POLITECNICO DI MILANO
DEPARTMENT OF PHYSICS
DOCTORAL PROGRAMME IN PHYSICS

---

# MULTIMODAL NONLINEAR OPTICAL MICROSCOPY FOR BIOLOGICAL APPLICATIONS

Doctoral Dissertation of:
**Benedetta Talone**

Supervisor:
**Prof. Dario Polli**

Tutor:
**Prof. Giulio Cerullo**

The Chair of the Doctoral Program:
**Prof. Marco Finazzi**

XXXIV Cycle

# Abstract in lingua italiana

Fin dalla sua invenzione, gli scienziati hanno utilizzato il microscopio per indagare le meraviglie della natura e della biologia, rivelando dettagli che altrimenti sarebbero invisibili ad occhio nudo. I microscopi sono diventati strumenti sempre piú sofisticati e complessi grazie ai progressi dell'ottica e della fotonica, e l'introduzione dell'illuminazione laser ha cambiato radicalmente il concetto di microscopia, spostandolo dalla semplice osservazione morfologica al riconoscimento delle strutture chimiche. Il potenziale eccezionale della microscopia ottica non lineare come tecnologia rapida, senza bisogno di marcatori, altamente specifica e ad alta risoluzione, cosí come i suoi benefici rispetto i metodi standard, sono stati ampiamente dimostrati. Inoltre, le varie modalitá non lineari di microscopia possono essere combinate in un singolo microscopio per sfruttare a pieno la capacitá delle informazioni che le immagini multimodali possono dare.

In questa tesi, dopo il capitolo introduttivo e il capitolo sui fondamenti teorici, vengono presentati tre lavori sperimentali che ho condotto durante il mio dottorato. Questi tre lavori esplorano diversi aspetti della microscopia ottica non lineare, prestando particolare attenzione alle applicazioni biologiche. A ciascuno di essi é dedicato un capitolo.

In primo luogo, ho concentrato la mia attivitá di ricerca sui meccanismi di fotodanneggiamento: dato l'uso crescente dei laser pulsati nelle applicazioni di biofotonica, é cruciale assicurarsi che il campione non venga danneggiato dal laser mentre viene osservato. Quindi, ho studiato la risposta delle cellule tumorali alla luce laser ultracorta nel vicino infrarosso. Ho misurato il tasso di sopravvivenza delle cellule HeLa in funzione della

potenza del laser, della velocitá di scansione e del tempo di esposizione, irradiandole con impulsi di 130-fs a 1040 nm di lunghezza d'onda e 80 MHz di frequenza di ripetizione in due configurazioni di illuminazione distinte. Per fornire informazioni rilevanti sulle circostanze di lavoro sicure a molti ricercatori che pianificano esperimenti che richiedono l'illuminazione laser, i risultati degli esperimenti sono stati esaminati utilizzando un metodo data-driven e quindi confermati con considerazioni termodinamiche.

Poi, ho sviluppato e ottimizzato un microscopio ottico multimodale non lineare in grado di acquisire immagini in cinque diverse modalitá: brightfield, fluorescenza a due fotoni, generazione di seconda armonica, coherent anti-Stokes Raman scattering e stimulated Raman scattering. Utilizzando questa tecnologia, ho condotto uno studio su campioni di sezioni di colonna vertebrale murina forniti da Humanitas-Clinical and Research Centre, per indagare il ruolo dell'enzima dipeptidil peptidase 3 (DPP3) nelle patologie ossee e nel mantenimento dell'omeostasi ossea. Facendo uso del nostro microscopio multimodale, dopo l'evidenziazione di discrepanze fra campioni sani e campioni con soppressione di DPP3, sono stati rivelati cambiamenti biologici rilevanti che non erano emersi facendo uso dei metodi standard. Grazie alle loro qualitá di non necessitare di marcatori, di essere chimicamente selettive e non invasive, le tecniche di microscopia ottica non lineare hanno dimostrato di essere valide e di successo nello studio delle malattie ossee, nonché uno strumento prezioso per la ricerca biologica.

Infine, ho approfondito il problema delle aberrazioni applicando l'ottica adattiva sensorless alla microscopia non lineare. Le variazioni dell'indice di rifrazione del campione sotto osservazione introducono aberrazioni ottiche che degradano la qualitá dell'immagine prodotta. É essenziale che il centro di massa della point spread function del sistema rimanga invariato durante la correzione, e perché ció avvenga, la base utilizzata per la correzione deve avere la proprietá di essere gradiente ortogonale. Mentre é stato dimostrato che la base dei polinomi di Lukosz possiede questa caratteristica per i processi lineari, non é stata dimostrata alcuna base conosciuta per i processi multiphotonici. Per risolvere questo problema, ho proposto un approccio sperimentale per la determinazione delle basi di aberrazione shift-less per le applicazioni di microscopia non lineare, convalidandolo facendo immagini in vivo di cervello di topo.

# Abstract

Since its conception, scientists have utilized the microscope to investigate the marvels of nature and biology, revealing details that would otherwise be invisible to the naked eye. Microscopes have become increasingly sophisticated and complex instruments as a result of advances in optics and photonics, and the introduction of laser illumination has fundamentally changed the concept of microscopy, shifting it from simple morphological observation to the recognition of chemical structures. The exceptional potential of nonlinear optical microscopy as a quick, label-free, highly specific, and high-resolution technology, as well as its benefits over standard methods, has been shown. In addition, various nonlinear microscopy modes may be combined in a single microscope to fully use the information capacity that multimodal pictures can give.

In this thesis, after the introductory chapter and the chapter on theoretical foundations, three experimental works that I conducted during my Ph.D. are presented. These three works explore different facets of the field of nonlinear optical microscopy, giving attention to biological applications. A chapter is dedicated to each of them.

First of all, I focused my research on photodamage mechanisms: given the rising usage of pulsed lasers in biophotonics applications, it is critical to ensure that the sample is not damaged by the laser while being observed. So, I studied the response of tumor cells to near-infrared ultrashort pulsed laser light. I measured the survival rate of HeLa cells as a function of laser power, scanning speed, and exposure period, irradiating them with 130-fs pulses at 1040 nm wavelength and 80 MHz repetition rate in two distinct

illumination settings. To give relevant insights into safe working circumstances to many researchers planning experiments requiring laser illumination, the outcomes of the experiments were examined using a data-driven method and then confirmed with thermodynamic considerations.

Then, I developed and optimized a multimodal nonlinear optical microscope able to acquire images in five different modalities: bright-field, two-photon excitation fluorescence, second harmonic generation, coherent anti-Stokes Raman scattering and stimulated Raman scattering. Using this technology, I conducted a study on murine spine section samples provided by Humanitas-Clinical and Research Centre, to investigate the role of the enzyme dipeptidyl peptidase 3 (DPP3) in bone pathology as well as the maintenance of bone homeostasis. Relevant biological changes were revealed using our multimodal microscope after highlighting discrepancies between healthy wild-type samples and DPP3 knock-out samples that had not been disclosed using standard approaches. Because of their label-free, chemically selective, and non-invasive qualities, nonlinear optical microscopy techniques have proven to be legitimate and successful in the investigation of bone diseases, as well as a valuable tool for biological research.

Finally, I delved into the problem of aberrations applying sensorless adaptive optics to nonlinear microscopy. Variations in the refractive index of the sample under observation introduce optical aberrations, which degrade the quality of the image produced. It is essential that the center of mass of the system point diffusion function remains unchanged during correction, and for this to happen, the base used for correction must have the orthogonal gradient property. While it has been shown that the Lukosz Polynomials base possesses this characteristic for linear processes, no known basis has been shown to be so for multiphotonic processes. To solve this issue, I proposed an experimental approach for determining shiftless aberration bases for nonlinear microscopy applications, validating it by making in vivo images of mouse brain.

# Contents

# CHAPTER 1

# Introduction

For more than a century, scientists have used the microscope to investigate the marvels of nature and biology, revealing subtleties that would otherwise have been invisible to the naked eye. The advancement of optics and photonics has allowed microscopes to become increasingly sophisticated and complex instruments. The introduction of laser illumination has transformed the concept of microscopy, shifting it from simple morphological observation to the recognition of chemical structures, and this has had a profound impact on the field of microscopy. Nonlinear optical microscopy has shown its amazing potential as a quick, label-free, highly specific, and high-resolution technology, as well as its benefits over traditional linear techniques. Moreover, several nonlinear microscopy modalities may be combined in a single experimental setup, to fully leverage the information capacity that multimodal images give. This results in the enhancement of a single image through the use of numerous complimentary contrast processes, which allow the simultaneous capture of morphological and chemical-functional information from a single observation.

Among traditional microscopy techniques, fluorescence imaging techniques [95] are by far the most popular in the biological sciences. To reveal morphological information about a tissue through accumulation in specific biological sites, these methods, particularly in their linear form, are now well-established and typically use exogenous staining and labeling with fluorophores, to be excited with visible light. Fluorescence is the most widely used tool for biological-medical research because of its selective character and the large number of fluorescent probes that have been created in recent decades [25, 39, 170, 192]. Even though fluorescence plays a critical role in biomedical research, the requirement to employ exogenous fluorescent molecules restricts the innovation potential of this technology. Sample preparation for microscopy sometimes requires lengthy processes and the addition of fluorophores is incompatible with *in vivo* imaging in the vast majority of situations. Indeed, there are numerous fluorescent probes that pose a significant barrier to their use in the clinical setting because of their toxicity.

Another very popular linear technique for biological imaging and material characterisation is based on spontaneous Raman scattering. The foundation of this technique was presented in 1928 by Raman and Krishnan [146] who reported the discovery of spontaneous inelastic scattering of light by molecules. The vibrational energy levels of the diffusing molecule are represented by the energy loss between the incident photons and the inelastically diffused photons. As a result, the analysis of spectral line displacement caused by the Raman effect offers information on the chemical composition, molecular structure, and intermolecular interactions of the material under investigation. This technique exceeds many limits presented by fluorescence, being label-free, chemically selective and not requiring any sample preparation. Unfortunately the spontaneous Raman scattering is very weak and the integration time necessary for signal detection make it not suitable for imaging applications on wide fields of view, such as those required in diagnostic and biomedical field. These critical issues have been the drive to orient recent research towards label-free, noninvasive, nonlinear optical (NLO) imaging methods.

Fluorescence microscopy's multiphoton declination is two-photon excitation fluorescence microscopy (TPEF). We owe the elaboration of the principle of two-photon absorption to Maria Goeppert-Mayer [61]. It was in her PhD thesis that she first described this third-order NLO phenomenon and it represented the theoretical foundation for all multiphoton optical microscopy techniques. For the experimental confirmation of it, we had to wait 30 years, until the advent of laser sources when Kaiser and Garrett, in 1961, employed a pulsed ruby laser to excite two-photon absorption in a $CaF_2$:$Eu^{3+}$ crystal, generating the fluorescent emission of high-energy photons in the blue spectral region [80]. In fact, for multiphoton absorption to occur, it is required to have a high spatial and temporal confinement of a large number of low-energy photons in a small area and this situation is readily created by using ultrashort-pulsed laser sources [151].

Actually, conventionally (and rather unfairly), the observation of second-harmonic generation (SHG) signal by Franken and colleagues in 1961 [49], just before Kaiser and Garrettâs demonstration of the TPEF, is considered the beginning of the field of nonlinear optics, although signs of this field may be found dating back considerably farther. In their seminal work, they observed that if a ruby laser pulse at frequency $\omega_1$ propagates through a quartz crystal, then radiation at the second harmonic frequency $\omega_2 = 2\omega_1$ is coherently generated in the material.

Vibrational imaging techniques based on Raman effect have evolved in various directions, but the most interesting ones for biomedical imaging applications are definitely the coherent Raman scattering (CRS) techniques. In CRS techniques, the interaction between two input light fields, at different frequencies, and matter induces Raman-active mode of vibration, that is used as imaging contrast mechanism for microscopy applications [30]. These techniques' initial experimental demonstration, like those of other NLO methods such as TPEF and SHG, came about as a result of the development of laser technology beginning in 1960 [107], which provided access to very powerful coherent light sources. CRS was discovered by chance in 1962, when researchers from the Woodbury group discovered an unanticipated additional line in the output spectrum of their Ruby laser [45, 187]. This result was ascribed to Raman scattering occurring inside the Ruby laser cavity, which was caused by the presence of liquid nitrobenzene utilized as a Kerr shutter. Indeed, the energy difference between the fundamental and red-shifted lines was found to correspond to the energy associated with the strongest $NO_2$ symmetric stretching vibration in nitrobenzene. Due to the fact that the phenomenon was thought to be caused by stimulated emission processes inside the laser cavity, it was dubbed stimulated Raman scattering (SRS). Also coherent anti-Stokes Raman scattering (CARS) signal was observed for the first time accidentally. As a part of their third-order response studies on materials with a Ruby laser in 1963, Ford Scientific Laboratory researchers Maker and Terhune noticed an unexpected signal from a higher-frequency blue-shifted radiation than the laser's basic one, but the first contribution in literature was published by Yajima and Takatsuji in 1964 [189]. Indeed, Maker and Terhune published their results only in 1965, after conducting further studies [108].

Even after their discovery, NLO microscopy remained mostly inactive in biology and medicine for about 30 years. Once again, breakthroughs in the discipline were spurred on by significant advancements in laser sources and technology. To study living cells and tissues using two-photon laser scanning fluorescence microscopy in 1990, Denk, Webb, and colleagues used a sub-picosecond pulsed dye laser [40]. Their work revealed the potential of the two-photon excitation microscopy while also paving the way for the use of additional nonlinear optical techniques for biomedical imaging research. Indeed, during the 1990s and 2000s, second harmonic generation [65] and later coherent anti-Stokes Raman scattering [32] were proved to be very effective biological imaging methods, each offering unique, and often complimentary, chemical information. However, because to the more complex detection scheme, the application of SRS to biological imaging occurred a few years later [50].

TPEF, SHG and CRS are examples of label-free microscopy techniques, derived from advances in technology, which base their contrast mechanism on the inherent features of the specimen under observation. Despite the fact that no optical modality is capable of acquiring all the information offered by histological and immunohistochemical investigations, the ability to gather morphological and biochemical information using quick, non-destructive, and label-free procedures is of paramount relevance. Multimodal microscopy holds promise to combine different NLO techniques to gather morphological and chemical-functional information. This may exceed the limits of conventional microscopy, such as the use of dyes and low chemical specificity, and improve observation with numerous complementary contrast processes [28, 109, 114, 131]. In recent years, since multiple NLO modes have been integrated on the same experimental configuration, many pioneering studies have been conducted. Just to give some examples, an extraordinary result was achieved by Wang and colleagues who finally managed to acquire *in vivo* images of white matter at single-cell resolution [182], and Huff *et al.* directly visualized the interactions between myelinated axons and other essential components (e.g. astrocyte processes, calcium activity) in it [73]. Le *et al.* [96] and Nan *et al.* [122] investigated lipid droplets monitoring their dynamic roles in various aspects of lipid metabolism. As a result of growing public interest in this technology, optical systems are becoming more and more complex and powerful [136]. Pegoraro and coworkers [133] demonstrated the applicability of a high-performance multimodal microscopy setup on live cells and tissues with user-variable spectral resolution and broad Raman tunability.

Nonlinear microscopy has shown its advantages over linear techniques in a wide range of biological and medical research, as well as its uncanny ability to be a fast, label-free, high-specificity, and high-resolution method.

In fact, these peculiar characteristics are revealing their usefulness in the diagnostic and therapeutic field of different diseases [73].

During my PhD, I had the opportunity to explore many facets of nonlinear microscopy, whose theoretical foundations are briefly presented in Chapter 2. Initially my research activity focused on the study of phototoxicity induced on viable Hela cells from infrared ultrashort pulsed laser radiation. The purpose was to characterize the cell response to laser irradiation to find microscopy working conditions that did not damage the sample. Phototoxicity is a very important topic in microscopy, which becomes crucial when dealing with biological samples. It is an extremely complex subject, which depends on many variables and around which there are many open questions on which you must continue to question and do research. This study and its results are presented in Chapter 3 and have also been published on Biomedical Optics Express journal with the title "Phototoxicity induced in living HeLa cells by focused femtosecond laser pulses: a data-driven approach" [167].

Most of my efforts focused on the optimization of the multimodal nonlinear optical microscope, that we developed in the VIBRA - Nonlinear Optical Microscopy Lab (www.vibra.polimi.it), for biological applications. Thanks to a productive collaboration with Humanitas - Clinical and Research Centre, we had the possibility to test our technology imaging murine spine section samples. The projectâs goal was to investigate the involvement of the enzyme dipeptidyl peptidase 3 (DPP3) in bone pathology and the maintenance of bone homeostasis as well as to demonstrate the validity of nonlinear microscopy techniques as an effective tools in the study of bone diseases. The full study is presented in Chapter 4.

Finally, in Chapter 5, the result of the collaboration with Neurophotonics group of Universitá degli Studi di Modena e Reggio Emilia is presented. During this collaboration I was able to discover the enormous potential of adaptive optics and its application to nonlinear imaging techniques. In addition, I had the opportunity to expand my expertise on biological samples, even conducting *in-vivo* experiments. In particular, we proposed a calibration method for correction base to avoid the displacement of the field of view during the optimization procedure in sensorless adaptive optics microscopy applications. Also in this case, the work was published on Optics Express journal with the title "Experimental determination of shift-less aberration bases for sensorless adaptive optics in nonlinear microscopy" [168].

# CHAPTER 2

# Theoretical Foundations

In this chapter an overview on the theoretical bases of nonlinear optical microscopy is provided, starting from the principles of nonlinear optics and giving a short mathematical framework for each microscopy techniques used in this thesis, with a strong focus on the physical interpretation of the processes involved.

## 2.1 Elements of Nonlinear Optics: classical description

Nonlinear optics is the discipline of physics that analyzes all the processes that occur in a material system when light causes its optical characteristics to change. Since it is necessary to expose a material to an intense light in order to induce an alteration of its optical characteristics, the laser sources are the preferred lighting sources used in this field, for their characteristics of coherence and intensity. The introduction of the concept of nonlinearity is due to the fact that the illuminated material system responds in a nonlinear way with respect to the strength of the applied optical field. To clarify this notion of optical nonlinearity, we will begin our theoretical framework talking about the polarization $P(t)$ of a material system.

### 2.1.1 The Nonlinear Optical Susceptibility

At the heart of both linear and nonlinear optical processes is the light-matter interaction between an electromagnetic field and the charged particles in the material system through which the field is propagating. This interaction determines a displacement of the electrical charges from their equilibrium position, alterating their spatial and temporal distribution [31]. As a result of this displacement of the valence electrons, an electric dipole moment $\mu$ is induced in a molecule of the material system [57], defined as:

$$\mu(t) = -e \times r(t), \tag{2.1}$$

with $e$ the electron charge and $r(t)$ the displacement from its equilibrium position.

Taking the sum of all the $N$ electric dipoles in a volume of material, with $N$ the average number of dipoles per unit volume, leads to the definition of the macroscopic polarization:

$$P(t) = N < \mu(t) >, \tag{2.2}$$

in which $< \mu(t) >$ represents the spatial average of the dipole moments. Polarization is an essential tool when it comes to interaction radiation-matter, being responsible for all interaction, whether linear or nonlinear effects. Assuming that the incident field is weak enough to not exceed the binding field between the electron and its nucleus, the macroscopic polarization and the applied electric field are linearly dependent as shown in this equation:

$$P(\omega) = \epsilon_0 \chi^{(1)} E(\omega), \tag{2.3}$$

where $\epsilon_0$ is the vacuum permittivity and $\chi^{(1)}$ is the linear susceptibility of the material. In this approximation the induced displacement of the electron charge is small and the harmonic approximation is still valid [31]. With growing field strength and larger electrons oscillations, the anharmonic contributions to the binding nuclear potential become more relevant [16]. The first-order approximation of the polarization is no more sufficient and more complex interactions must be considered. The simplest way to correct the harmonic potential, assuming that the anharmonic contributions are still relatively small, consists in expanding the electrons displacement in a power series around the equilibrium position. In the description of the polarization, this translates to the inclusion of higher-ordered terms, which represents the effects of nonlinear electron motions [5]:

$$P(\omega) = \epsilon_0 [\chi^{(1)} E(\omega) + \chi^{(2)} E(\omega)^2 + \chi^{(3)} E(\omega)^3 + \dots] \tag{2.4}$$

with $\chi^{(2)}$ and $\chi^{(3)}$ the second-order and third-order nonlinear susceptibilities respectively.

The most common way to describe nonlinear optical phenomena is to write the polarization in frequency domain, like we did. This is because a time-varying polarization can lead to introducing new components of the electromagnetic field.

### 2.1.2 The Wave Equation for Nonlinear Optical Media

To be clear and exhaustive, we decided to start from Maxwell′s equations:

$$\nabla \cdot \mathbf{D} = \rho; \tag{2.5}$$

$$\nabla \cdot \mathbf{B} = 0; \tag{2.6}$$

$$\nabla \times \mathbf{E} = -\frac{\partial \mathbf{B}}{\partial t}; \tag{2.7}$$

$$\nabla \times \mathbf{H} = \frac{\partial \mathbf{D}}{\partial t} + \mathbf{J}. \tag{2.8}$$

Considering the objective of this thesis, we may assume that:

- there are no free charges in the region of interest:

$$\rho = 0, \tag{2.9}$$

- there are no free currents in the region of interest:

$$\mathbf{J} = 0, \tag{2.10}$$

- we are dealing with a nonmagnetic material system:

$$\mathbf{B} = \mu_0 \mathbf{H}, \tag{2.11}$$

To correctly account for the nonlinearity of the material system, we must express the field D as:

$$\mathbf{D} = \epsilon_0 \mathbf{E} + \mathbf{P}, \tag{2.12}$$

where the polarization vector **P** is nonlinearly dependent on field **E**. Without going into the calculations, exploiting these premises it is possible to derive the wave equation in nonlinear optics in its most general form:

$$\nabla \times \nabla \times \mathbf{E} + \frac{1}{c^2}\frac{\partial^2 \mathbf{E}}{\partial t^2} = -\frac{1}{\epsilon_0 c^2}\frac{\partial^2 \mathbf{P}}{\partial t^2} \tag{2.13}$$

Under certain conditions, including the validity of the slowly varying amplitude approximation, Eq. (2.13) can be simplified and rewritten in the form:

$$\nabla^2 \mathbf{E} - \frac{1}{\epsilon_0 c^2} \frac{\partial^2 \mathbf{D}}{\partial t^2} = 0 \tag{2.14}$$

To continue in this dissertation, it is convenient to rewrite the polarization vector $P$ as:

$$\mathbf{P} = \mathbf{P}^{(1)} + \mathbf{P}^{(NL)}, \tag{2.15}$$

dividing its component ($\mathbf{P}^{(1)}$) linearly dependent on the applied electric field $E$ from that ($\mathbf{P}^{(NL)}$) not linearly dependent. Similarly, the displacement field $\mathbf{D}$ can be split into its linear and nonlinear components:

$$\mathbf{D} = \mathbf{D}^{(1)} + \mathbf{P}^{(NL)}, \tag{2.16}$$

with the linear part $\mathbf{D}^{(1)}$ defined as:

$$\mathbf{D}^{(1)} = \epsilon_0 \mathbf{E} + \mathbf{P}^{(1)}. \tag{2.17}$$

Now we can rewrite Eq. (2.14) by making the linear and nonlinear parts of the field $\mathbf{D}$ explicit:

$$\nabla^2 \mathbf{E} - \frac{1}{\epsilon_0 c^2} \frac{\partial^2 \mathbf{D}^{(1)}}{\partial t^2} = \frac{1}{\epsilon_0 c^2} \frac{\partial^2 \mathbf{P}^{(NL)}}{\partial t^2}. \tag{2.18}$$

Now let′s consider the simplified case of a lossless, dispersionless and isotropic medium. In this particular condition we can write the linear part of the displacement field $\mathbf{D}^{(1)}$ as:

$$\mathbf{D}^{(1)} = \epsilon_0 \epsilon^{(1)} \mathbf{E}, \tag{2.19}$$

where the constant between $\mathbf{D}^{(1)}$ and $E$ is given by the product of two scalar constants: the vacuum permittivity $\epsilon_0$ and the relative permittivity of the material $\epsilon^{(1)}$. So, for this simplified case, the wave equation (2.18) becomes:

$$-\nabla^2 \mathbf{E} + \frac{\epsilon^{(1)}}{c^2} \frac{\partial^2 \mathbf{E}}{\partial t^2} = -\frac{1}{\epsilon_0 c^2} \frac{\partial^2 \mathbf{P}^{(NL)}}{\partial t^2}. \tag{2.20}$$

Written in this form, it′s easy to see that the nonlinear polarization (i.e. the nonlinear response of the material) acts as a source term in this equation that has the form of a driven wave equation.

## 2.2 Nonlinear Optical Microscopy

As already said, the discovery of second harmonic generation by Franken and colleagues in 1961 [49] is regarded as the beginning of the field of nonlinear optics. Generally speaking, the development of nonlinear optics has been stimulated by the need to improve the performance of traditional microscopes. Traditional linear microscopy is intrinsically limited in the spatial resolution by the well-known Abbe diffraction limit, which states that the minimum resolvable distance for a microscope is equal to about half the wavelength of the light employed. The spectrum of light that can be used to observe biological samples is well defined by their optical properties, so it is not possible to simply decrease the wavelength of the excitation light to improve resolution [111]. Progress in life sciences, medicine, and biology has opened up new challenges and questions, making it necessary to explore the infinitely small sub-cellular and molecular world, not accessible with traditional technologies. Nonlinear optical microscopy techniques respond effectively to this need, paving the way for the clinical translation of biophotonic technologies, thanks to their label-free nature, intrinsic 3D sectioning capabilities, and high penetration depth.

### 2.2.1 Multiphoton Microscopy

In light-matter interaction, an incident photon may be absorbed by a molecule, for example a fluorophore, and that because of this absorption the molecule undergoes an electronic transition from the fundamental state to an excited state. Such phenomena are defined as linear or one-photon absorption phenomena (OPF). However, the same transition can also be achieved through the simultaneous absorption of two or more photons, using longer wavelength excitation photons and high illumination intensities [117]. These processes, involving more than one photon, are nonlinear, and are grouped under the name of multiphoton excitation fluorescence (MPEF). According to the theory of multiphoton excitation, the multiphoton excitation fluorescence signal generated is proportional to the n-power of the incident light beam intensity, where n denotes the number of photons simultaneously absorbed, thus the order of nonlinearity.

#### Two-photon excitation fluorescence

By far the most well-known and used multiphoton interaction in imaging and microscopy is two-photon excitation fluorescence (TPEF). This phenomenon may be conceptualized as the absorption of two excitation pho-

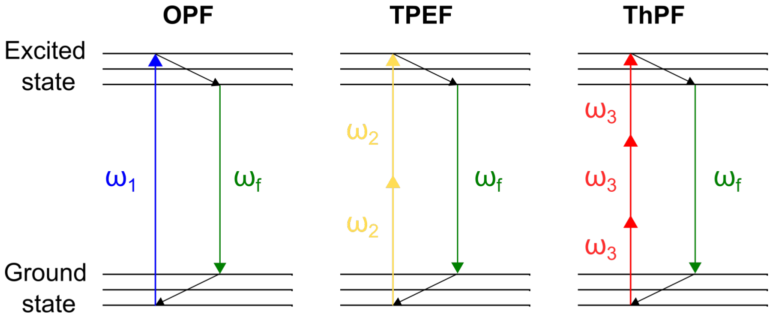

**Figure 2.1:** *Jablonski diagram of the linear one-photon excitation fluorescence transition compared to those of the nonlinear two- and three-photon excitation fluorescence (TPEF and ThPF). Dashed lines represent virtual states while solid ones represent real states.*

tons with frequency $\omega_1$ and the subsequent emission of a single fluorescence photon with frequency $\omega_f$, as seen in Fig. 2.1. Owing to energy conservation, the frequency of the emitted fluorescence photons should be double that of the excitation photons; nevertheless, energy is lost into the molecular environment through non-radiative decay processes. As a result, the frequency of the emitted photon $\omega_f$ is lower than the sum of the frequencies of the absorbed photons $2\omega_1$, and the lost energy is dissipated in the form of heat [16]. Due to the nonlinear nature of TPEF, a signal proportional to the squared power of the excitation beam intensity is generated:

$$I_{TPEF} = \sigma_{2f} I^2 \tag{2.21}$$

in which $\sigma_{2f}$ represents the two-photon absorption cross-section and $I$ is the excitation light intensity. Thus, as very high intensities are needed, when a sample is excited with a pulsed and focused laser beam, TPEF is generated only from a tiny volume centered on the focal point, with the highest power density [41]. This provides the TPEF its 3-dimensional sectioning capability. This characteristic is very advantageous in optical microscopy, as it allows one to eliminate the out-of-focus fluorescence signal, as depicted in Fig. 2.2. In addition, the use of longer wavelengths for excitation provides greater penetration depths, as photons are less scattered during propagation through the medium [117]. Hence, this nonlinear microscopy technique allows one to acquire almost background-free images with high spatial resolution. Furthermore, the use of NIR laser sources ensures that the sample under observation experiences less photodamage than would cause a VIS laser source, typically employed in linear microscopy. And also, the detrimental phototoxic effects to the sample are spatially limited and mitigated, being the absorption confined to the focal spot.

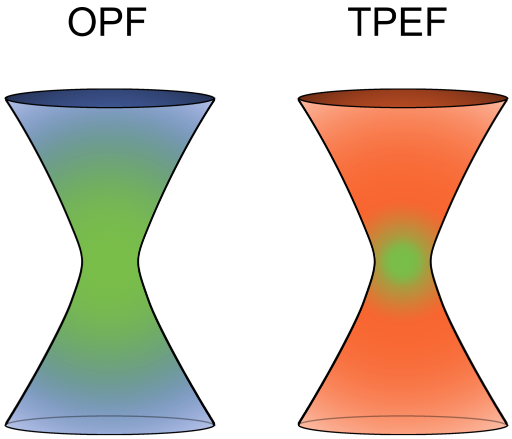

**Figure 2.2:** *Difference between OPF (incoherent processes) and TPEF (coherent processes). In the latter, the excitation is localized only in the focal spot, as highlighted by the green shade.*

Moving to a more rigorous mathematical discussion of the process, we will derive the transition rate and the cross section for two-photon absorption (2PA), exploiting the time-dependent perturbation theory, within the semiclassical framework [16]. We can use this formalism as we are interested in studying 2PA process in biological samples for microscopy applications. The perturbative regime occurs when an incident excitation light, with intensity of the order of GW/cm$^2$ ($10^9$ W/cm$^2$), produces a distortion of the electronic cloud in the material [16, 99].

The first step to derive the 2PA rate consists in assuming that the atomic wavefunction $\psi(\mathbf{r}, t)$ follows the time-dependent Schrödinger equation

$$i\hbar \frac{d\psi(\mathbf{r}, t)}{dt} = H\psi(\mathbf{r}, t). \tag{2.22}$$

The Hamiltonian H can be represented as the sum of the Hamiltonian of the unperturbed system H$_0$ and the time-dependent interaction potential with the applied field V(t), that is:

$$H = H_0 + V(t), \tag{2.23}$$

where V(t) can be expressed as:

$$V(t) = -\mu \mathbf{E}(t), \tag{2.24}$$

where, for sake of simplicity, we will consider the applied optical field **E** to be a monochromatic wave of the form:

$$\mathbf{E}(t) = Ee^{-i\omega t} + c.c. \tag{2.25}$$

It is possible to express the solution to Schrödinger equation as the linear combination of the eigenstates associated with them

$$\psi(\mathbf{r}, t) = \sum_l a_l(t) u_l(\mathbf{r}) e^{-i\omega_l)t}, \tag{2.26}$$

with $a_l(t)$ the probability amplitude that atom is in energy eigenstate $l$ at time t. By placing Eq. (2.23) and Eq. (2.26) in Eq. (2.22), taking advantage of perturbation techniques and performing calculations, one can find an approximated solution to the problem, written in the form of a set of equations:

$$\frac{da_m^{(N)}}{dt} = (i\hbar)^{-1} \sum_l a_l^{(N-1)} V_{ml} e^{-i\omega_{lm} t}, \qquad N = 1, 2, 3 \ldots \tag{2.27}$$

In the last equation, $\omega_{ml} = \omega_m - \omega_l$ is the transition frequency between the eigenstates $l$ and $m$ and V$_{ml}$ is the matrix element of the perturbing Hamiltonian V.

Setting N=1 amounts to describe linear absorption in the case of first-order interactions in the field, and Eq. (2.27) becomes:

$$\frac{da_m^{(1)}}{dt} = -(i\hbar)^{-1} \mu_{mg} [Ee^{-i(\omega_{mg} - \omega)t} + E^* e^{i(\omega_{mg} + \omega)t}], \tag{2.28}$$

where $\omega_{mg} = \omega m - \omega g$ represents the transition frequency between the state $g$ (typically the ground state) and the excited state $m$, as depicted in Fig. 2.3.

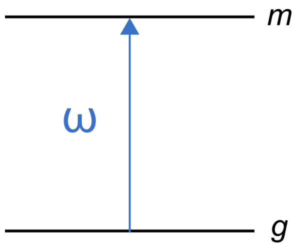

**Figure 2.3:** *Energy levels involved in the one-photon absorption process.*

In the assumption that, before the application of the field, the atom stays in its ground state, the following expression for the probability amplitude is found:

$$\begin{aligned} a_m^{(1)}(t) &= -(i\hbar)^{-1}\mu_{mg}\int_0^t dt[Ee^{-i(\omega_{mg}-\omega)t} + E^* e^{i(\omega_{mg}+\omega)t}] \\ &= \frac{\mu_{mg}E}{\hbar(\omega_{mg}-\omega)}[e^{i(\omega_{mg}-\omega)t} - 1] + \frac{\mu_{mg}E^*}{\hbar(\omega_{mg}+\omega)}[e^{i(\omega_{mg}+\omega)t} - 1]. \end{aligned} \tag{2.29}$$

The first term of Eq. (2.29) represents the process of one-photon absorption, while the second term represents the process of stimulated emission. In the rotating wave approximation, the stimulated emission term can be neglected and Eq. (2.29) reduces to:

$$a_m^{(1)}(t) = \frac{\mu_{mg}E}{\hbar(\omega_{mg}-\omega)}[e^{i(\omega_{mg}-\omega)t} - 1] \tag{2.30}$$

It is now possible to move the discussion to the case of two-photon absorption. By solving Eq. (2.27) for N=2, we obtained:

$$\begin{aligned} \frac{da_m^{(2)}}{dt} &= (i\hbar)^{-1}\sum_m a_m^{(1)} V_{nm} e^{-i\omega_{mn}t} \\ &= -(i\hbar)^{-1}\sum_m \frac{\mu_{nm}\mu_{mg}E^2}{\hbar(\omega_{mg}-\omega)}[e^{-i(\omega_{ng}-2\omega)t} - e^{i(\omega_{nm}-\omega)t}]. \end{aligned} \tag{2.31}$$

A graphical definition of energy levels used in Eq. (2.31) is given in Fig. 2.4.

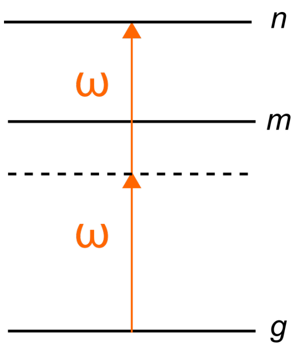

**Figure 2.4:** *Representation of energy levels used in the derivation of the transition rate for two-photon absorption process.*

Considering Eq. (2.31), the second term in square brackets can be discarded because it is not significant for the process of two-photon absorption, and the resultant equation can be integrated to obtain:

$$a_m^{(2)}(t) = \sum_m \frac{\mu_{nm}\mu_{mg}E^2}{\hbar^2(\omega_{mg} - \omega)} \left[ \frac{e^{i(\omega_{mg}-2\omega)t} - 1}{\omega_{mg} - 2\omega} \right]. \tag{2.32}$$

By squaring the module of this probability amplitude $a_m^{(2)}(t)$, the probability of two-photon absorption $p_m^{(2)}(t)$ is obtained, that is

$$p_m^{(2)}(t) = |a_m^{(2)}(t)|^2 = \left| \sum_m \frac{\mu_{nm}\mu_{mg}E^2}{\hbar^2(\omega_{mg} - \omega)} \right|^2 2\pi t \rho(\omega_{ng} = 2\omega), \tag{2.33}$$

where it is assumed that, for large t, in a realistic situation the transition driven by $\omega_{ng}$ does not lead exactly to a single state but to a density of final states $\rho_f(\omega_{mg})$. Finally, deriving the two-photon absorption probability with respect to t, the transition rate for two-photon absorption is obtained as

$$R_{ng}^{(2)} = \sigma_{ng}^{(2)}(\omega) I^2. \tag{2.34}$$

In the last equation, $I = 2n\epsilon_0 c|E|^2$ is the intensity of the excitation beam and $\sigma_{ng}^{(2)}(\omega)$ represents the two-photon cross section, which is usually expressed in units of Göppert-Mayer (GM), and can be written as:

$$\sigma_{ng}^2(\omega) = \frac{1}{4n^2\epsilon_0^2 c^2} \left| \sum_m \frac{\mu_{nm}\mu_{mg}}{\hbar^2(\omega_{mg} - \omega)} \right|^2 2\pi \rho_f(\omega_{ng} = 2\omega) \tag{2.35}$$

#### Second harmonic generation

As already mentioned, the first documented observation of the second-harmonic generated signal was made by Franken and coworkers in 1961 [49]. The incidence of a laser beam with frequency $\omega$ onto a nonlinear optical medium could result in the generation of a second laser beam with frequency $2\omega$. The polarization vector $P(\omega)$ (see Eq. (2.4)) represents the response of the medium, and it is dependent on its susceptibility $\chi$. The first-order susceptibility is used to describe linear interaction processes. To describe more complex nonlinear processes one must consider the terms of higher orders. The terms of second and third order, $\chi^{(2)}$ and $\chi^{(3)}$, are responsible for the second-harmonic generation and the third-harmonic generation, respectively. The occurrence of interactions of a higher order, even very rare and exotic, is in any case possible [26]. Jablonski diagrams of these two processes (second- and third-harmonic generation) are given in Fig. 2.5. The presence or absence of spatial symmetry in the material is a decisive factor in the creation of nonlinear effects. According to the electric dipole approximation, if a material shows centrosymmetry (that is, if it has a center of inversion), then all of the susceptibility components of even order must disappear as well. As a result, centrosymmetric materials are fully excluded from second-order processes, which is the first and most evident conclusion of this. The second implication that follows from this is that, in order to generate a discernible signal, the material must be non-centrosymmetric throughout the macroscopic dimensions. This property is not necessarily a downside of the technique, quite the contrary: some biological samples that exhibit a well-defined orientation, such as collagen fibrils, emit a signal that is not only related to the intensity of the applied field or the number of molecules but also their spatial distribution [120]; the information obtained is more intricate but richer than in other comparable techniques, such as TPEF, and it will be of paramount importance for the discussion of Chapter 4.

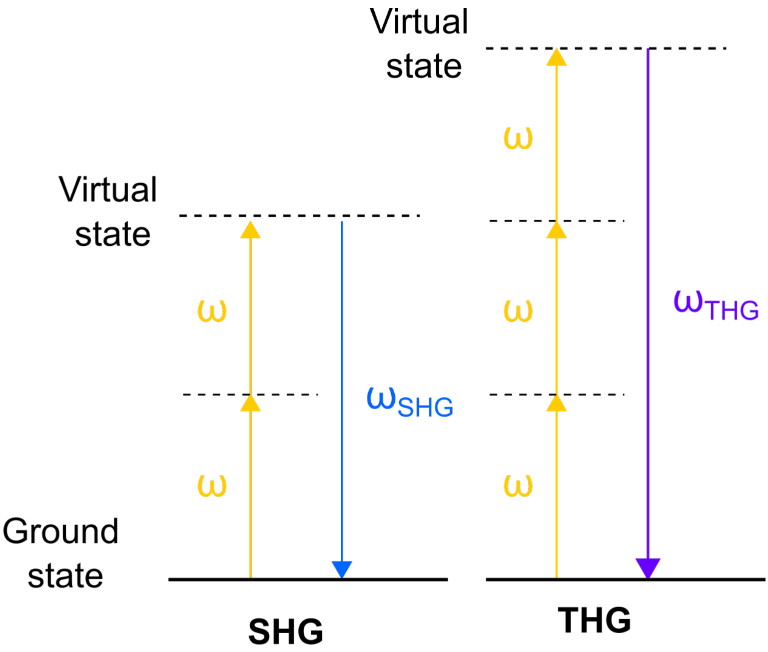

**Figure 2.5:** *Quantum mechanics of the different transitions happening in SHG and THG processes, as depicted in a Jablonski diagram.*

TPEF and SHG share some similarities: typically, the same pump laser used for TPEF is also often suitable for SHG, but differently from TPEF, second harmonic generation is a coherent process, thus light is scattered by the material and its phase retains a tight correlation with that of the incident beam. In fact, there is no energy deposition during this process and the system is left unchanged. This is the characteristic of a parametric interaction, which sets it apart from absorption processes like TPEF. The response of the system is almost instantaneous, on the order of femtoseconds, as the virtual states are short-lived, whereas fluorescence processes lifetime is on the order of nanoseconds. SHG retains most of the advantages of multiphoton microscopies, such as its intrinsic 3D resolution and optical sectioning. The intensity of the second harmonic radiation generated $I_{SHG}$ can be calculated rigorously following some mathematical steps. Our derivation closely resembles that offered in the book "Handbook of Biomedical Nonlinear Optical Microscopy" [111]. Let′s start from the wave equation (2.20) for an electric field propagating in a nonlinear medium. This time, we assume that the fundamental- and second-harmonic waves can be represented as plane waves, and written in the form:

$$\mathbf{E}_j(z,t) = E_j(z)e^{-i\omega_j t} + c.c. = A_j(z)e^{i(k_j z-\omega_j t)} + c.c., \qquad j = 1,2 \tag{2.36}$$

where $\omega_1 = \omega$ and $\omega_2 = 2\omega$, $A_j(z)$ is the spatially slowly varying field amplitude of field $j$. Similarly, nonlinear polarization for the second-harmonic wave is given by:

$$\mathbf{P}_2(z,t) = P_2(z)e^{i(2k_1 z-2\omega_j t)} + c.c., \tag{2.37}$$

with the complex amplitude of the nonlinear polarization $P_2$, defined as:

$$P_2 = P(\omega_2) = \epsilon_0\chi^{(2)}E_1^2 \tag{2.38}$$

Using Eq. (2.36) and Eq. (2.37) in Eq. (2.20), we obtained:

$$\frac{d^2A_2}{dz^2} + 2ik_2\frac{dA_2}{dz} - k_2^2A_2 - \frac{(2\omega)^2n_2^2}{c^2}A_2 = -(2\omega)^2\epsilon_0\mu_0\chi^{(2)}A_1^2e^{i(2k_1-k_2)z} \tag{2.39}$$

Simplifying this expression and applying the slowly varying amplitude approximation, we arrived at the equation:

$$\frac{dA_2}{dz} = \frac{2i\omega}{n_2c}\chi^{(2)}A_1^2e^{i(2k_1-k_2)z} \tag{2.40}$$

Assuming a low conversion efficiency, i.e. $E(\omega)$ almost constant over the material medium, $A_1$ can be considered as a constant. Integrating Eq.

(2.40), we obtained:

$$A_2(L) = \frac{2i\omega\chi^{(2)}A_1^2}{n_2 c}\frac{e^{i\Delta k}-1}{i\Delta kL}, \tag{2.41}$$

that is the amplitude of the second-harmonic field for a distance propagation $L$ and $\Delta k = 2k_1 - k_2$ is the wave vector mismatch of the forward-propagating field.

At this point, we can easily calculate the intensity of the second-harmonic radiation generated $I_{SHG}$ (that is equal to $I_2$), since $I = 2n\sqrt{\epsilon_0/\mu_0}|A|^2$, so:

$$I_{SHG}(L) = \sqrt{\frac{\mu_0}{\epsilon_0}}\frac{2\omega^2}{n_\omega^2 n_{2\omega}c^2}[\chi^{(2)}]^2 I_1^2 L^2[sinc^2(\Delta kL/2)]. \tag{2.42}$$

The phase-matching condition radically affects the radiation pattern and the intensity of the generated signal and the maximum conversion efficiency is achieved when the phase-matching condition is fulfilled, that is $\Delta k = 0$. This poses some constraints in the applicability of SHG: in biological imaging for example, a field in which SHG has been widely used and promoted [52], the phase-matching condition is most easily satisfied if the detection unit is placed in the forward direction and for thin samples only.

### 2.2.2 Vibrational microscopy: coherent Raman scattering

Coherent Raman scattering (CRS) microscopy methods are incredibly renowned noninvasive nonlinear techniques for obtaining chemical specificity by using the Raman-active vibrational modes of materials under observation.

A $'$pump$'$ laser beam, at frequency $\omega_p$, and a $'$Stokes$'$ laser beam, at frequency $\omega_S$, are spatially and temporally sinchronized and focused on a specimen. If the frequency difference between the two laser beam matches a Raman vibrational mode $\Omega$ of the specimen, namely $\Omega = \omega_p - \omega_S$, the combination of the two fields, pump and Stokes, acts as a driving field, making the molecules in the focal volume oscillate coherently. Unlike the weak incoherent signals generated in the spontaneous Raman process, the coherent nature of the CRS signal makes CRS microscopy techniques suitable for fast imaging applications.

CRS techniques are third-order nonlinear processes governed by third-order susceptibility $\chi^{(3)}$. Generation of a CRS signal, can be imagined as a two-step process: firstly, a state of vibrational coherence is induced in the targeted molecules by the two laser pulses, pump and Stokes, with optical frenquency difference equal to $\Omega$ (Raman vibrational mode of the molecule). In the second stage, the CRS signal is generated by the interaction of a third pulses, referred to as ′probe′ with optical frequency $\omega_{pr}$, with coherently vibrating molecules. The various CRS techniques differ according to implementation of this second step [66]. Besides being affected by nonlinearities, electronic movements are also deformed by nuclear motions, as previously stated. Typically, this is what happens when nuclear modes from molecular vibrations or symmetric group vibrations are associated with electron movements, which is what happens in this case. CRS takes advantage of this by probing the low-frequency nuclear vibrations indirectly via the much higher-frequency electron oscillations [97].

In a classical framework, the polarizability $\alpha$ describes the interaction between a monochromatic plane wave ($\mathbf{E}(t) = Ae^{-i\omega t} + c.c.$) and the electrons in a medium. The polarizability $\alpha$ is simplified to a scalar term if the pump field and the Stokes field have the same polarization [142]. Therefore, a time-dependent electric dipole moment $\mu(t) = \alpha(t)E(t)$ is induced. In a first approximation, the electronic polarizability can be expanded in a Taylor series near the still position of the nuclei [62]:

$$\alpha(t) = \alpha_0 + \left(\frac{d\alpha}{dQ}\right)_0 Q(t) + \dots \tag{2.43}$$

To the second member of the Eq. (2.43) we wrote two terms: the first, $\alpha_0$, is the zeroth-order approximation of polarizability and it holds true when non-linear effects and/or nuclear modes are not present; the second represents the effects related to the nuclear modes and it is a sort of coupling strength between the nuclear coordinates Q and electronic ones. For $\left(\frac{d\alpha}{dQ}\right)_0 \neq 0$, the polarizability changes and the electron motion is distorted accordingly. Let's consider the simplest case of a system composed by two nuclei, whose motion may be approximated by a harmonic oscillator, exposed to two plane-wave like fields $E_1(t)$ and $E_2(t)$, with frequency $\omega_1 > \omega_2$. If the applied fields intensities are sufficiently high, nonlinear processes become relevant and electronic oscillations are driven at multiple combination frequencies, including at the input fields frequency difference $\Omega = \omega_1 - \omega_2$. In these conditions, the nuclear mode is subjected to a force F(t), that is:

$$F(t) = \left(\frac{d\alpha}{dQ}\right)_0 [A_1 A_2^* e^{i\Omega t} + c.c.] \tag{2.44}$$

where the term $\left(\frac{d\alpha}{dQ}\right)_0$ couples the electronic motions to the nuclear ones. For $F(t) \neq 0$, the oscillating electronic cloud is able to exchange energy with the nuclear mode and the time-dependent nuclear displacement Q(t) can be found as the solution of the equation of motion of the damped oscillator [58]:

$$\frac{d^2Q(t)}{dt^2} + 2\gamma\frac{dQ(t)}{dt} + \omega_v Q(t) = \frac{F(t)}{m} \tag{2.45}$$

where $\gamma$ is the damping constant, m is the reduced mass of the nuclear oscillator and $\omega_v$ represents the resonance frequency of the harmonic nuclear mode, which leads to $Q(t) = Q(\Omega)^{-i\Omega t} + c.c.$, whose amplitude $Q(\Omega)$ is given by [16,30]

$$Q(\Omega) = \frac{1}{m}\left(\frac{d\alpha}{dQ}\right)_0 \frac{A_1 A_2^*}{\omega_v^2 - \Omega^2 - 2i\Omega\gamma}. \tag{2.46}$$

So, the amplitude of the nuclear vibrational mode depends on the amplitudes of the input fields and the strength of the coupling term between the nuclear coordinates Q and the polarizability $\alpha$. In addition, Eq. (2.46) shows that the vibrational amplitude reaches its maximum as the frequency detuning $\Omega$ converges to the oscillator resonance frequency $\omega_v$.

The nuclear harmonic oscillator's classical theory describes how the electronic movements are perturbed, resulting in changes to the optical characteristics of a medium when two input light fields are passed through it. A change in the optical characteristics means a change in the polarization, as presented in Eq. (2.2). Using the result obtained in Eq. (2.43), we obtain:

$$P(t) = N\left[\alpha_0 + \left(\frac{d\alpha}{dQ}\right)_0 Q(t)\right][E_1(t) + E_2(t)] \tag{2.47}$$

In this equation (2.47), we find again two different contributions: the linear ones, associated to $\alpha_0$, and the nonlinear ones, associated to $\left(\frac{d\alpha}{dQ}\right)_0$. As it was foretold, only the latter ones are in charge of the interaction between the input fields (at $\omega_1$ and $\omega_2$ ), which effectively drives the CRS processes. There are 4 possible frequency combinations, which give rise to four distinct polarization components:

$$P_{NL}^{(3)}(t) = P_{CSRS}e^{i(\omega_2-\Omega)t} + P_{SRG}e^{i\omega_2 t} + P_{SRL}e^{i\omega_1 t} + P_{aS}e^{i(\omega_1+\Omega)t} \tag{2.48}$$

where:

- $\omega_{CSRS} = \omega_2 - \Omega$ is the coherent Stokes Raman scattering frequency;
- $\omega_{SRG} = \omega_2$ is the Stokes frequency;
- $\omega_{SRL} = \omega_1$ is the pump frequency;

- $\omega_{aS} = \omega_1 + \Omega$ is the coherent anti-Stokes Raman scattering frequency.

The third-order susceptibility contribution to the Raman interaction may be shown explicitly by expanding the nonlinear polarization. Taking as example the anti-Stokes term $P_{aS}e^{i(\omega_1+\Omega)t}$ , inserting Eq. (2.47) and Eq. (2.43), one obtains the resonant part of the third-order susceptibility, written as [30]:

$$\chi_R^{(3)}(\Omega) = \frac{N}{6m\epsilon_0}\left(\frac{d\alpha}{dQ}\right)_0^2 \frac{1}{\omega_v^2 - \Omega^2 - 2i\Omega\gamma}. \tag{2.49}$$

Eq. (2.49) explicates again that the medium response is maximum when the frequency detuning $\Omega$ approaches the resonance frequency $\omega_v$ of the vibrational Raman mode. When the calculations are repeated for the polarization in relation to the other Raman effect, it is discovered that they all have the same third-order susceptibility. Nonetheless, as will be seen in the next sections, the intensity of the signals emitted by various CRS approaches differs significantly.

#### Coherent anti-Stokes Raman scattering

Coherent anti-Stokes Raman scattering (CARS) is a four-wave mixing process in which two pump fields, at frequency $\omega_p$, and one Stokes fields, at frequency $\omega_S$, with $\omega_S < \omega_p$, partake to generate one anti-Stokes photon, at frequency $\omega_{aS} = 2\omega_p - \omega_S$. A schematic representation of the energy situation is reported in Fig. 2.6. The purpose of this section is to investigate the generation of coherent Raman scattering signals using two temporally and spatially overlapped laser beams [196]. Generally speaking and as already mentioned, CARS process should involve a third field, called the probe field with frequency $\omega_{pr}$, that drives the third and final interaction. However, because of the more accessible implementation scheme, the most widespread excitation geometry involves only two synchronized optical beams instead of three, pump and Stokes beams, and the pump beam is used in place of the probe beam. Therein and in the ensuing discussion, without loss of generality, only the degenerate case of one pump beam, i.e. $E_{probe} \equiv E_p$, and one Stokes be $E_S$ will be examined.

The pump beam, at frequency $\omega_p$, and the Stokes beam, at frequency $\omega_S$, impinge on a Raman-active material with a frequency difference $\Omega = \omega_p - \omega_S$, commonly referred to as Raman shift, that equals the resonance frequency of the vibrational mode of the material $\omega_v$, i.e. $\Omega = \omega_v$. From

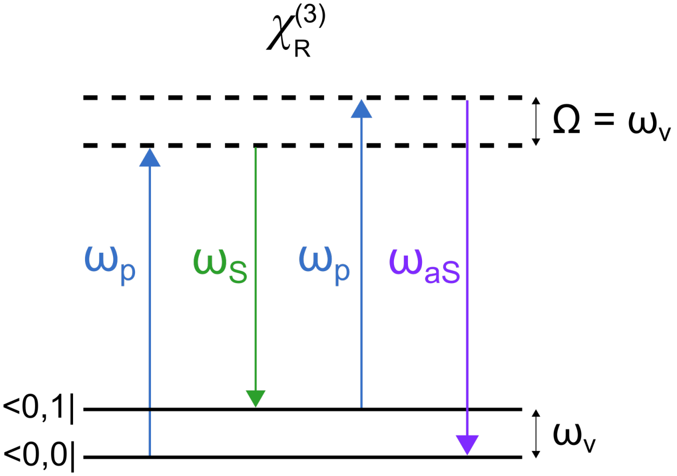

**Figure 2.6:** *Schematic of the CARS light-matter interaction. The subscripts p and s indicate the pump and Stokes fields, respectively. Dashed lines in the Jablonski diagram are virtual levels, solid lines represent real levels*

this interaction, a nonlinear third-order polarization at the anti-Stokes frequency $\omega_{aS}$ arises, generating an optical field at the same frequency ($\omega_{aS}$). This new field is the result of two interactions made by the pump field and the Stokes field via a virtual energy state (depicted with the dashed line in Fig. 2.6), which does not correlate to the system's actual excited state. In this way, a coherent state is generated, given by the superposition of the fundamental state ($< 0,0|$) and first excited vibrational level ($< 0,1|$). Then, a third interaction with the pump field drives the system to the final virtual state where the anti-Stokes photon is emitted. Eventually, the system is driven to the final virtual state by a third interaction with another pump photon, which results in the emission of the anti-Stokes photon.

Under the assumption that the two driving fields, pump and Stokes, are plane waves, sharing the same polarization, and that their amplitude varies negligibly during propagation in the medium, it is possible to derive the anti-Stokes field intensity. Starting from the coupled nonlinear wave equations and after a propagation length L in the Raman active medium, one obtains [30]:

$$I(\omega_{aS}) \propto |A_{aS}(L)|^2 \propto |\chi_e^{(3)}(\Omega)|^2 I_p^2 I_s L^2 sinc^2\left(\frac{\Delta k L}{2}\right) \tag{2.50}$$

where $\Delta k \equiv k_{aS} + k_s - 2k_p$ is the phase-matching term, that originates from the energy and momentum conservation. In order for the radiating CARS signal to be efficiently built up, the phase-matching condition must be met to determine the maximum coherence length $L_c$, namely the length in which the effective coherence is maintained, defined as:

$$L_c = \frac{2\pi}{|\Delta k|} \tag{2.51}$$

Moreover, the phase-matching is highly related to the propagation direction of the field. In the assumption of tight focusing condition, which is a common scenario in forward-detected (F-CARS) microscopy research utilizing high numerical-aperture objectives, for F-CARS signals, the phase-matching condition is automatically fulfilled ($\Delta k \approx 0$), and the small residual wave vector mismatch derives from the dispersion properties of the medium. Consequently, the $sinc$ function in Eq. (2.50) is maximum and the CARS signal intensity simplifies in:

$$I(\omega_{aS}) \propto |A_{aS}(L)|^2 \propto |\chi_e^{(3)}(\Omega)|^2 I_p^2 I_s L^2. \tag{2.52}$$

Some key properties of the CARS signal may be deduced from the latter equation:

- it scales quadratically with the number of Raman scatterers: in fact, it depends quadratically on amplitude of the third-order susceptibility $\chi^{(3)}$ that in turn depends linearly on the number of scattering molecules in the medium. When working with very diluted samples, this is a disadvantage to be aware of;
- it depends quadratically on the laser intensity of the pump beam and linearly on the laser intensity of the Stokes beam;
- it depends quadratically on the interaction length $L$.

Moving to the case of backward-detected (E-CARS) signal, the wave vector mismatch is different from zero ($|\Delta k| = 2k_{aS}$) and corresponds to a really small coherence length $L_c$, lower than a micrometer [30]. This property is deleterious to the signal's constructive interference, which drops fast as a function of $L$ [179]. But, as a result of this, E-CARS signals intrinsically feature a contrast mechanism capable of probing nanoscopic structures, which distinguishes them from F-CARS signals and provides complementary information about the sample [32]. Being $|\Delta k| = 2k_{aS} \neq 0$, in general the $sinc$ term in Eq. (2.50) cannot be placed equal to 1. Consequently, the signal oscillates with a periodicity of $\frac{\lambda_{aS}}{2n}$ and can be written as:

$$I(\omega_{aS}) \propto \lambda_{aS}\, sin^2(k_{aS} L) \tag{2.53}$$

Until now, only the resonant component of nonlinear susceptibility has been taken into account. As seen in Eq. (2.49), $\chi_R^{(3)}$ is a complex quantity whose imaginary and real parts reflect different physical processes: the first reflects the resonant Raman response associated with nuclear vibrational modes and its spectrum has the typical Lorentzian function shape with a maximum at the resonance frequency; the second, that is the real component, has a dispersive-like shape and is connected to the electronic response of the molecules as well as the nonlinear refractive index [21]. When all processes associated with the four-wave mixing mechanism are taken into account, it is discovered that also purely electronic motions at the anti-stokes frequency $\omega_{aS}$ are present. These electronic motions generate a signal that may be overlaid on the resonant CARS signal and, in the far field, even interfere with it, giving rise to a distorted signal. These non-Raman components are represented into the total susceptibility with a non-resonant term called $\chi_{NR}$, which is usually referred to as non-resonant background (NRB). Because only virtual levels are involved in the interactions , the NRB is a real quantity with a flat spectral response, meaning that the nonresonant susceptibility is a real quantity and independent on frequency. Therefore, the total third-order nonlinear susceptibility is equal to the following:

$$\chi^{(3)} = \chi_R^{(3)} + \chi_{NR}^{(3)} = Re[\chi_R^{(3)}] + i \cdot Im[\chi_R^{(3)}] + \chi_{NR}^{(3)}. \tag{2.54}$$

This non-resonant component makes it more difficult to interpret the CARS spectra and, as a result, it determines the lowest level of resonant signal that may be detected. NRB may be generated by the whole specimen, both target and non-target molecules. A biological sample contains several molecules of the solvent, which is often selected because it is optically transparent to the applied fields. Despite this, the molecules of the solvent might nonetheless contribute to the electronic non-resonant susceptibility of the sample. Moreover, also the target molecules contribute to the generation of the NRB, in addition to the intended resonant signal. The possible processes are shown in the diagrams of Figure 2.7.

The total CARS signal is proportional to the square modulus of the total nonlinear susceptibility, and can be written as [71]:

$$\begin{aligned} I_{as} \propto |\chi^{(3)}|^2 = |Re[\chi_R^{(3)}] + i \cdot Im[\chi_R^{(3)}] + \chi_{NR}^{(3)}|^2 = \\ = |Re[\chi_R^{(3)}]|^2 + |Im[\chi_R^{(3)}]|^2 + |\chi_{NR}^{(3)}|^2 + 2|Re[\chi_R^{(3)}]| \cdot |\chi_{NR}^{(3)}| \end{aligned} \tag{2.55}$$

The last two terms of this equation (Eq. (2.55)) clearly show that the presence of the NRB not only adds a constant background to the resonant CARS

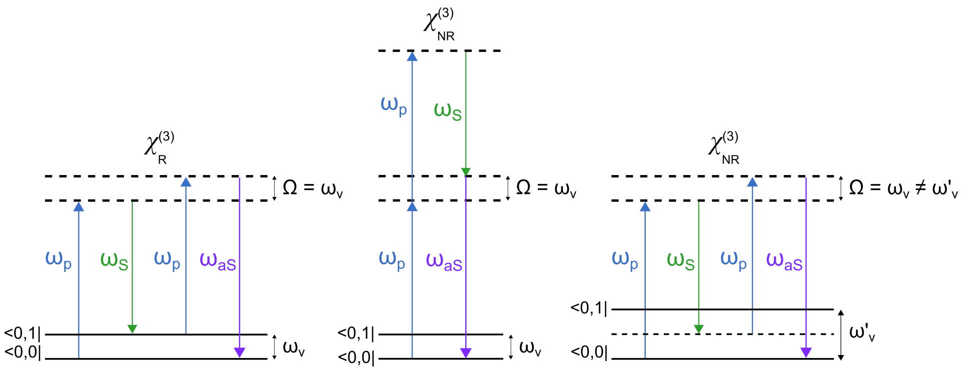

**Figure 2.7:** *Energy diagram showing the transitions driven by the resonant susceptibility compared with the possible four-wave-mixing transitions leading to NRB. The subscripts p and s stand for the pump and Stokes, respectively. Dashed lines represent virtual levels and solid lines real levels.*

signal, readily eliminated by using background removal techniques, but it also produces an interference term, which causes distortion in the CARS resonant signal. In typical biological experiments, the concentration of the target molecules is highly diluted in the specimen. In this scenario, the unfavorable presence of NRB poses some limitations in CARS microscopy and has pushed researchers to find methods for NRB suppression, like polarization-sensitive CARS (P-CARS) [27, 188] and frequency-modulation CARS [98, 126]. A second class of approaches is based on taking advantage of the self-heterodyne amplification of the CARS signal through NRB, to speed up the measurements, together with the use of phase-retrieval algorithms to recover the resonant part of $\chi_3$ [33, 56, 78]. The experiments carried out in the fingerprint spectral region are more affected by NRB than those carried out in the CH-stretch region, due to the inherently weaker signals generated in fingerprint, which are of the order of ten times or weaker than the signals generated in the higher frequency region. Thus, more sophisticated approaches, as those based on deep learning [17, 174], could be employed.

### Stimulated Raman scattering

Stimulated Raman scattering (SRS) is another coherent Raman technique and shares the same excitation modalities as CARS. A narrowband pump laser, at frequency $\omega_p$, and a narrowband Stokes laser, at frequency $\omega_s$, with a frequency detuning $\Omega = \omega_p - \omega_s$ that approaches the molecular vibrational frequency of the sample, induce a transition in the molecule population from the ground state through a virtual state to the vibrationally excited state (Fig. 2.8). As a consequence, the SRS and CARS signals often coexist in the sample and a multimodal setup can retrieve both of them at the same time. While CARS is a parametric process, meaning that it does not produce a deposition of power into the sample and the interacting fields, at the end of the nonlinear process, only exchange power between them, SRS is a dissipative process. In the latter, power is transferred from the pump to the Stokes beam, and an excess of power remains in the sample deposited through molecular vibration, ultimately leading to heat dissipation. Because of the stimulated excitation of the vibrational transition, the molecular transition rate is enhanced in contrast to that in spontaneous Raman. Due to the coherent excitation of molecular vibration, a pump photon is absorbed by the sample, and a Stokes photon is generated, which results in the stimulated Raman loss (SRL) of the pump field and the the stimulated Raman gain (SRG) of the Stokes field (Fig. 2.8), causing intensity changes in the pump and Stokes beams, which carry the same Raman information.

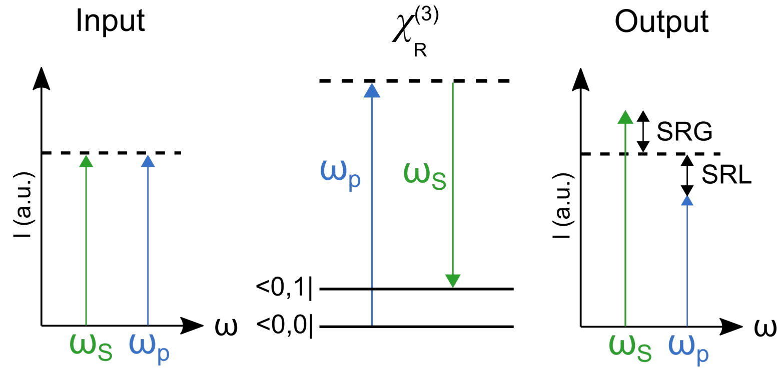

**Figure 2.8:** *Jablonski diagrams of the SRS light-matter interactions. The subscripts p and s indicate the pump and Stokes field, respectively. Dashed lines represent virtual levels and solid lines real levels.*

SRG and SRL may be determined in the plane-wave approximation by solving the coupled-wave equations. For the same reasons as those outlined in the preceding section, here we will consider only the degenerate case of two temporally and spatially synchronized excitation laser beam, pump (at $\omega_p$) and Stokes (at $\omega_S$) (with $\omega_p > \omega_S$), propagating in the forward direction. Because both the SRG and SRL process theories may be deduced in the same manner, only the former will be examined. In SRG, the radiating field oscillates at a frequency similar to the frequency of the incident Stokes field. The wave vector mismatch for the forward-propagating field is $\Delta k = -k_1 + k_2 + k_1 - k_2$, meaning that the phase-matching condition is always automatically satisfied. As a result, and in contrast to CARS, there is no mismatch owing to material dispersion in forward-detected SRG, ensuring always maximum conversion efficiency. Assuming again that the variations of the pump and Stokes fields along the interaction length $L$ are negligible, the plane wave solution for the amplitude of the forward-propagating SRG field can then be written as:

$$\Delta E_s = E_s(L) - E_0 \propto -i\chi^{(3)}|E_p|^2 E_s L \tag{2.56}$$

with $\Delta E_s$ the net gain in the Stokes field after a propagation length $L$ in the medium. The stimulated field's frequency is identical to the Stokes field's frequency and propagates in the same direction, resulting in the following total intensity in the far-field at the detector:

$$\begin{aligned} I(\omega_s) &\propto |E_s(L) + \Delta E_s(L)|^2 = \\ &= I_s + |\chi^{(3)}|^2 I_p^2 I_s L^2 + 2Im[\chi^{(3)}(\Omega)] I_p I_s L, \end{aligned} \tag{2.57}$$

where $I_s$ represents the Stokes beam intensity, which is considered to remain roughly steady throughout the nonlinear process. The second term indicates the intensity of the SRS signal, usually negligible, and the final term reflects the heterodyne amplification of the nonlinearly generated field by the incident Stokes beam. This final term contains the Raman sensitive information, which must be recognized as a gain in intensity on top of the Stokes signal from the laser, which is typically four to five orders of magnitude higher than the SRG. In order to extract this signal, a common technique is to modulate the pump beam at a high frequency and then have the modulation transferred to the Stokes field through the SRS. This transferred modulation may be detected with the use of a lock-in amplifier that is very sensitive. The laser and shot noise are the primary sources of noise to contend with at this point. Thanks to this implementation, it is possible to reject the first term of Eq. (2.57), whereas the second term is typically negligible, overall yielding an SRS signal as:

$$\frac{\Delta I(\omega_s)}{I_s} \propto 2Im[\chi^{(3)}(\Omega)] I_p L \tag{2.58}$$

Some key properties of the SRS signal may be deduced from the Eq. (2.57) and Eq. (2.58):

- it is linearly dependent on the interaction length $L$ and the phase-matching condition is always fulfilled;

- it is linearly dependent on pump field intensity;
- it is linearly dependent on the imaginary part of the third-order susceptibility, meaning it is completely insensitive to NRB;
- it is linearly dependent on the number of probed molecules N, since $Im[\chi^{(3)}(\Omega)] \propto N$;
- it is linearly dependent on the Raman cross-section $\sigma_{Raman}$, because $Im[\chi^{(3)}(\Omega)] \propto \sigma_{Raman}$. Therefore, the spectral shape of the signal is comparable to the spectra available in literature collected with spontaneous Raman [142].

## 2.3 Biological Specificity of Nonlinear Microscopy techniques

### 2.3.1 Two-photon excitation fluorescence microscopy

Two-photon excited fluorescence (TPEF) microscopy of intrinsic fluorophores yields physiological and pathological information from biological tissues at subcellular resolution. Reduced nicotinamide adenine dinucleotide (NADH) and flavin adenine dinucleotide (FAD) are two endogenous fluorescent coenzymes on the intracellular scale. Autofluorescence images of NADH and FAD have been applied to record changes during metabolism noninvasively, according to their distributions and concentrations, and monitor metabolism-related physiological and pathological processes, such as cell differentiation and cancer development [166]. Elastin is the protein that gives vertebrate tissues their unique elastic characteristics [77]. Its elastic property complements the tensile strength imparted by collagen fibrils, and both proteins are frequently found together in connective tissue. Elastin, like collagen, is a major extracellular source of fluorescence emissions, and both proteins display significant overlap in their endogenous fluorescence signals, making them practically indistinguishable with traditional linear microscopy. Although the two proteins perform complementary biological roles, they are very unlike in structure, with elastin lacking the non-centrosymmetric structure required for SHG. By using this, the right selection of excitation wavelengths in conjunction with spectral filtering enables the isolation of collagen and elastin signals in TPEF microscopy [193,195]. Moreover, TPEF was used in a number of investigations to identify changes in endogenous fluorescence emissions as a marker for the occurrance of photodamage. In fact, photodamage is often linked to an increase in the NADH two-photon autofluorescence [6,55,171].

### 2.3.2 Second-harmonic generation microscopy

SHG offers an effective contrast mechanism for imaging cellular and tissue structures exploiting the physics of second-order light-matter interactions [193]. For an effective generation of SHG signal, the sample under observation shall have non-centrosymmetric structures on the scale of the wavelength of the second-harmonic radiation, namely $\lambda_{SHG}$. For imaging well-ordered structures such as fibrillar collagen, this characteristic is particularly advantageous. Because this criterion is not satisfied, other structural proteins such as nonfibrillar collagen, laminin, fibronectin, and elastin are transparent when using this technique [75]. Using SHG, researchers have been able to see the supramolecular assembly of collagen in tissues at a previously unimaginable degree of detail [22]. Collagen triple helix and collagen fibrils are organized in tightly aligned repeating structures within fibrillar collagen. As a result, fibrillar collagen is highly anisotropic and the emitted SHG signal is coherently amplified. A fascinating property of SHG that contributes to its success in biological investigations is its polarization sensitivity. As a result, the SHG signal strength depends on the polarization state of the incoming laser light in comparison to the spatial distribution of the radiating molecules [121]. Thus, the intensity of the SHG signal generated by a collagen sample in an imaging experiment is dependent not only on the concentration of proteins stimulated in the focal volume, but also on the polarization state of the incident radiation in relation to the orientation of the fiber axis, as illustrated in Fig. 2.9. Therefore, the SHG signal's polarization dependency may be used to investigate the tissue's collagen fiber orientation [186, 194].

### 2.3.3 Stimulated Raman scattering microscopy

SRS microscopy technique is gaining popularity in biology and histology. Based on observation of their vibrational spectrum, we can distinguish the four main biological macromolecules, *i.e.* proteins, nucleic acids, lipids, and carbohydrates, as each spectrum is characterized by specific Raman peaks. Thus, Raman spectroscopy offers information on a biological system's phenotype [143].

Typically, the Raman spectrum of a biological sample may be divided into three regions: the fingerprint spectral region (400-1800 $\mathrm{cm}^{-1}$), which comprises the most peculiar and chemically specific information; the silent spectral region (1800-2700 $\mathrm{cm}^{-1}$), that usually does not present vibrational modes contributed by biomolecules; and finally the CH-stretch region (2700-3200 $\mathrm{cm}^{-1}$), where the macromolecules, predominantly lipids and proteins,

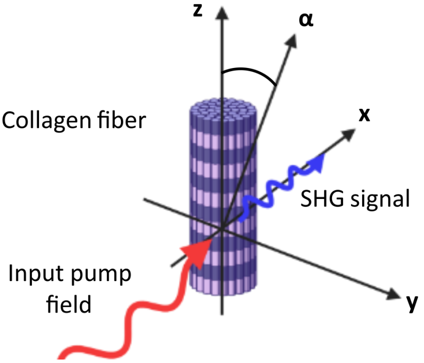

| Collagen fiber | Laser polarization | SHGsignal |
|---|---|---|
| <br>Cross section<br>(centrosymmetric) | ↔ ↕<br>parallel/perpendicular | None |
| <br>axial<br>(non-centrosymmetric) | ↔<br>parallel | Strong |
|  | ↕<br>perpendicular | Weak |

**Figure 2.9:** *Illustration of the orientation of a single collagen fibre relative to an applied electric field. The emitted SHG signal (in blue) possesses double the energy of the incident field (in red). The maximum SHG signal is observed when the incident light is polarized along the collagen fibre axis (z); if it is polarized perpendicular to the fibre axis (x), the emitted signal is weak; if the collagen fibre is oriented along the direction of propagation of the field, no SHG signal will be observed [121].*

resonate through the stretching vibrations of the CH groups. Appropriate experimental Raman shifts must be chosen, in order to investigate the Raman modes associated to the major biochemical classes of tissue and cellular specimens. For example, to detect lipids and proteins, the frequency detuning between pump and Stokes beams should be set at 2850 $cm^{-1}$ and 2920 $cm^{-1}$, respectively, being the Raman shift resonant with atomic groups $CH_2$ and $CH_3$ [76, 103, 125].

# CHAPTER 3

# Characterization of HeLa cells response to NIR ultrashort laser pulses

This chapter presents the experimental study of photodamage induced on viable HeLa cells exposed to NIR ultrashort pulsed laser light.

## Introduction

It's impossible to speak about biological multimodal nonlinear optical microscopy without considering the detrimental effect that laser radiation could have on biological samples. The recent introduction of ultra-short pulsed laser sources has led to an incredible improvement in microscope imaging capabilities, making possible for example the direct observation of dynamic cellular processes [23, 193]. New microscopy techniques have been introduced, such as super-resolution microscopy, which allowed to break the diffraction limit, reaching resolutions never reached before [9, 60, 119]. Thanks to these technological advances, the nonlinear optical microscopy has emerged as one of the preferred tools for answering complex biological questions. Considering the high-intensity illumination required by innovative microscopy techniques, this made it necessary to deepen our knowledge on photodamage mechanisms to preserve the specimen under observation [94]. In fact, avoiding phototoxicity represents an essential and insufficiently understood bottleneck for *in vivo* biomedical imaging [86, 88, 134].

We use the word "phototoxicity" to refer to the harmful effects of light on living biological systems. It is a multifaceted phenomena comprised of wavelength-dependent photophysical processes that may result in the production of highly reactive photochemical compounds, the generation of heat, and the destruction of DNA [36, 74]. There are three types of photodamage mechanisms: photothermal, photochemical and multiphoton ionization. Each type of damage has its well-defined characteristics and will be deepened in the next section (Section 3.1). Whereas defining phototoxic processes is rather easy, assessing phototoxicity in microscopy applications is a whole different story [172]. One of the biggest difficulties in dealing with phototoxicity is having to control a large amount of factors simultaneously. In fact, severity and type of damage induced depends on the experimental parameters related to the laser source (such as wavelength, laser power, pulse duration, etc.) and to the illumination configuration (exposure time, scanned or stationary exposure, etc.) and clearly the effects are specific to the type of sample examined [29, 54, 68, 105, 149]. In addition, radiation adverse effects can be both short- and long-term, and their evaluation and identification is a challenging subject for which a variety of approaches have been developed. For example, effective ways to detect sample damage directly during microscopy application are to measure photobleaching and irradiation-induced fluorescence [55, 134]. Alternatively, many specific tests have been developed to target particular damage such as ROS and free radicals production, DNA strand breaks, changes in metabolic activity and in cell morphology, stress-related proteins, cloning efficiency and level of apoptosis [42, 43, 69, 148, 165, 167].

In bioimaging, the aim is to acquire pictures with appropriate contrast, spatial and temporal resolution paying attention not to affect in any way the biology of the sample under observation. Unfortunately these three factors are all interdependent and to optimize them it is often necessary to increase the light exposure, in terms of time or power, negatively impacting on the health of the sample. But with the advancement of technology and new perspectives in biomedicine, the preservation of sample health is becoming increasingly important. Due to the detrimental effect of radiation on samples, the data collected during the experiments will not be reliable, but will only be a representation of the cellular response to radiation, leading to incorrect conclusions. [94]. Many studies have been carried out in this field [38, 74, 84, 94, 172], but there are still several concepts to grasp to develop a comprehensive theory of photodamage, owing to the topic's complexity, a large number of variables, and incapacity to investigate them all.

To be consistent with our work, the rest of this introduction will be devoted to the brief presentation of the most important results obtained on label-free cultured cells present in the literature and relevant for nonlinear optical microscopy applications. A very interesting study was conducted by Nan and colleagues [122], who demonstrated the possibility of performing CARS measurements without perturbing cells under observation. They studied the onset of linear and nonlinear damage varying pulse energy and average laser power. The wavelengths of their pump and Stokes laser beams were 711 nm and 892 nm respectively, with 2 ps of pulse duration. They obtained a linear damage threshold for average power between 9 mW and 12 mW, using low pulse energy (<1 nJ). On the contrary, they used high pulse energy (>1 nJ) and low average power (< 5 mW) to characterize the nonlinear damage obtaining a pump pulse energy threshold between 2 nJ and 3 nJ with a repetition rate of 1 MHz, and a pump pulse energy threshold between 1.5 nJ and 2.3 nJ with a repetition rate of 2 MHz. Ultimately they proposed 1.5 mW (8 MHz, 0.2 nJ) for the pump and 0.5 mW (8 MHz, 0.06 nJ) for the Stokes as safety working conditions to performe CARS microscopy. Fu and coworkers [54] have set themselves the ambitious goal of defining guidelines to accomplish high-quality biological CARS microscopy images preventing photodamage. They studied the photodamage rate as a function of laser power, excitation wavelength and repetition rate. In addition, they observed and characterized the enhancement of the damage induced by the vibrational absorption at the Raman resonance, also called 'coherent Raman induced' photodamage. They employed a pump and a Stokes beam at 704 nm and 808 nm respectively, and they observed that a total average power of 9.24 mW was sufficient to induced harsh damage in cells after an exposure of 60 s, while with a total average power of 2.3 mW the cells have not reported any damage after an exposure of 600 s. Always staying on CARS microscopy but considering its wide-field declination, Silve et al. [158] shown the feasibility of acquiring CARS images of suspended live cells. They employed a pump and a Stokes beam at 625 nm and 770 nm, with pulse duration of 4 ns and 3 ns, respectively and at a repetition rate of 10 Hz. In their experiment, the cells sustained exposure to 3000 pulses of pulse energy 1.2 mJ and 0.53 mJ (pump and Stokes) without damage. Moving to the other coherent Raman microscopy technique, Freudiger and colleagues [51] finely tuned the experimental parameters for SRS microscopy of biological samples. They employed a pump and a Stokes beam at 817 nm and 1064 nm, and a 1.2 NA objective. Varying pulse duration (180 fs, 1 ps and 6 ps), they quantified empirically a damage threshold value for average laser power for each pulse duration studied: 25 mW, 80 mW and 280 mW, respectively. Furthermore, they proposed an empirical formula to calculate the maximum value of total average power to prevent photodamage. Eventually Waldchen et al., using three distinct cell lines and designing ad-hoc experiments, produced a detailed study on photodamage of living cells, evaluating the effects of irradiance, wavelength, light dosage, fluorescent labeling, temperature, and reducing agent on the survival of labeled and unlabeled cells [181]. They demonstrated that shorter excitation wavelengths correspond to more severe damage. In fact, shifting the excitation wavelength from 488 nm to 514 nm for the same irradiance of 0.2 kW/cm$^2$, the survival rate of label-free cells exposed to cw radiation for 240 s went from 0% to 100%.

This chapter begins with an overview on photodamage mechanisms, followed by a brief summary of the main results obtained in this field, relevant for non-linear optical microscopy applications. Then an experimental investigation of photodamage caused by focused ultrashort (130-fs) laser pulses on HeLa cells is presented. The cells were exposed to two distinct illumination configurations while the laser power, scanning speed and exposure period were varied. The findings are studied using a data-driven method, and they include an analysis of the underlying phototoxic process as well as an empirical model for imaging without compromising the observed sample,in the range of parameters investigated. Looking at the relationship between the damage and the applied laser power, we found that it was mainly photothermal damage, and this was verified by thermodynamic considerations as well. Based on our studies, we were able to determine the sample damage probability as a function of the factors investigated, and we identified a safety threshold that may be utilized for microscopy applications to ensure that the risk of damage is less than 5 percent.

## 3.1 Photodamage mechanisms

Photodamage mechanisms may be triggered by either linear or nonlinear optical processes [89]. This section provides a short summary of photodamage processes, beginning with the linear mechanisms that occur at low light intensities and progressing to the more damaging nonlinear mechanisms that occur at increasing intensities. In laser physics, the term "intensity of radiant energy" refers to the amount of power delivered per unit area (W/m$^2$). In this chapter, I shall use the word irradiance to refer to the average laser intensity, to be consistent with photometric terminology.

Linear photodamage is mostly generated by sample heating caused by laser irradiation [102], referred to as *photothermal* damage, but it may also be coupled with *photochemical* damage [159]. This is mainly true for pigmented molecules and tissues [37, 112, 128], such as skin. Samples with this feature undergo linear absorption of incident photons, especially if illuminated with visible or ultraviolet (UV) radiation. Increasing light intensity, nonlinear photodamage mechanisms come into play, which for example could be induced by multiphoton absorption [70, 90]. The most frequent nonlinear phototoxic mechanism is photochemical damage, which is associated with the generation of reactive oxygen species (ROS) and free radicals [15, 91]. Nonlinear excitation of cellular and tissue absorbers such as porphyrins, flavins, and coenzymes such as NAD(P)H results in the creation of these hazardous species. Cells have a variety of systems in place to deal with ROS generation under physiological settings. Sometimes exposure to radiation can lead to ROS overproduction, such as to compromise redox homeostasis and cell cycle [19]. Apart from ROS production, cells can suffer direct DNA photodamage [15, 110, 155], and molecular ionization can result in the formation of low-density plasma if the irradiance exceeds the value of $\sim 6 \cdot 10^{12}$ W/cm$^2$ for an NIR femtosecond pulsed laser beam [91, 176]. Finally, once the plasma is no longer constrained, optical breakdown happens, resulting in instantaneous mechanical devastation of biological samples [54, 81, 177, 178].

## 3.2 Materials and Methods

In this section sample, protocols, procedures and experimental setup used in this experimental study will be presented in a detailed way.

### 3.2.1 HeLa Cell

In this work, we decided to use HeLa cells, the first immortalized human cancer cell line, for two main reasons. Firstly, these cells better withstand external stressors, and this is very important for us considering the logistics of our laboratories. Secondly, due to some of their peculiar characteristics, such as availability and ease of handling, they have been widely used in the literature for characterization and damage studies [118, 181].

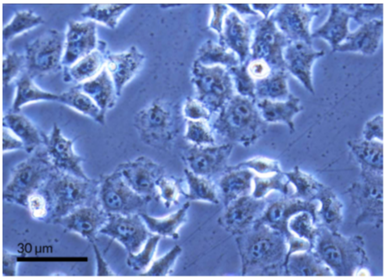

**Figure 3.1:** *Bright-field image of HeLa cells.*

They have been the subject of heated controversy over the years. From an ethical point of view, the cells were harvested and used without the consent of the patient, Mrs Henrietta Lacks. No human specimen had ever been reproduced and used so extensively, and it was not customary to seek written permission from patients. In addition, by choosing the name as a union of the first two letters of the first name (Henrietta) and the first two letters of the last name (Lacks), they did not maintain the anonymity of the donor. From a scientific standpoint, the ability of HeLa cells to survive and reproduce, and their widespread, and sometimes careless, use in every biological research laboratory, has led to the enormous problem of cell line cross-contamination, inter- and intraspecies. This phenomenon has become so pervasive that it is now estimated that $\sim 20\%$ of cell lines are falsely labelled [113]. Despite the controversy, HeLa cells continue, and will continue, to play a major role in scientific research. So, we decided to characterize their survival rate to NIR ultrashort pulsed laser light exposure.

### 3.2.2 Cell culture

HeLa cells are cultured in Dulbecco's modified Eagle's medium (DMEM) supplemented with 10% fetal bovine serum, 1% L-glutamine (2 mM), penicillin (10 units/ml), and streptomycin (10 $\mu$g/ml) at 37°C and in 5% $CO_2$ atmosphere (Euroclone, Italy). The culture medium is changed every 2-3 days. Cells are seeded in gridded cell-culture Petri dishes (IBIDI, 35 mm $\mu$-Dish Grid-500). The effective area disposable for the cell adhesion is 40 mm$^2$. The cells are stored in the incubator until the 100% confluence condition is reached, then they are ready to be used for our experiments [167].

### 3.2.3 Cell staining

For the survival essay, we used a live/dead cell double staining kit consisting of calcein-acetomethoxy (AM) 0,2 $\mu$L/mL (excitation at 473 nm, emission at 490-590 nm) and ethidium homodimer-1 0,5 $\mu$L/mL (excitation at 559 nm, emission at 570-670 nm) (ThermoFisher Scientific, Italy). Just before laser exposure, the cell culture medium is replaced with a DMEM solution containing the two fluorescent dye, calcein-AM and ethidium homodimer-1, which are able to distinguish live and dead cells. Specifically, the calcein-AM is carried into living cells through the cellular membrane, thereby colouring them green. By contrast, the cell membrane is impermeable to ethidium homodimer-1. This fluorescent dye has the characteristic to attach to DNA, but it can only penetrate cells with damaged membranes, i.e dead cells, colouring them in red.

The staining procedure involves some washing steps of the cell sample to remove the DMEM and to add the medium containing the dyes. Initially we carried out this procedure just after laser exposure, but we noticed that many cells damaged or stressed by the radiation tended to detach from the Petri dish, compromising the analysis of the result of the experiment. Therefore, we opted to add the dyes before laser irradiation experiments.

The introduction of fluorescent probes can have a substantial impact on light absorption and therefore change the outcome of the study. So we checked in the literature and there is no indication that calcein-AM and ethidium homodimer may contribute to photodamage. To exclude a possible two-photon absorption of the fluorophores during laser irradiation, we considered the two-photon excitation spectrum of the two dyes. To the best of our knowledge, the two-photon excitation spectrum of calcein is unfortunately reported in literature just in the range 700-950 nm, by Peter and colleagues [135]. However, in this paper the authors reported that fluorescein is a very similar parent compound of calcein-AM, and it displays a very small two-photon absorption cross section at our wavelength (1040 nm), below 10 GM. Going to consider the ethidium homodimer-1, this too presents a small two-photon absorption cross section [124]. In addition, we also verified experimentally that the introduction of dyes did not affect our experiment by comparing the results obtained with both procedures (i.e. adding the dyes before or after laser exposure). Fig. 3.2 shows two images obtained by inserting the dyes after laser exposure (panel A) and before laser exposure (panel B). In both cases the illumination was carried out with the same settings. The black areas, where the cells have detached from the Petri dish after changing the culture medium, are clearly visible in Fig. 3.2A. As highlighted in the red box, comparing the experimental points not affected by cell detachment, the damage obtained for the sample with calcein-AM and ethidium homodimer (Fig. 3.2B) is perfectly consistent with that obtained for the sample irradiated before adding the probes (Fig. 3.2A). Therefore, we are extremely confident regarding the negligible impact of cell staining on phototoxicity, which made us conclude that the best protocol was to add them before laser irradiation, to avoid cell detachment during the washing steps.

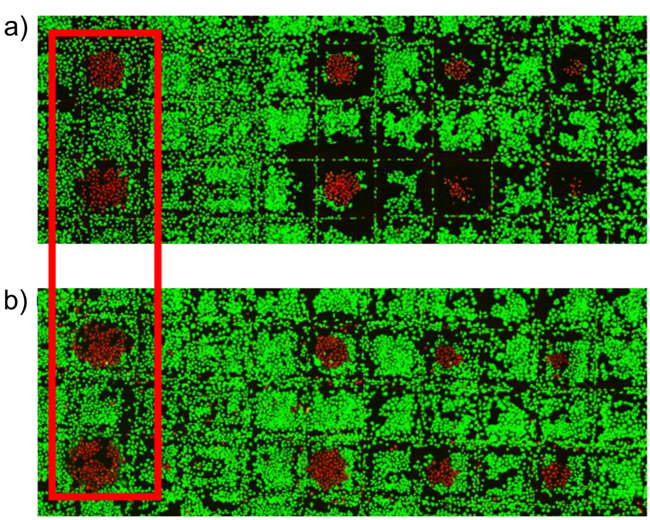

**Figure 3.2:** *Experimental images obtained by inserting the dyes after laser exposure (panel a) and before laser exposure (panel b). In the red box, comparison of experimental points not affected by cell detachment that demonstrate the negligible impact of fluorescent dyes on photodamage in this experiment.*

### 3.2.4 Cell irradiation - Experimental setup

In this subsection a clear presentation of the experimental setup used to expose cells to laser radiation will be provided, starting from the hardware components (laser source, excitation optics, etc.) and ending with software.

**Ultrafast Pulsed Laser Source**

This setup uses a Fidelity HP (Coherent, USA) ytterbium-doped fiber laser which uses a master oscillator power amplifier (MOPA) architecture. This laser source provides light at 1040 nm, with repetition rate of 80 MHz, pulse duration 130 fs, a negative group delay dispersion variable from 0 to -120000 fs$^2$ and up to 18 W of output power [167].

### Excitation optics

Some of our experiments were carried out by scanning the laser beam in a pattern over the sample. In order to prevent distortion phenomena like vignetting, laser scanning should be implemented such that the beam's incident angle vary while remaining centered on the objective's back aperture. There are many ways to accomplish this: we choose a fast galvanometric mirror (GVS311/M, Thorlabs, Germany) just for one lateral dimension. The scheme of the laser scanning system is sketched in Fig. 3.3. This configuration is a double-sided telecentric system and is known as 4f relay system due to the position of the relay lenses. The first relay lens is placed one focal length after the scan mirror, the second relay lens is placed one focal length before the objective back aperture, and the relay lenses are separated by the sum of their focal lengths [191]. In this way, the chief rays for any scan angles are parallel between the relay lenses and the beam, during the scan, remains in the limits of the objective's back aperture.

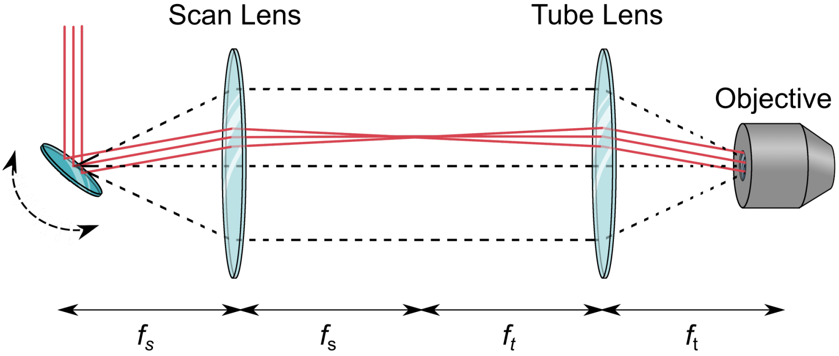

**Figure 3.3:** *Schematic representation of a laser scanning system in the paraxial approximation. A collimated beam impinges on a beam scanning device, in this case a galvanometric mirror, that is placed in the back focal plane of the so-called scan lens, of focal length $f_s$. A second lens of focal length $f_t$, named tube lens, is positioned in 4f configuration with respect to the scan lens to image the galvo mirror to the back aperture of the objective, as pointed out by the red dashed lines [191].*

As the last element of the excitation system, the one responsible for focusing the beam on the sample, we employed two different optics. In the experiment described in Section 3.3, the sample was illuminated by holding the laser beam at a fixed point, and in this case we used a lens with focal length $f = 30$ mm. Instead, in the experiment presented in Section 3.4, we opted for a scanning illumination configuration and we employed a objective (Melles Griot) of 0.25 NA and 10x magnification. We experimentally measured the spot size focused on the sample using the knife-edge method. In the first case we obtained a spot with a radius of 15 $\mu$m, calculated as half width at half maximum (HWHM), while in the second case we obtained a smaller spot with a radius of 6 $\mu$m, again calculated as HWHM. We purposefully picked these two optical elements to avoid the difficulty associated with the laser beam waist's vertical location relative to the cell plane. The Petri dish's thin (170 $\mu$m) glass bottom often exhibits thickness fluctuations. Additionally, it is not exactly flat owing to tensions or bending caused by gravity. As a consequence, maintaining the laser focus on the cells while scanning the sample across vast fields of view with a high-numerical aperture objective is rather challenging. We overcame this issue by using a low-NA objective and a lens with a long depth of focus, resulting in excellent repeatability.

#### Scanning system

The scanning system is made up by two different parts. The first one is the galvanometric mirror, already presented in the previous subsection, and the second is an x-y motorized translation stage (8MTF-75LS05 Standa, Lithuania). The galvanometric mirror is controlled by the driving waveform and it produces a deflection of the beam back and forth along one direction. The sample holder is mounted on the 2-axis motorized stage that moves the sample in the $xy$-plane with a resolution (min step size) of 1/8 of 2.5 $\mu$m and that is controlled by a software. The combination of the galvanometric mirror, the 2-axis moving stage and of a shutter turns out to be an extremely flexible scanning system and it enables us to realize and change easily different scanning patterns, according to the aim of the experiment. With this implementation we obtain a serpentine scan (shown in Fig. 3.4). For the y direction we use the galvanometric mirror, whereas for the x direction we use the motorized translator.

#### Collection and detectors

After the sample holder, another $4f$ relay system is placed, in order to make the generated signal impinge on a photodiode. In this setup we used a PDA10CS(-EC) (Thorlabs, Germany), a photodetector sensitive to light in the NIR wavelength range (800-2600 nm) and with switchable gain.

#### Additional information

All the lenses used in the microscope are B-coated (Thorlabs, Germany) and are specific to wavelength range 650-1050 nm with a reflectance less

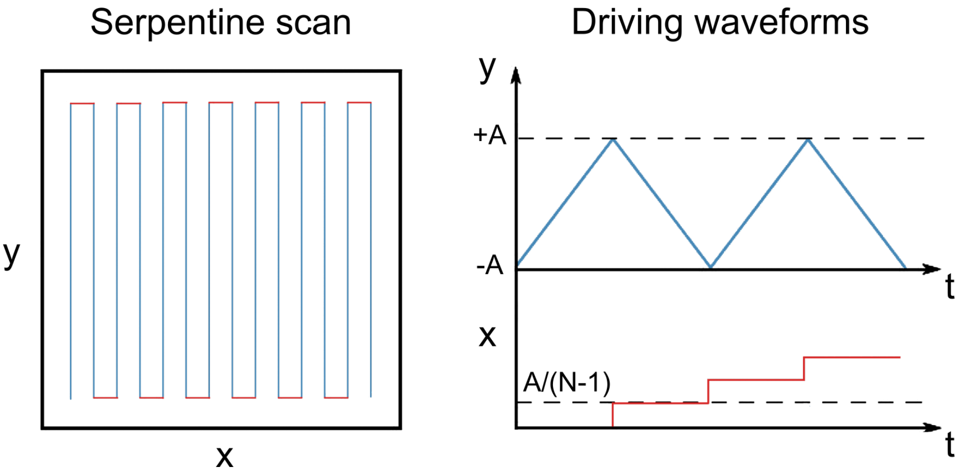

**Figure 3.4:** *Serpentine scan. On the left of the figure is shown the pattern and on the right are presented the correspondent driving wave-forms for both x and y directions. Parameter A represents the width of the scanning area, in this case intended as square, while N is the number of ramps of the y waveform that one wants to employ in the scanning procedure.*

than 0.5% in this range. This microscope provides also the possibility to perform imaging with white light (bright-field). This is a very useful tool because it allows one to inspect the sample before the measurement and to make sure that the focus is on the sample using a linear translation stage along z-axis (the sample holder is mounted on it, and both of them are mounted on the motorized two-axis translation stage). In this configuration the white lamp is placed on the opposite side of the sample with respect to the laser source and a beam splitter deflects the beam towards a Thorcam (Thorlabs), a CCD with 1024x768 pixels. With the Thorcam, we have a FOV of 200x266 $\mu$m. Illuminating from above is the best choice because it allows us to move only the sample (when we find focus), leaving the objective and all the optics fixed. A picture of the experimental setup is provided in Fig. 3.5.

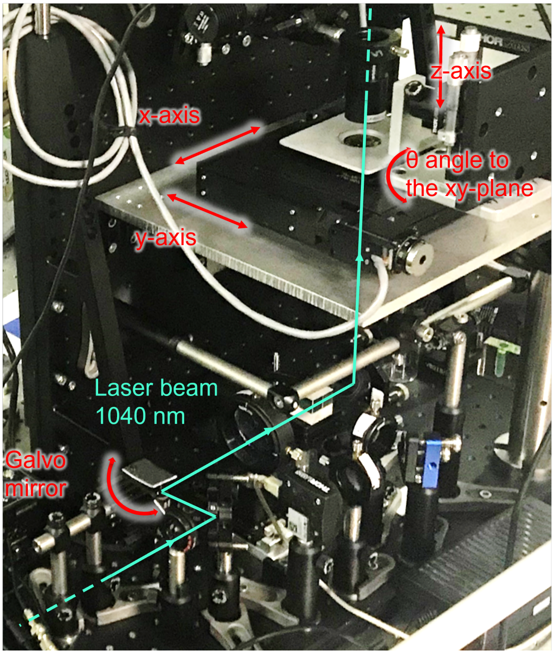

**Figure 3.5:** *Picture of the experimental setup used to characterize the HeLa cell response to NIR ultrashort laser pulses.*

### Software

We interact with this setup mainly through a custom software programmed with the National Instrument software LabView (https://www.ni.com/shop/labview.html). The main functions that we used during the experiments are:

- **Move Standa:** this allows us to move the sample holder in solidarity with the motorized translator stage. The shift can be carried out in the x and y directions, by a definite amount and with a certain speed.
- **Move MCL:** this allows us to move the sample holder in the z direction, to place the sample on the correct focal plane.
- **Test parameters:** this function allows us to carry out a laser scan of a portion of the sample. The parameters of interest that can be set are the size of the scanned area, the scanning speed and the number of horizontally scanned lines. When the measuring process is started, the function automatically moves the sample holder so that the laser scans the defined area according to the scanning pattern shown in Fig. 3.4.

- **Free Galvo:** when using this function, the laser beam scans a line back and forth on the sample, while the screen shows the transmission plot of the laser over the scanned line. The lengthof this line is defined by the user. If on the path of the laser there is a portion of the sample that blocks the beam, then the screen will show a corresponding gap in the transmission profile. We used this function to infere the size of the laser spot from the sharpness and the slope o the gap in the transmission plot.

Additionally, the software allows us to open and close the laser shutter and see and control the settings of the image of the sample acquired by the Thorcam. An image of the software interface is provided in Fig. 3.6.

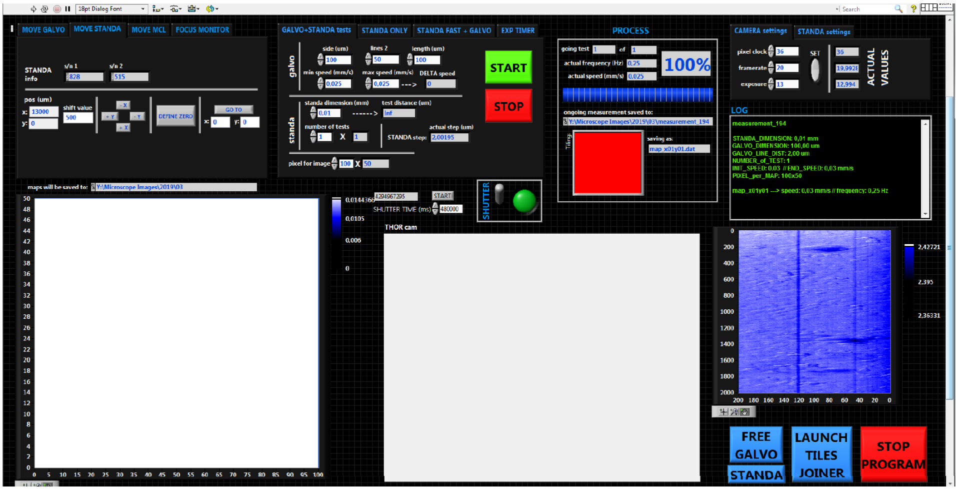

STANDA info s/n 1: 828 s/n 2: 515

pos (um) x: 13000 y: 0

shift value: 500

x: 0 y: 0

maps will be saved to: Y:\Microscope Images\2019\03

side (um): 100 lines 2: 50 length (um): 100

min speed (mm/s): 0,025 max speed (mm/s): 0,025 ---> DELTA speed: 0

standa dimension (mm): 0.01 ------> test distance (um): Inf

number of tests: 1 X 1

actual step (um) STANDA step: 2,00195

pixel for image: 100 X 50

4294967295 START

SHUTTER TIME (ms): 480000

going test 1 of 1

actual frequency (Hz): 0,25

actual speed (mm/s): 0,025

ongoing measurement saved to: Y:\Microscope Images\2019\03\measurement_194

saving as: map_x01y01.dat

pixel clock: 36 → 36

framerate: 20 → 19,9928

exposure: 13 → 12,994

```
measurement_194

 STANDA_DIMENSION: 0,01 mm
GALVO_DIMENSION: 100,00 um
GALVO_LINE_DIST: 2,00 um
NUMBER_of_TEST: 1
INIT_SPEED: 0,03  // END_SPEED: 0,03 mm/s
PIXEL_per_MAP: 100x50

map_x01y01 ---> speed: 0,03 mm/s // frequency: 0,25 Hz
```

**Figure 3.6:** *LabView software interface used to control the experimental setup.*

### 3.2.5 Confocal microscopy

After exposing the cells to laser radiation, the onset of damage is assessed using a confocal microscope (Olympus Fluoview FV10i). This microscope is endowed with four diode lasers at emission wavelengths of 405 nm, 473 nm, 559 nm and 635 nm, an integrated incubator, and with a phase-contrast objective of 0.4 NA and 10x magnification. This translates into the possibility to acquire an image of 1.2×1.2 mm$^2$. The pinhole was set to 2.5 Airy Unit. As the linear absorption and emission spectra of the fluorescent dyes are different, it is possible to distinguish live and dead cells by acquiring two-colour images. Calcein-AM, used to mark live cells, is excited with the laser diode with 473 nm wavelength, and the emitted one-photon fluorescence signal is collected in the band 570-670 nm. In contrast ethidium homodimer-1, the marker for dead cells, is excited using the laser at 559 nm wavelength and emits a linear fluorescent signal in the band 570-670 nm. As several experimental points were acquired in each Petri dish, multi-area images were acquired on the samples to cover the whole area actually exposed to the laser radiation. In order to analyse the images, we decided to act on two different aspects: on the one hand, we counted the live and damaged cells in the areas actually exposed to the laser, and on the other hand, we measured the extent of the damaged zone. To do this, we used the open-source software *ImageJ* [1].

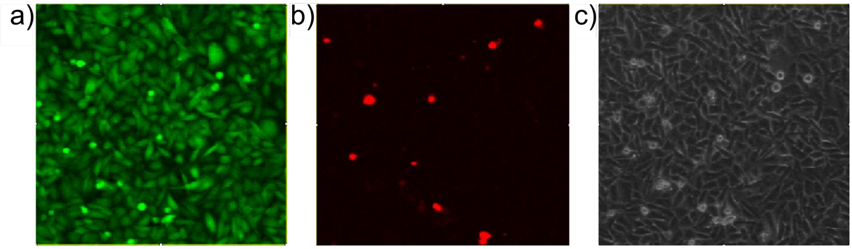

**Figure 3.7:** *HeLa cells imaged with confocal microscope: a) alive cells stained with calcein-AM fluorescent dye, b) dead cells stained with ethidium homodimer-1 fluorescent dye, c) phase constrast view.*

## 3.3 Cell response to fixed laser exposure

In the first experiment we conducted, we applied a fixed illumination modality, i.e. we held the laser in a fixed position on the sample for a defined time (Fig. 3.8a). In this configuration, we studied cell viability as a function of exposure time $T_{exp}$ and irradiance $I_{avg}$. On each sample we created a pattern of 6x6 irradiated points, each 1 mm apart. Each point was exposed with a different combination of the two parameters under analysis. In particular, a range from 15 seconds to 8 minutes was explored for the exposure time, with intermediate values progressively doubled. For the irradiance we used values between 0.3 MW/cm$^2$ and 1 MW/cm$^2$. Fig. 3.8b shows the image obtained with the confocal microscope of a sample after it has been exposed to the laser. By looking at the damaged areas on the sample, the irradiation pattern can be recognised. The complete list of parameters used in this experiment, both fixed and variable ones, can be seen in Table 3.1.

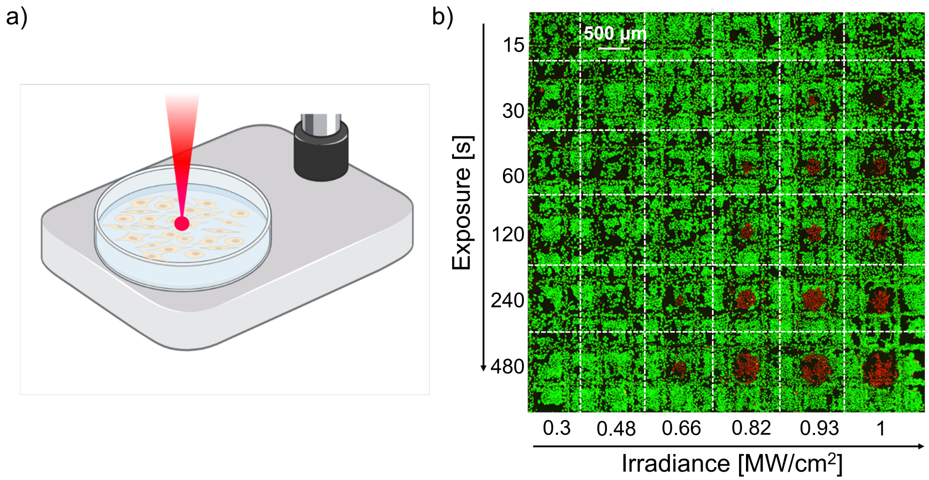

**Figure 3.8:** *Fixed laser illumination modality. a) Schematic representation of the illumination configuration. The laser beam is held fixed at a point on the sample. b) Image, obtained using the confocal microscope, of a sample after laser exposure. Due to the presence of the fluorescent dyes calcein-AM and ethidium homodimer-1, alive cells are stained in green and dead cells are stained red. A pattern of 6x6 points, each with increasing values of exposure time and irradiance, was exposed to the laser on the sample. Adapted with permission from [167] ®Optica Publishing Group.*

***Experimental parameters***

| **Parameter** | **Value** |
|---|---|
| **Irradiance - I$_{avg}$** | [0.3 - 1] MW/cm$^2$ |
| **Exposure time - T$_{exp}$** | [15 - 480] s |
| **Average Laser power - P$_{avg}$** | [2.26 - 6.97] W |
| **Energy per pulse - E$_p$** | [28 - 87] nJ |
| **Peak power - P$_p$** | [217 - 670] kW |
| **Spot radius** | 15 $\mu$m |
| **Pulse length - $\tau$** | 130 fs |
| **Repetition rate - f** | 80 MHz |
| **Wavelength - $\lambda$** | 1040 nm |

**Table 3.1:** *Experimental parameters used in fixed laser illumination experiment.*

As reported in Table 3.1, we irradiated the sample with a laser spot of 15 $\mu$m radius at FWHM. Following the standard procedure employed in laser physics, in Subsections 'Damage probability: a binary problem' and 'Extension of the damage: a continuous problem' we approximated the laser spot as a circle with a diameter of 30 $\mu$m, which is the FWHM of the

Gaussian spot experimentally calculated with the knife-edge method. This approximation allows us to consider irradiance, or average laser intensity, deposited on the sample as homogeneous, calculated as the average power divided by the area of the laser spot. Indeed it is well known that for a Gaussian function of the form $A \cdot exp(-\frac{x^2}{2\sigma^2})$, where $A$ is the peak value and $\sigma$ is the standard deviation, its FWHM is equal to $\approx 2.355\sigma$. Therefore, approximating the Gaussian spatial profile with a rectangular one with the same peak value $A$ and with a width equal to the Gaussian FWHM, entails approximating its area $A\sigma\sqrt{2\pi} \simeq A\sigma 2.507$ with a value equal to $A\sigma 2.355$, which differ by just $6\%$. Fig. 3.9 shows the detail of the damage caused with 0.93 MW/cm$^2$ irradiance and 240 s of exposure. The laser spot is drawn in white and the damaged area extends far outside the area actually exposed to the laser, so that the particular spatial profile of the laser spot on the sample does not play a significant role, making legitimate to apply the approximation described above.

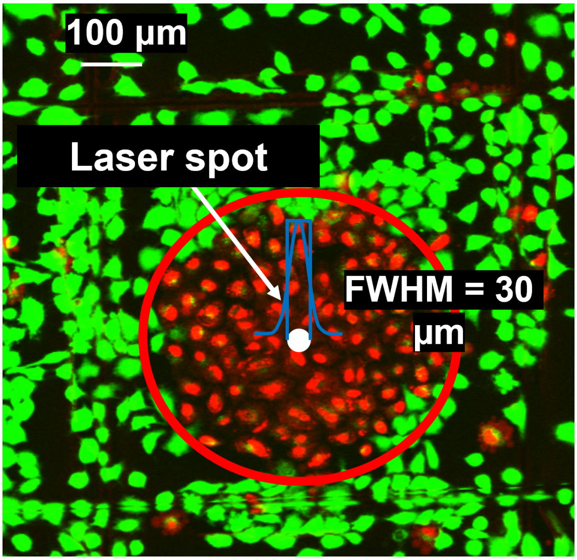

**Figure 3.9:** *Detail of the damage caused with 0.93 MW/cm$^2$ irradiance and 240 s of exposure, highlighted by the red circle. The laser spot, kept fixed on the sample, is represented by the white spot and constitutes the actual irradiated area. The Gaussian profile of the pulse and its rectangular approximation are sketched in blue. Adapted with permission from [167] ®Optica Publishing Group.*

In order to characterize the response of the cells to laser radiation, we carried out a standard viability essay, already described in Subsection 'Cell staining', to assess cells' capacity to survive to laser radiation. Note that the viability test is the least sensitive protocol for detecting cellular phototoxicity. Cell death is just the ultimate effect that radiation could induce on cells. With this test we have no information about non-lethal damage that may occur and undermine cell function or about damage that might trigger the process of apoptosis and lead to delayed death. As can be seen from Fig. 3.8b, no lethal damage is observed for low values of irradiance and/or short exposure times, which corresponds to the area in the top left corner. On the contrary, the damaged areas are present in the lower right area, which corresponds to the area exposed to higher irradiance values for longer exposure times. The radius of the damaged areas also varies in line with irradiance and exposure values and can expand far beyond the area actually exposed to the laser (only 30 $\mu$m of laser spot diameter). In order to obtain statistically relevant results and validate the reproducibility of the experiment, we used 13 different Petri dishes, for a total of 313 irradiated sample points, corresponding to several thousands of cells [167].

A first summary presentation of the average results is given in Fig. 3.10. Here we divided the laser's irradiance values into four groups of same width of 0.2 MW/cm$^2$ and we reported the average cell damage radius observed. Consistently with what already pointed out in Fig. 3.8b, there is a sort of 'safe' zone, represented in green where no damage has ever been caused by using low irradiance values and short exposure time. As irradiance and exposure values increase, the extent of the damaged area increases, up to a radius of hundreds of microns. According to this findings, we decided to approach the analysis in three steps. First, we analysed the data to determine the threshold at which damage occurs, and treated the problem as dichotomous. Second, considering only the points where damage occurred, we correlated its spatial extent with the parameters irradiance and exposure time. Eventually, we correlated the damage with the increase in temperature induced by laser exposure, based on thermodynamic considerations.

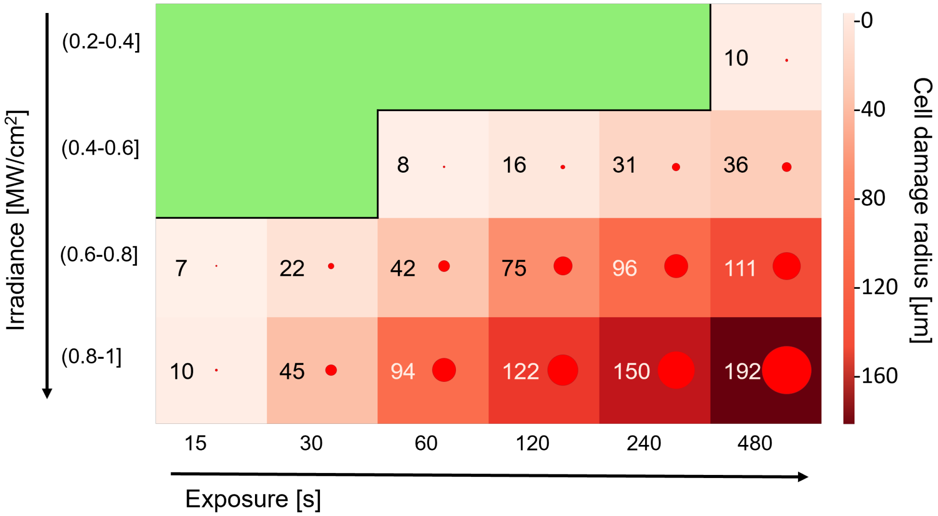

**Figure 3.10:** *For various irradiance ranges and exposure durations, the average radius of the damaged region is shown. The green zone denotes the safe undamaged area. The red circles, the radius of which is indicated by their numerical values, illustrate the spatial extension of the damage. Adapted with permission from [167] ®Optica Publishing Group.*

### 3.3.1 Data analysis

The problem was divided into two phases of analysis: a first more general phase to identify a data-driven model that can define the damage probability (further on in this thesis 'Damage probability: a binary problem') and a next step to analyze and describe the extension of the damaged area on the effectively damaged samples (further on in this thesis 'Extension of the damage: a continuous problem').
For both problems the following hypotheses were considered:

1. the experimental setup is fixed
    - Pulse length ($\tau$) = 130 fs
    - Spot area = $\pi 15^2\ \mu m^2$
    - Repetition rate ($f$) = 80 MHz

    therefore the results have to be considered valid only under the conditions defined above;
2. all measurements are independent of each other.

Finally, the problem was addressed from a thermodynamic point of view, considering the heat generated by the laser and its diffusion in the sample.

### Damage probability: a binary problem

First, we decided to start estimating the probability of damage occurring as a function of the parameters that we varied during the experiment, irradiance and exposure time. To do this, we formulated the problem that we are addressing as a binary problem, defining a dichotomous variable Y. Let Y be the dichotomous variable denoting whether or not damage occurred on the laser-irradiated specimen. Then Y will be equal to 1 if the radius of the damaged area observed on the sample is greater than zero, instead Y will be equal to 0 when no damage has been observed, that the damaged area has radius zero.

$$\text{Y=1} \qquad \text{if} \qquad R_{damage} > 0$$

$$\text{Y=0} \qquad \text{otherwise}$$

In this analysis, we considered 301 experimental points out of 313, after removing outliers and we used a logistic model [7]. The logistic function is a common S-shaped curve, also called sigmoid curve, increasing in a monotonous fashion from zero to 1. It is widely used in statistics, as a distribution function, and in many other fields, including biology. Applying the logistic model, we calculated the probability that the variable Y acquires value 1, *i.e.* that the damage occurs, in this way:

$$Pr(Y = 1) = \frac{1}{(1 + e^{-\beta(x-\mu)})} \tag{3.1}$$

where $\beta$ is defined as the logistic growth rate, it is the steepness of the curve and is inversely proportional to the standard deviation of the dataset distribution. The parameter $\mu$ is the mean, that is the position of the sigmoid's midpoint, i.e. the value of the variable x for which the probability for the damage to occur is 50$\%$. Last but not least, x is the independent variable and we defined it as a function of the exposure time $T_{exp}$ with exponent $k_0$ and the irradiance $I_{avg}$ with the exponent $k_1$ as follows:

$$x = T_{exp}^{k_0} \cdot I_{avg}^{k_1} \tag{3.2}$$

The ordinary least squares (OLS) method is used in the implementation to determine the optimal values for the exponents $k_0$ and $k_1$, as well as the logistic growth rate $\beta$ and the mean $\mu$. We fitted, iteratively on different combinations of values of $k_0$ and $k_1$ varying from -10 to +10 in increments of 0.1, a logistic model that intercepts the dependence between the dependent variable Y and the quantity $x = T_{exp}^{k_0} \cdot I_{avg}^{k_1}$, in order to maximize the accuracy of the prediction.

It is possible to think about logistic regression as a supervised learning approach that belongs to the family of classification algorithms: in order to categorize a prediction's outcome into the class it belongs to (damage/non-damage), the estimated probability may be utilized directly as follows:

damage if $Pr(Y = 1) >= 50\%$

no damage if $Pr(Y = 1) < 50\%$

in which we considered 50% as the cut-off probability. As shown in Table 3.2, the optimal values found was $k_0$=0.5, $k_1$=1.8, $\mu$=4.48 and $\beta$=0.98. The graphic representation of the results of the fitting is given in Fig. 3.11. In these plots, we decided to provide the regression lines, which depict the regression equation connected to the response variable represented as the probability of the damage to occur, as well as the experimental points. Despite the fact that both panels (Fig. 3.11a and Fig. 3.11b) depict the same graph, Fig. 3.11b depicts each curve as representing a separate exposure time value, which makes it easier to understand and analyze the data. To assess the ability of our algorithm to correctly classify and predict damaged and undamaged experimental points, we plotted them in Fig. 3.11 using two different symbols, a circle and a cross respectively. In addition, we shaded the upper semi-space of the backdrop of Fig. 3.11 gray to indicate where damage is more likely to occur, i.e. where $Pr(Y = 1) >= 50\%$. Considering the model that we have implemented, the specificity, that is the ability to correctly classify the undamaged points, is very high and stands around 95%, while the sensitivity, that is the ability to correctly classify the damaged points, stands around 75%. Overall a good result that could be deduced directly from the graph, in fact most of the circles (damaged experimental points) are present in the upper part of the graph and most of the crosses (non-damaged experimental points) in the lower part. The results are summarized in Table 3.2.

| **Coefficients** | **Exponents** | **Accuracy** | **Specificity** | **Sensitivity** |
|---|---|---|---|---|
| $\mu$ = 4.48<br>$\beta$ = 0.98 | $k_0$ = 0.5<br>$k_1$ = 1.8 | 85.1% | 94.8% | 74.8% |

**Table 3.2:** *Optimal values obtained for coefficients $\beta$ and $\mu$ and exponents $k_0$ and $k_1$, and accuracy, specificity and sensitivity of the model implemented.*

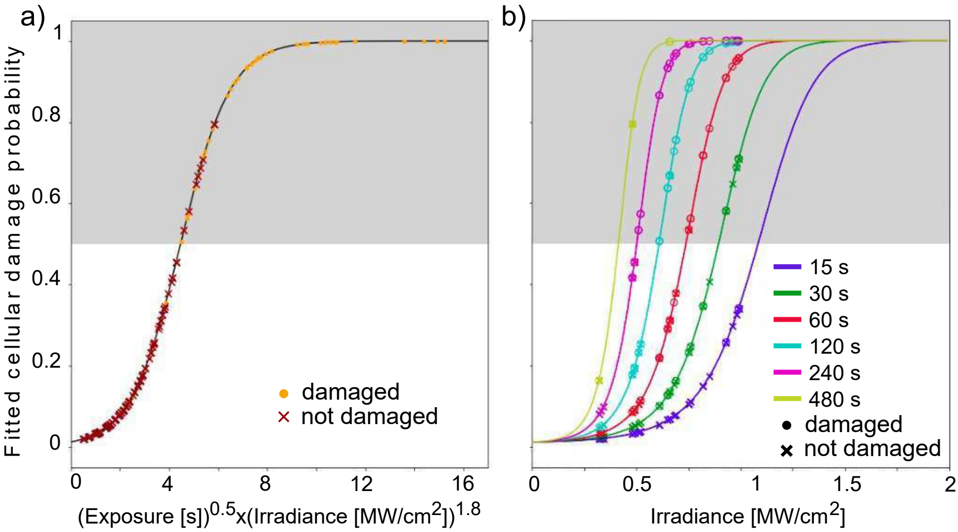

**Figure 3.11:** *a) The damage probability curve for sample points irradiated by a fixed laser as a function of the applied irradiance and exposure time. b) The damage probability curve for sample points irradiated by a fixed laser as a function of the applied irradiance for different exposure times. Reprinted with permission from [167] ®Optica Publishing Group.*

It is crucial to proceed in the least impactful and invasive way possible when approaching live cell imaging. We have used our results to develop a rule for those approaching to use nonlinear optical microscopy on vital Hela cells with ultrashort pulsed laser sources of duration 100$\sim$200 fs, with high repetition rate in the range 40$\sim$100 MHz and wavelength in the near-infrared spectral region, that means $\lambda \approx 1$ $\mu$m. To do this, we have assumed as an acceptable safety threshold, to limit the probability of damage to the sample to less than 5%. Choosing this value as the desired value for the dependent variable Y in the Eq. (3.1), we calculated the corresponding value for the independent variable x, that is x=1.475. At this point, using the definition we have chosen for the variable x, given in Eq. (3.2), we have calculated some safe working conditions, which are shown in the Table 3.3. As far as the experiments were concerned, no damage was seen in any of the samples exposed to x<=1.475, indicating that the safety limit was chosen appropriately.

*Safe working conditions*

| Exposure time T$_{exp}$ | Maximum Irradiance I$_{avg}$ |
|---|---|
| 1 second | 1.241 MW/cm$^2$ |
| 10 seconds | 0.655 MW/cm$^2$ |
| 1 minute | 0.398 MW/cm$^2$ |
| 10 minutes | 0.210 MW/cm$^2$ |

**Table 3.3:** *Safe working conditions required to maintain the damage risk below 5% in fixed laser beam studies and throughout our parameter range.*

### Extension of the damage: a continuous problem

In this section, the key variable we analyzed is the spatial extension of the damage. So we decided to study the relationship between the extent of the damaged area, assumed circular and represented by its radius R, and the parameters that we varied during laser exposure, namely exposure time T$_{exp}$ and irradiance I$_{avg}$. To find the empirical formula that represented this relationship, we used a dataset consisting of 155 experimental points. In fact, from the initial 313, we removed the outliers and all the experimental points where the damage was not observed, so with R=0, and we kept only the points where the damaged area has extension greater than zero, so R>0. In this analysis, let R be the variable that describes the extension, in terms of $\mu$m, of the damage on the sample irradiated by the laser kept fixed. We modeled R with a regression model built on the exposure time T$_{exp}$ and on the irradiance I$_{avg}$, in this form:

$$R = \nu \cdot T_{exp}^{h_0} \cdot I_{avg}^{h_1} \qquad \nu, h_0, h_1 \in \mathbb{R} \tag{3.3}$$

The model determines how the extent of the damage behaves, identifying the optimal values for the exponents $h_0$ and $h_1 \in \mathbb{R}$ together with the coefficient $\nu$ using the OLS method. So, we fitted iteratively on different combinations of values of $h_0$ and $h_1$ (varying in the range from -10 to +10 with increments of 0.1) a regression model that intercepts the dependence between the dependent variable R and the quantity $T_{exp}^{h_0} \cdot I_{avg}^{h_1}$, maximizing the R$^2$ value. The results are reported in Table 3.4. The highest accuracy of the prediction was achieved for the exponent values $h_0$=0.3 and $h_1$=1.5, which were quite similar to the values obtained in the preceding section ($k_0$=0.5 and $k_1$=1.8).

A graphical representation of the model is shown in Fig. 3.12. The circles represent the mean values of the radius of the damaged area observed on the sample, called cellular damage radius, with their standard deviation,

| Coefficient | Exponents | $R^2$ |
|---|---|---|
| $\nu = 32.11$ | $h_0 = 0.3$<br>$h_1 = 1.5$ | 0.947 |

**Table 3.4:** *Optimal coefficient $\nu$ and exponents $h_0$ and $h_1$ values calculated to maximize the coefficient of determination $R^2$.*

reported as error bar, and are plotted as a function of the irradiance for the different exposure times. The cellular damage radius increases slightly with the prolongation of the exposure time $T_{exp}$, instead the trend is nonlinear with the augmentation of the irradiance $I_{avg}$, as confirmed by the exponent $h_1$ that is greater than 1.

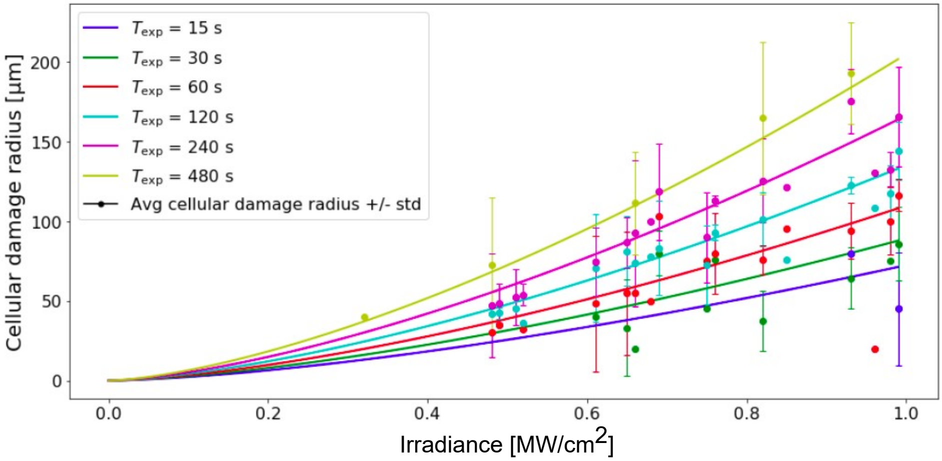

**Figure 3.12:** *Graphical illustration of the curves demonstrating the size of the cellular damage radius as a function of applied irradiance in sample locations exposed to a fixed laser for six different exposure times. Reprinted with permission from [167] ®Optica Publishing Group.*

### Spread of the damage in the sample: a thermodynamic approach

At this point, we decided to investigate the source and the characteristics of the damage itself. We noticed that the damaged areas in the samples were often much larger that the area that was actually irradiated by the laser, especially for long exposure times. This behaviour is perfectly visible in Fig. 3.9, suggesting that the damage is somehow spreading, resulting in the death of cells that have never been directly exposed to the laser radiation. Our hypothesis to interpret this phenomenon was the generation of photo-induced heat and its diffusion in the sample. For this reason, in this section we decided to analyze our data following a thermodynamic approach and considering the photothermal phenomena that can occur when laser radiation interacts with matter.

Photothermal interaction occurs in situations where the temperature increase in the medium is the main effect of the laser irradiation. When cells reach temperatures of roughly 42°C, they are subjected to thermal damage [169]. Cell death or changed cell behavior, such as reduced cell reproduction, may occur when temperatures reach dangerously high levels [152]. In some circumstances, photothermal damage produces immediately visible negative effects, ranging from coagulation and vaporisation to direct melting or carbonization of the object exposed to radiation. When investigating photothermal damage, there are two basic processes to take into consideration: *heat production* and *heat transfer* [123]. In our case, the *heat generation* occurs when the sample is illuminated and is caused by the deposition of laser energy in the sample. The amount of energy deposited depends both on the laser parameters, such as wavelength, temporal pulse length and repetition rate, and on the optical properties of the sample. If scattering and reflection are neglected, the optical properties are reduced to the absorption coefficient $\alpha$. Absorption is governed by Lambert-Beer's law, which, for a Gaussian beam propagating in the $z$-direction within a medium, can be written as:

$$I(r,z,t) = I_0(t)e^{-r^2/2\sigma^2}e^{-\alpha z}, \tag{3.4}$$

in terms of laser intensity $I(r,z,t)$, where $z$, as already mentioned, is the propagation direction and also the vertical coordinate of our reference system, $\sigma$ represents the standard deviation of the Gaussian-like profile of the beam in the horizontal plane, with radial coordinate $r$, and $\alpha$ is the absorption coefficient of the medium through which the laser beam propagates. To correctly apply Eq. (3.4) to our experiment, the parameter $\sigma$ should be set to 30 $\mu$m, corresponding to the FWHM of the beam in the focal plane, while the absorption coefficient has been set a value $\alpha \sim$ 0.2 cm$^{-1}$ [157], namely the absorption coefficient of the DMEM at the wavelength of our laser source ($\lambda$=1040 nm). Finally, considering the intensity temporal profile $I_0(t)$, despite the fact that the study was conducted using a pulsed laser source, the high laser repetition rate ($f_{rep}$=80 MHz) enables one to consider it as if it was a continuous source. In order to be consistent with the lexicon usually adopted in photometry, in this thesis we referred to the average intensity of the laser $I_0$ using the term irradiance $I_{avg}$, calculated as:

$$I_0 = I_{avg} = \frac{P_{avg}}{A_p}, \tag{3.5}$$

where $A_p$ is the beam spot area on the sample, considering its value at FWHM, and $P_{avg}$ is the average laser power, calculated as:

$$P_{avg} = f_{rep} E_p, \tag{3.6}$$

with $E_p$ the single pulse energy. After the laser radiation has been absorbed by the medium, the heat begins to diffuse in the sample. The crucial point to correctly simulate this phenomenon, is to model a heat source that can cause an increase in temperatures in the medium exposed to the laser. It is possible to express the heat source considering its volume density $Q(r, z)$, which is calculated, using the Lambert-Beer's law, as the derivative in the $z$-direction of the intensity profile $I(r, z, t)$, namely:

$$Q(r, z) = \alpha I_0 T_w e^{-r^2/2\sigma^2} e^{-\alpha z} g(z). \tag{3.7}$$

The notation is the same used above. Here we consider two additional terms: the first one is the Fresnel transmission factor $T_w$, inserted to account for the effect of the passage of the laser beam through the air/DMEM interface; the second one is the term $g(z)$ and it has been introduced to consider the transverse spreading of the beam caused by diffraction and it is coherent with the confinement of the beam during propagation.

At this point, to understand how the heat diffuses in the sample, we must study the related thermal transport problem. We considered the Fourier transport equation and we solved it for the temperature field $T(r, z)$:

$$\rho C_p \frac{\partial T(r, z)}{\partial t} - \kappa \nabla^2 T(r, z) = Q(r, z), \tag{3.8}$$

with $\rho$ the density, $C_p$ is the heat capacity and $\kappa$ is the thermal conductivity of the medium in which the heat is spreading. The term $Q(r, z)$ represents the heat source mentioned above. The calculations were carried out using a finite-element method (FEM)-based model, which was implemented using a commercial software (COMSOL Multiphysics 5.6). Table 3.5 lists the thermal parameter values used in the simulation, as reported in literature [83, 129, 157, 173].

Thanks to the symmetry of the sample and laser beam, we solved the heat transfer equation considering a two-dimensional axisymmetric domain of 500 $\mu$m × 500 $\mu$m. To correctly replicate the experimental circumstances, the system was examined by establishing Infinite Element (IE) domains that encircle the physical domain, simulating an indefinitely extended aqueous environment that is several times bigger than the cell area in the sample. Outside IEs, the temperature was held constant at 27°C, *Cell culture medium (DMEM)*

| Parameter | Value |
|---|---|
| **Specific heat capacity** ($C_p$) | 4186 (Jkg$^{-1}$K$^{-1}$) |
| **Density** ($\rho$) | 1000 (kgm$^{-3}$) |
| **Thermal conductivity** ($\kappa$) | 0.6 (Wm$^{-1}$K$^{-1}$) |
| **Absorption coefficient** ($\alpha$) | 0.2 (cm$^{-1}$) |

**Table 3.5:** *DMEM's optical and thermal parameters used in the simulation [83, 129, 157, 173].*

which was the equilibrium initial value ($T_0$).

The results obtained from the solution of the Eq. (3.8) are shown in Fig. 3.13. In panel (a) we reported the temperature reached at the center of the laser spot ($r$ = 0, $z$ = 0) over time, for three different values of irradiance: 0.57 MW/cm$^2$, 0.71 MW/cm$^2$ and 0.85 MW/cm$^2$. The most obvious thing that can be seen from this graph is that the temperature reaches saturation in $\simeq$ 500 ms, a much shorter time than the values we used as exposure times. Once this equilibrium value is reached, it is kept constant for the rest of the laser exposure and the temperature at the center of the laser spot is purely the outcome of a dynamic equilibrium between the heat generation induced by laser absorption and the heat diffusion in the sample in the presence of the laser. In fact, it is directly proportional to the irradiance as displayed in panel (b) of Fig. 3.13. Finally, we studied how the temperature evolves spatially in the sample and in the panel (c) of Fig. 3.13, we reported the profile of the equilibrium temperature (after two seconds of exposure) along the radial coordinate $r$, up to a maximum value of 250 $\mu$m, again for three different values of irradiance: 0.57 MW/cm$^2$, 0.71 MW/cm$^2$ and 0.85 MW/cm$^2$. Indeed, we found that the temperature saturated also outside the laser spot but it took a longer time, in the order of few seconds.

The next step in our study was comparing this theoretical model to the experimental data on the extension of the damage. As already mentioned, we approximated the damaged areas obtained experimentally to circular areas, whose extension we measured by referring to the cellular damage radius R. Using the results obtained in the simulation, we have obtained the temperature reached along the perimeter circumference of each damaged area, that is, corresponding to the distance from the center of the laser spot equal to the cellular damage radius R. Our goal was to find the temperatures that had proven lethal and caused cell death. An illustration of this process is shown in Fig. 3.14. Six experimental points illuminated with an irradiance of 0.82 MW/cm$^2$ are shown in the top row. Each of these points was

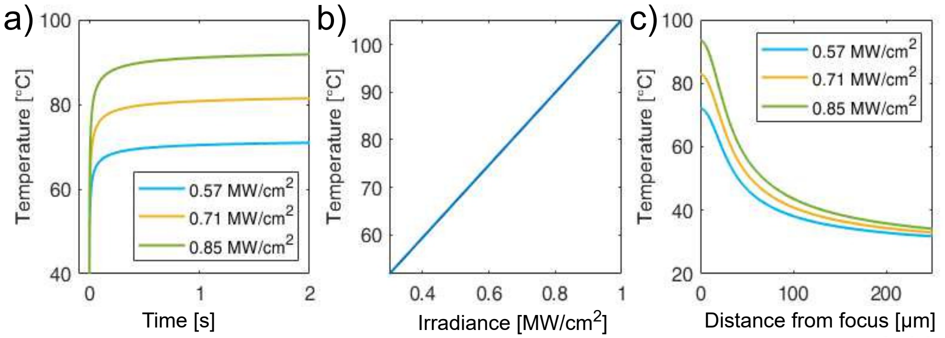

**Figure 3.13:** *a) Temperature reached on the sample as a function of time at the center of the laser focal spot ($r = 0, z = 0$), calculated with Eq. (3.8), for 3 different values of irradiance. b) Temperature reached on the sample as a function of irradiance at the center of the laser focal spot, calculated using Eq. (3.8). c) Temperature profile in the Petri dish as a function of the radial coordinates for three different values of irradiance. Reprinted with permission from [167] ®Optica Publishing Group.*

exposed to the laser for a different exposure time, that goes from 15 s to 480 s. As already said, green cells are healthy and vital cells, whereas red cells are dead. For this value of irradiance, an exposure of 15 s does not cause any damage, for longer exposure times the damage appears and its extension increases with increasing exposure time. The edge of the damaged area is highlighted by the yellow circle and the cellular damage radius $R$ is its radius. Plots of temperature spatial distributions in the sample obtained from simulations, for the same irradiance value, are reported in the bottom row. On each plot, the isotherm corresponding to the edge of the damaged region was colored green based on the experimental images. The values of the isotherms highlighted in green are shown below, while the temperature reached at the center of the laser spot is 91°C.

Looking at Fig. 3.14, we noticed that the temperatures that induce cell death for short exposure times are much higher than those that have the same effect for long exposure times. In fact, after 30 s of illumination only cells approaching 50°C die, whereas for an exposure of 480 s a little less than 40°C is sufficient to induced permanent damage. The same behaviour was found for all samples and irradiance values tested. Interestingly, we realized that the cellular damage radius, that we expressed as function of exposure time $T_{exp}$ and irradiance $I_{avg}$ in Eq. (3.3), for a particular exposure time is solely dependent on the sample's local temperature, due to the linear relationship between irradiance and temperature shown above. To confirm this, we determined the temperature reached at the edge of the

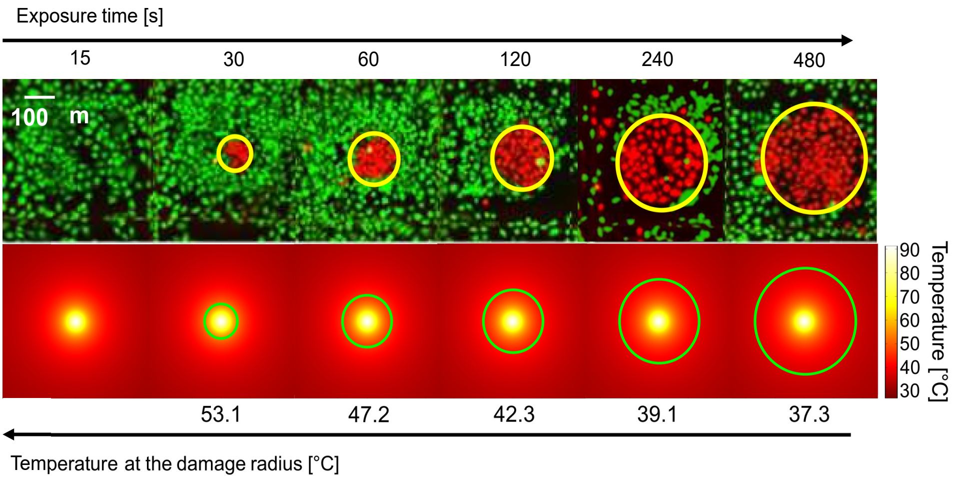

**Figure 3.14:** *Effect of increasing exposure time on cells. In the first row, the experimental damage obtained using an irradiance of 0.82 MW/$cm^2$ and varying exposure time, with the circumferences of the damaged areas highlighted in yellow. In the second row, simulations where the isotherms and relative temperatures, corresponding to the circumferences of the damaged areas, are highlighted in green. Reprinted with permission from [167] ®Optica Publishing Group.*

damaged area for all the 155 samples, in the same way as for Fig. 3.14. The result is presented in Fig. 3.15. Here the blue dots are the temperatures corresponding to each cellular damage radius $R$ observed experimentally, for all irradiance values, divided according to the exposure time. As shown in the graph, for a given exposure time, the cellular damage radius, that is the radius that describes the extent of the area of dead cells, will always correspond to the same threshold temperature. To emphasize this result, a red vertical line was added to Fig. 3.15 to represent the mean threshold temperature.

To further confirm the validity of our approach and our results in temperature increase, we compared our results with those obtained by employing a formula proposed by Macias-Romero *et al.* [104]. This model calculates the temperature increase in the sample due to the interaction with a pulsed focused Gaussian beam with repetition rate $f$ and pulse duration $\tau$:

$$\Delta T(x,y,z,t) = \sum_{n=0}^{int(t*f)} \int_0^{\tau_p} \frac{A\sqrt{2}}{8\pi^2 C_p[\kappa(t-t'-\frac{n}{f})]^{3/2}} \iiint_{-\infty}^{\infty} e^{-\frac{2(x'^2+y'^2)}{a^2}-\frac{2z'^2}{b^2}-\frac{(x-x')^2+(y-y')^2+(z-z')^2}{4\kappa(t-t'-\frac{n}{f})}} dx'dy'dz'dt' \tag{3.9}$$

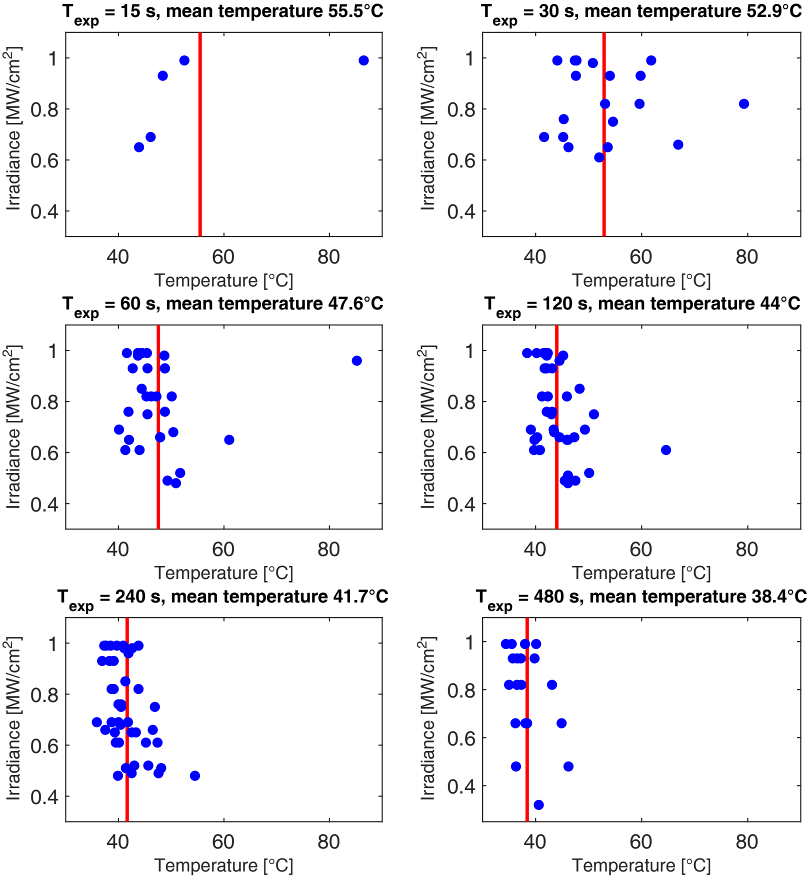

**Figure 3.15:** *For each sample and irradiance, scatter plots of the temperatures at the border of the cellular damage areas, divided by exposure time, are shown. Each group's mean threshold temperature is displayed in red. Reprinted with permission from [167] ®Optica Publishing Group.*

The parameters appearing in the formula are: $a$ and $b$, which are the semi-axes of the transverse and longitudinal dimensions of the heat source, respectively in the radial plane and in the $z$-direction; A is a constant given by $A = 2\alpha bE/(\pi a^2 b)$, where $\alpha$ is the absorption coefficient and $E$ is the energy delivered by a single pulse; $\kappa$ is the thermal conductivity of the medium and $C_p$ is the specific heat capacity of the medium, expressed in units of $Jg^{-1}K^{-1}$. In Table 3.6, a comparison of temperature increase values obtained at the centre of the laser spot after 1 second of laser exposure

| Average laser power | Temperature rise | |
|---|---|---|
| | Fourier-based model | Macias-Romero model |
| 1 W | 10.7°C | 11.8°C |
| 3.5 W | 39.3°C | 41.3°C |
| 7 W | 76.5°C | 82.5°C |

**Table 3.6:** *Temperature increase in the sample at the center of the laser spot for 1 s of exposure time, calculated with the Fourier-based model and with the model proposed by Macias-Romero and colleagues, for three different values of average laser power.*

with the Fourier-based model (second column) and with Macias-Romero model (third column) is reported. The results are very close, with a discrepancy in the range 1-7 degrees, which is probably better than the achievable precision in measuring the local temperature rise in cells using a thermocamera or a temperature sensitive dye.

## 3.4 Cell response to scanning laser exposure

In this section we present the second experiment we conducted to study the cellular response to laser exposure in terms of cell viability, but this time we applied a laser scanning illumination modality (Fig. 3.16). Some laser power and irradiance values have already been proposed to avoid damaging the samples under observation [44, 53]. Our purpose in this work is to explore a new range of parameters to broaden the knowledge of this complex phenomenon.

Before presenting the methodology and results of this experiment, a short clarification on our scanning system is needed. In this illumination configuration, the laser describes a serpentine pattern on the sample, thanks to the combined use of the galvanometric mirror and the motorized translational stage, as already described in 'Scanning system' Subsection. Throughout the experiment, the laser beam scans a defined area of the sample of dimension 50×50 $\mu$m$^2$. So the beam follows a serpentine pattern to cover the whole area, changing direction after each horizontal scan is completed. The vertical distance between two consecutive horizontal scans is inversely proportional to the number of equispaced horizontal lines scanned used during the illumination. We used the number of equispaced horizontal lines as a parameter of the experiment, calling it number of lines $L$. For this parameter we explored three different values: 20, 50 and 200 lines. Given the scanning laser beam diameter dimension ($d = 12$ $\mu$m), the vertical dimension of the scanned area (50 $\mu$m) and the number of lines ($L$) used in the experiment, it is clear that the scanning lines overlay during illumination procedure, as depicted in Fig. 3.17. To clarify this aspect, we defined the vertical line density (VLD) as:

$$VLD = d \cdot (\frac{L}{50\mu m}) \tag{3.10}$$

Another useful parameter when dealing with this kind of topics is the energy density, also called light dose $D$. This parameter is defined as:

$$D = I_{avg} \cdot T_{exp}, \tag{3.11}$$

with $I_{avg}$ irradiance and $T_{exp}$ the exposure times. When calculating exposure duration in this experiment, we took into account the entire amount of time that a single cell was illuminated by laser light, which we estimated as follows:

$$T_{exp} = \frac{A_{spot} \cdot (\frac{L}{50\mu m})}{V_s}, \tag{3.12}$$

with $A_{spot}$ the area of the laser spot on the sample and $V_s$ the scanning speed.

In this configuration we studied cell viability as a function of average laser power $P_{avg}$, scanning speed $V_s$ and number of lines $L$. In particular, we systematically varied the average laser power between 1 W and 7 W, for the scanning speed we studied 3 different values, 0.25 mm/s, 0.5 mm/s and 1 mm/s, and we tested three different values of number of scanning lines, 20, 50 and 200, as already mentioned. The complete list of parameters used in this experiment, both fixed and variable ones, can be seen in Table 3.7.

We performed this experiment on three different samples. On each sample we irradiated 54 areas of 50×50 $\mu$m$^2$ each. Each area was exposed with a different combination of the three parameters under analysis: average laser power, scanning speed and number of lines. There were an average of 10 cells in each 50×50 $\mu$m$^2$ area and, using three distinct samples, we were able to acquire consistent findings across more than 1600 cells. Even if in some cases the damage spreads beyond the region where the laser irradiated, we decided to only count cells in that area.

This time we decided to monitor the cell viability over a longer period after laser exposure, to also consider photo-induced cell apoptosis that was not immediately visible and to get more accurate results. Thus, to analyze the effects of laser radiation on cell viability after irradiation, two images of each samples were acquired at the confocal microscope (as described in Subsection 'Confocal microscopy'), one immediately after exposure and

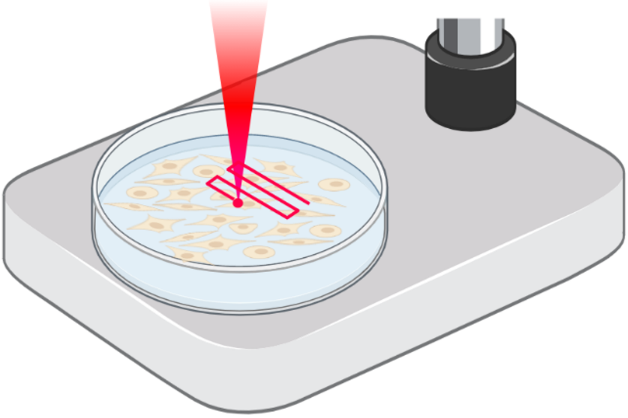

**Figure 3.16:** *Schematic representation of the scanning laser illumination configuration. The laser describe a serpentine pattern on the sample.*

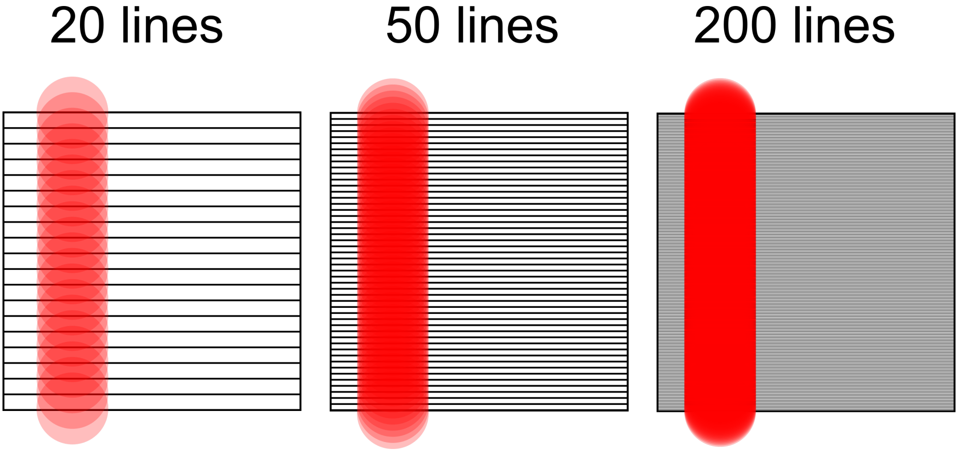

**Figure 3.17:** *Graphic representation of the vertical line density parameter (VLD). The squares represent the scanned surfaces, with a number of lines (L) equal to 20, 50 and 200 lines. The red circle represents the laser spot.*

one after 18 hours. During the counting process, we divided cells in three categories: *live*, *dead* and *stressed*. *Live* cells display a bright green color and have an elongated shape indicating that they are still safely attached to the substrate. *Dead* cells are red in color and usually have circular shape, because they have detached from the bottom of the Petri dish. They also appear smaller than healthy cells. Some of the cells couldn't be clearly put in one of these two categories. We classified those cells as *stressed*, including cells that have both green and red areas and cells that are still green

*Experimental parameters*

| **Parameter** | **Value** |
|---|---|
| **Average Laser power - $P_{avg}$** | [1 - 7] W |
| **Number of lines - L** | 20, 50, 200 |
| **Scanning speed - $V_s$** | [0.25, 0.50, 1] mm/s |
| **Irradiance - $I_{avg}$** | [0.9 - 6.2] MW/cm$^2$ |
| **Energy per pulse - $E_p$** | [12.5 - 87.5] nJ |
| **Peak power - $P_p$** | [96 - 673] kW |
| **Energy density - D** | [0.04 - 11.2] MJ/cm$^2$ |
| **Spot radius** | 6 $\mu$m |
| **Pulse length - $\tau$** | 130 fs |
| **Repetition rate - f** | 80 MHz |
| **Wavelength - $\lambda$** | 1040 nm |

**Table 3.7:** *Experimental parameters used in scanning laser illumination experiment.*

but seem to have an unhealthy shape. Cells belonging to this category are possibly apoptotic cells, and the 18-hours timelapse helped us observe thier behaviour over time. Examples of the three categories can be seen in Fig. 3.18.

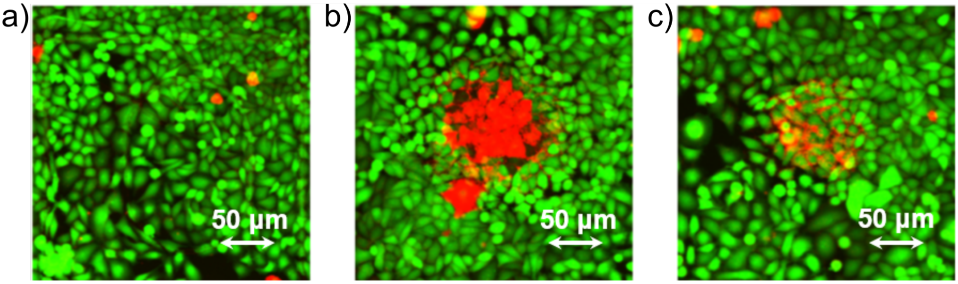

**Figure 3.18:** *Examples of different types of cells stained with ethidium homodimer-1 and calcein-AM. a) Healthy live cells. b) Cluster of dead cells. c) Cluster of stressed cells.*

Fig. 3.19a shows the image obtained with the confocal microscope of a sample 18 hours after it has been exposed to the laser, instead Fig. 3.19b reports the same image with the 54 irradiated areas highlighted by the white squares.

### 3.4.1 Data analysis

The objective of this study is to develop a data-driven law that explains how the experimental, *i.e.* variables average laser power $P_{avg}$, scanning speed $V_s$

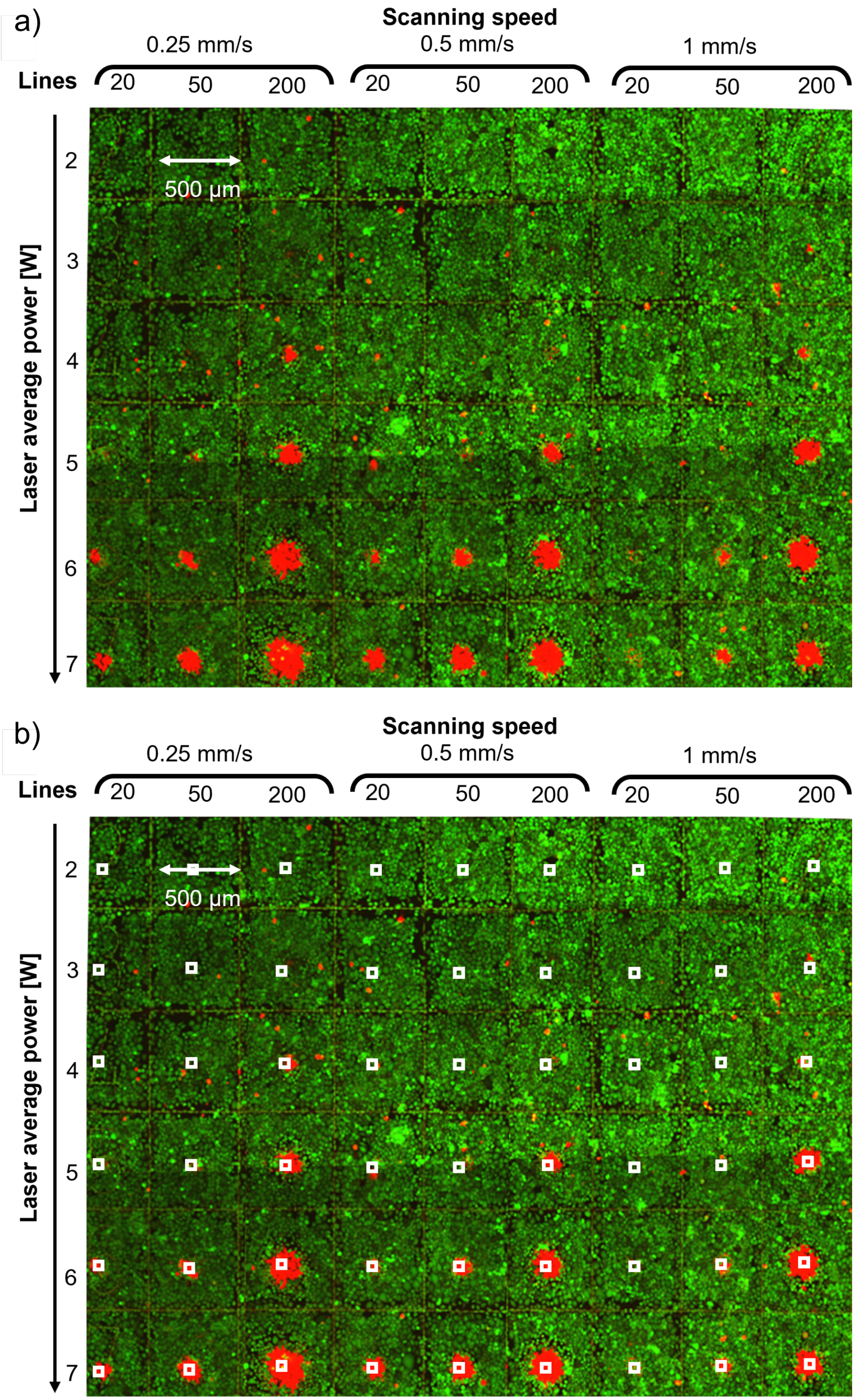

**Figure 3.19:** *Image, obtained using a confocal microscope, of a sample after laser exposure. a) Thanks to the use of fluorescent dyes, alive cells are stained in green and dead cells are stained red, it is possible to see the lethality of the radiation varying the values of average laser power, scanning speed and number of lines. b) Same image reported in panel a with the irradiated areas highlighted by the white squares. Adapted with*

and number of lines $L$, are related to the percentage of damaged cells, that means dead and stressed cells. Let Y be the percentage of damaged cells (dead and stressed) after laser exposure in the scanned area. In the same way we did in the previous experiment, we decided to use a logistic function to model the variable Y (see Eq. (3.1)), but this time the independent variable x is defined as:

$$x = P_{avg}^{k_0} \cdot L^{k_1} \cdot V_s^{k_2}, \tag{3.13}$$

therefore, as a function of the experimental variables elevated to the exponents $k_0$, $k_1$ and $k_2$.

In this analysis we considered 187 experimental data and, same as before, we used the OLS method to determine the optimal values for the exponents $k_0$, $k_1$ and $k_2$, fitting iteratively on different combinations of values in the range -10 to +10 in increments of 0.1. The optimal values, which maximize the R$^2$ of the interpolation, obtained for the exponents are $k_0$=1.0, $k_1$=0.16 and $k_2$=-0.08, with a coefficient $\mu$=8.65 ± 0.12, a coefficient $\beta$=0.90 ± 0.12. These results are summarized in Table 3.8.

| $k_0$ | $k_1$ | $k_2$ | $\mu$ | $\beta$ | $R^2$ |
|---|---|---|---|---|---|
| 1.0 | 0.16 | -0.08 | 8.65 ± 0.12 | 0.90 ± 0.12 | 0.79 |

**Table 3.8:** *Optimal values of the exponents $k_0, k_1, k_2$ and of the coefficients $\mu$ and $\beta$, that maximize the R$^2$ value of the model implemented.*

The graphic representation of the results of the fitting is given in Fig. 3.20. In panel a, we reported the fitted logistic function (solid line) obtained with data (dots) collected 18 hours after illumination. In order to demonstrate the need to assess photodamage even many hours after exposure, we have also included in the graph in red the result obtained with the data collected immediately after exposure to laser radiation. In fact, using the data collected after 18 hours, the resulting curve (black curve) is left-shifted from the curve obtained with the data collected immediately after laser exposure (red curve). This means that the number of damaged cells has increased in the 18 hours between the two data acquisitions, and therefore the radiation had induced apoptosis processes not immediately detectable, proving the unreliability of the data collected immediately after irradiation. In panel b of Fig. 3.20 we decided to plot the result obtained 18 hours after illumination by dividing the data according to the number of lines $N$ used in the illumination. In this case we didn't repeat the optimization of the fitting procedure, we just used the optimal values identified before (and reported in Table 3.8) redefining the independent variable x for the plot:

$$x_L = P_{avg}^{k_0} \cdot V_s^{k_2}, \tag{3.14}$$

So we reported three scatter plots and the three interpolations of the same optimal logistic function: in green for $L$ = 20, in yellow for $L$ = 50 and in cyan for $L$ = 200. This graph clearly shows that the higher the number of lines, the more cells are damaged, and this is directly related to the fact that more lines correspond to greater cell illumination during the imaging process. In fact, going to consider the exponent $k_1$ obtained for the number of lines ($L$) variable, the percentage of the damage cells is directly dependent on L, but in a sub-linear way, being $k_1$ = 0.16 (less than 1). Looking at the other variables used in the experiment, as expected we find a very weak inverse dependence on scanning speed $V_s$, with $k_2$ = -0.08, while the most significant dependence we find by the average laser power $P_{avg}$. With $k_0$ = 1.0, the percentage of damage cells depends linearly on the $P_{avg}$. The heatmaps in the Fig. 3.21 represents values assumed by the dependent variable Y = F(x, $\mu$, $\beta$) for any combination of $P_{avg}$, $V_s$ and $L$, providing a graphical representation of the dependencies: when the power of the laser varies (vertical axis), the proportion of damaged cells changes considerably more than when the scanning speed varies (horizontal axis) or the number of lines (the three consecutive heatmaps).

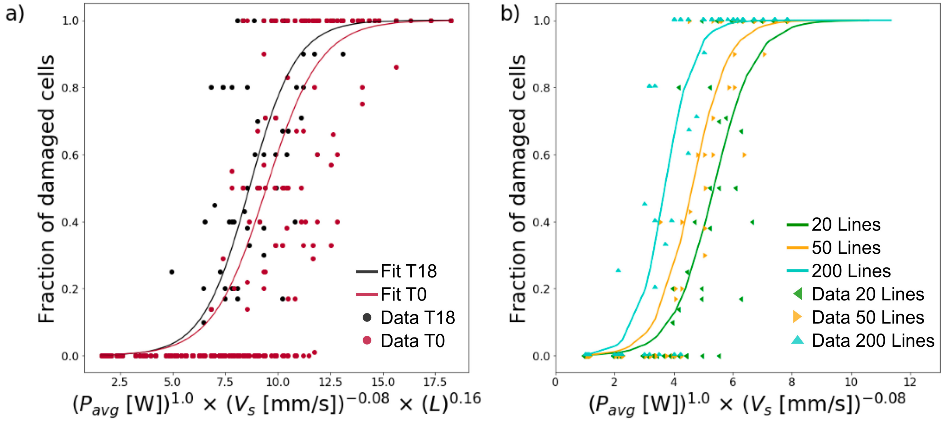

**Figure 3.20:** *a) Logistic fit: in red with data collected just after the laser exposure and in black with data collected after 18 hours. b) Logistic fit for each value of number of lines L, with data collected after 18 hours. Reprinted with permission from [167] ®Optica Publishing Group.*

In the analogous way as for fixed laser illumination configuration, we

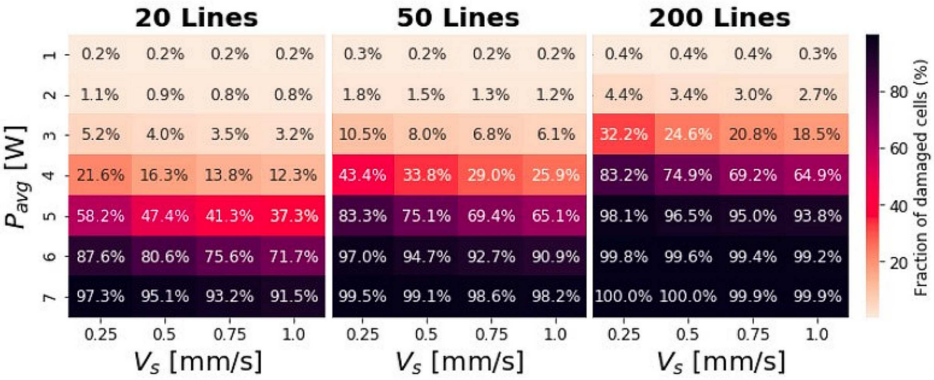

**Figure 3.21:** *Percentage of damaged cells calculated for any combination of $P_{avg}$, $V_s$ and L. Reprinted with permission from [167] ®Optica Publishing Group.*

derived also in this case an empirical safety rule to perform imaging in laser scanning illumination configuration. As before, this rule has been designed to keep the probability of damage below the 5% threshold and is valid in the range of parameters we have explored. According to this rule, the safety limit corresponds to x = 5.367. As confirmation of the validity of this threshold, from our experiment only one experimental point was damaged below this value of the independent variable x. We summarized the safety working conditions in Table 3.9, calculating the safe values of average laser power using Eq. (3.13).

***Safe working conditions***

| **VDL** | **$V_s$ = 0.25 mm/s** | **$V_s$ = 0.5 mm/s** | **$V_s$ = 1 mm/s** |
|---|---|---|---|
| **2.4** | 2.975 W | 3.145 W | 3.324 W |
| **6** | 2.569 W | 2.715 W | 2.870 W |
| **24** | 2.058 W | 2.175 W | 2.299 W |

**Table 3.9:** *Maximum values of average laser power allowed for keeping the damage probability below 5% in scanning laser illumination configuration, valid for our range of parameters.*

## 3.5 Discussion

In this chapter we presented a careful study of the cellular response, in terms of viability, induced in vital HeLa cells exposing them to NIR ultrashort pulsed laser source in two different laser illumination configurations, *i.e.* keeping the laser fixed on the sample or scanning the laser beam over the sample area. It is possible to investigate the mechanism of damage that takes place considering its dependence on the applied laser power. In fact, it is well established the relation between the photodamage rate R and the laser parameters:

$$R \propto P_p^n f \tau, \tag{3.15}$$

with $P_p$ laser peak power, n the order of photodamage mechanism, $f$ laser repetition rate and $\tau$ pulse duration [4, 54, 87]. In the first experiment, conducted in fixed laser illumination configuration, we studied the photodamage as a function of irradiance $I_{avg}$, that we defined as $I_{avg}$ = $P_{avg}$/ spot area [MW/cm$^2$]. For the duration of this first experiment we kept the spot area constant, so we can say without losing generality, that we studied the dependence of damage from the average laser power. In the second experiment, conducted in laser scanning illumination configuration, we investigated the onset of the damage as a function of the average laser power. Because we opted not to modify the repetition rate or pulse length, we decided to study the dependence of damage on average laser power instead of laser peak power, without sacrificing generality, in order to interpret our data and evaluate the damage mechanism that comes into play.

Starting with the results obtained in the first experiment, in Subsubsection 'Damage probability: a binary problem' we obtained for the irradiance an exponent $k_1$ = 1.8, while in Subsubsection 'Extension of the damage: a continuous problem' we obtained an exponent $h_1$ = 1.5. In each of these instances, the exponent is smaller than 2. Interpreting this data, we can say that phototoxicity is mainly caused by a first order process, so the damage is photothermal, with some contribution from second order processes, as indicated by the fact that the exponent is greater than 1. This finding is further corroborated in Subsubsection 'Spread of the damage in the sample: a thermodynamic approach', where it is proved, with thermodynamic considerations, that potentially fatal temperatures are achieved in correlation with damaged sample area. Thus, the presence of photothermal damage is confirmed. Then we deepened the damage induced by higher order processes. Our hypothesis is that the thermal shock induced from the laser exposure enhanced the formation of reactive oxygen species (ROS), as already observed in literature [48, 161]. Furthermore, heat shock has been shown to activate not only ROS production, but also the death receptor apoptotic pathways, resulting in cell death [63, 64, 72]. In fact when cells are under stress, they start to send signals to each other which could trigger the apoptosis process (extrinsic pathways) [46]. In light of this, the death of cells exposed to potentially non-lethal temperatures for very long exposures (the temperature threshold calculated for an exposure time of 480 s is just 38.4°C) would be explained: infrared radiation and the heat generated act as environmental stressors and induce cells to exchange apoptosis signals. A confirmation of this hypothesis can be found considering the theory of Brownian motion, random walk and diffusion. Indeed, thanks to these theories we know that diffusing molecules travel over a distance whose square value increases on average linearly with time [154]. We found in Subsubsection 'Extension of the damage: a continuous problem' that the cellular damage radius is related to exposure time elevated to a power close to 0.5, which supports the idea that apoptotic signals are exchanged and diffused across cells. Another important result of this series of tests is the proof that cells can endure high temperatures for a short length of time, but that they will not survive if exposed to even moderate temperatures for an extended period of time, as shown in Fig. 3.15. This is very useful information for microscopists who undertake nonlinear imaging with ultrashort laser pulses, since it allows them to see finer details. The experiment provides compelling evidence that high irradiances are preferable in most cases because they produce strong signals and allow one to image the sample in a short period of time without causing damage.

Continuing on the result obtained in the second experiment, which was conducted in scanning laser illumination configuration, we obtained for the average laser power an exponent $k_0 = 1.0$. Given the different (and shorter) exposure times applied with respect to the first experiment, the linear component, thus photothermal damage, is even more predominant. In fact, while in the first experiment we used exposure times from 15 to 480 s, in the second experiment the tested values ranged from 45 to 1800 ms, insufficient time for ROS to be produced in this parameter range.

Eventually, if the same range of parameters is employed, the data-driven approach to data analysis offers a reliable tool for evaluating the experimental circumstances to perform safe nonlinear optical bio-imaging on living HeLa cells. The $5\%$ probability of photodamage seems to be an appropriate safety threshold level for this application, since in our tests, we identified just one damaged experimental points below this level.

## 3.6 Conclusions

With these experiments we set out to study the cellular response induced by exposure to NIR ultrashort laser pulses in live Hela cells, in order to provide useful information to perform biological imaging without damaging the sample under observation. By focusing our study on a few parameters and narrowing the range of values to explore, we were able to characterize the type of photodamage that occurs and define experimental safety conditions that allow performing nonlinear optical imaging without causing the death of the cells observed. Phototoxicity in biological samples is a very broad and complex subject, characterized by many questions still open. In addition to the many variables that one has to manage, one has to deal with the inherent variability of biological organisms. Despite the enormous challenge of approaching such a topic, continuing research in this area is of fundamental importance given the continuous development of photonic technologies and their possible translation into the biomedical field.

## CHAPTER 4

# Multimodal nonlinear optical microscopy of murine spine samples

This chapter presents the result of the fruitful collaboration with the group of Dr. Sobacchi from Humanitas-Clinical and Research Center in Milan, Italy. The purpose of this collaboration was to test the applicability and advantages that multimodal nonlinear optical microscopy could bring to the pathophysiological study of bone samples. The use of our nonlinear technology on samples of murine vertebrae has proved extremely promising: quantitative and chemically specific data have been collected effectively, revealing informations that were not evident with standard analyses.

## Introduction

Bone is a complex specialized connective tissue that performs fundamental functions in our body. It is the solid and stable part around which muscles and ligaments are anchored, giving structure to the body. Moreover, it has a protective function for vital organs, such as the braincase, and also a physiologic function being the seat of the hematopoietic and mineral homeostasis activities. This tissue is made up of both organic and inorganic materials. The organic part is composed mainly of type-I collagen fibrils, which is organized in a honeycomb matrix structure, proteins, and water, and it is responsible for bone elasticity and fracture resistance. On the other hand, the inorganic component consists mainly of phosphate and calcium mineral salts, such as hydroxyapatite crystals, a mineral salt whose bonds provide the collagen matrix its rigidity and hardness, giving the characteristic firmness to the bone structure [160]. Bone matrix is constantly resorbed and regenerated during a process called bone remodeling, which is regulated by its cells and a variety of local and systemic stimuli. The equilibrium of this incredibly complex system can be altered under pathological conditions, leading to changes in bone structure and mechanics [8].

In their seminal study "Absence of Dipeptidyl Peptidase 3 (DPP3) Increases Oxidative Stress and Causes Bone Loss" [116], Menale and colleagues demonstrated the significant role played by the enzyme DPP3 in maintaining bone homeostasis, suggesting that it could be potentially used as a new marker of bone loss pathologies in humans. In their experimental work they employed well-established techniques in the biomedical field such as immunohistochemistry, micro-computed tomography or fluorescence microscopy. Since modern optical technologies are enabling significant advancements in medical imaging and pathological analysis of biological material, they decided to expand their study and explore the opportunities that nonlinear optical microscopy could offer them. So, a very productive collaboration between our research teams was opened.

In this chapter, the results obtained with multimodal NLO microscopy by examining the bone tissue composition in pathologic circumstances in mouse spine sections are presented. As a model of bone loss due to increased oxidative stress, we used the DPP3 Knock-out (KO) mouse model provided by Menale and coworkers [116]. A multimodal custom-built microscope was used to investigate spine sections from wild-type (WT) and knock-out (KO) mice. The microscope worked in 4 different modalities: bright-field, SHG, TPEF and SRS. The latter technique has been exploited at two different Raman shifts, 2850 $\mathrm{cm}^{-1}$ and 2920 $\mathrm{cm}^{-1}$, typical of lipids and proteins respectively. The imaging data was examined with the use of specialized software, algorithms, and statistical analysis tools. As a result, we were able to identify variations between the two sets of samples (WT and KO) that would otherwise go unnoticed by traditional analysis, indicating how promising multimodal NLO microscopy is to study bone tissue.

## 4.1 Materials and Methods

In this section sample, protocols, procedures and experimental setup used in this experimental study will be presented in a detailed way.

### 4.1.1 Tissue samples

Murine spine tissue samples from two different study groups were provided by Humanitas Clinical and Research Center (Milan, Italy). Mice from the pathology-bearing group (sample size n = 3), *i.e.* knock-out (KO) models, belonged to a lineage of animals in which the dipeptidyl peptidase 3 (DPP3) gene was ubiquitously inactivated, inducing bone-loss related symptomatology [116]. The other group of mice, *i.e.* wildtype (WT) models, constituted the control group for the experiment (sample size n = 3). Both KO and WT mice were bred in a specific-pathogen-free animal facility, under a 12-hour dark/light cycle, with adequate supplies of water and food. All the procedures involving mice were performed in accordance with the ethical rules of the Institutional Animal Care and Use Committee of Humanitas Clinical and Research Center and with international laws (Italian Ministry of Health, protocol n.07/2014-PR). Euthanasia via $CO_2$ asphyxiation was practiced on the mice; from each mouse, lumbar spine tissues were collected, fixed in $4\%$ PFA and promptly embedded in methylmetacrilate, without any decalcification procedure. Six $\mu$m thick sections were placed on polylisine-coated BK7 glass slides to preserve them. In order to perform microscopy experiments, the sample is then deplasticized and attached on a #1.5 quartz coverslip, with an average thickness of 170 $\mu$m.

The choice of the material for the coverslip is critical for the quality of the microscopy studies. Common glass slides suffice for most of conventional microscopy and spectroscopy applications in the visible to IR light range; nonetheless, its transmission efficiency drops close to the UV-visible range. On the other hand, quartz coverslips possess an elevated and uniform transmission spectra, covering the whole range of frequencies of interest and represents the high standard in NLO microscopy research. Because of these reasons and considering the low power available on the Stokes branch, it was chosen to operate on 170 $\mu$m quartz coverslip substrates for multimodal nonlinear optical imaging experiments carried out in the context of the present chapter. The configuration adopted during experiments, the best one for imaging acquisition, is depicted in Fig. 4.1.

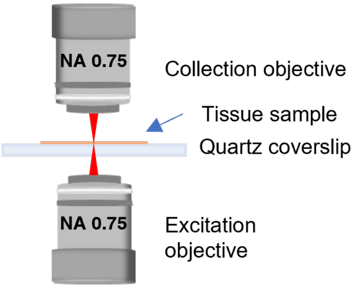

**Figure 4.1:** *Schematic representation of the experimental configuration of tissue sample and excitation and collection objective. Size not in scale.*

### 4.1.2 Multimodal nonlinear optical microscope

In VIBRA - Nonlinear Optical Microscopy Lab, we developed a multimodal NLO microscope using only off-the-shelf components. The setup is completely accessible and each part is easily reconfigurable. The microscope is fed by an ultra-short pulsed fiber-based laser source [34]. In this subsection a clear presentation of the experimental setup will be provided, starting from the hardware components (laser source, excitation optics, etc.) and ending with software.

#### Laser source and beam manipulation

In this setup a mode-locked Erbium:fiber oscillator (Toptica Photonics, Germany) with a repetition rate of 40 MHz is employed. The oscillator feeds three independent Er-doped fiber amplifiers (EDFAs, referred to as Arm 0, Arm 1 and Arm 2), each of them yielding 350 mW output power at a central wavelength of 1560 nm, thus the three EDFA outputs are synchronized and coherently in phase. Moreover, three silicon prism pairs compress the pulse duration at the source up to less than 100 fs. The first optical element placed on the optical path of the Arm 0 output is a half-wave plate (HWP) followed by a polarizing beam splitter (ThorLabs, USA). The combination of these two optics allows to select polarization and power of the laser beam. Then, beam is sent to 10-mm-long MgO-doped periodically poled lithium niobate (PPLN) crystal with a poling period of 19.3 $\mu$m. The PPLN doubles the Arm 0 frequency, generating a second-harmonic beam at 780 nm, that we used as pump for coherent Raman microscopy modalities. The resulting maximum laser power of this pump beam amounts to 90 mW, that is modulated by an acousto-optic modulator (AOM) at 1 MHz [35]. The Arm 1 output is coupled to a highly non-linear fiber (HNLF), with 3.7 $\mu$m core diameter and approximately 7 cm length, which causes anomalous dispersion and broadens the input spectrum. Because of this spectral broadening, side-lobes are generated, both at longer and at shorter wavelengths than the input fundamental one at 1560 nm. Two modes of propagation are possible: in a soliton regime at longer wavelengths, while in the normal dispersion regime at shorter wavelengths. By adjusting the silicon prism pair insertion, the dispersion of the input pulse entering the HNLF can be regulated, thus influencing the position of the peaks associated to the newly generated high frequency and low frequency components. Therefore, the longer wavelengths component can be modulated between 1700 nm and 2100 nm, whereas the shorter wavelengths component down to 1000 nm. Finally, the resulting white light output enters a 10-mm-long PPLN crystal with a fan-out grating design, making it possible to obtain narrowband Stokes pulses, which are tunable in wavelength in the range from 950 nm to 1050 nm and a linewidth that ranges from 18 $\mathrm{cm}^{-1}$ to 30 $\mathrm{cm}^{-1}$. The tuning operation is user-controllable and it is performed through a Kinesis motorized stage and its dedicated software (ThorLabs, USA). Therefore, $\Omega = \omega_p - \omega_S$ in the 2300-3300 $\mathrm{cm}^{-1}$ vibrational range, effectively covering the whole CH-stretching region, which is fundamental to select the appropriate Raman shift for bio-applications.

For the SRS signal we decided to opt for the in-line balanced (IBD) detection scheme. To do this it is necessary to create two collinear replicas of the Stokes pulse, orthogonally polarized and temporally shifted. A HWP and an $YVO_4$ birefringent crystal are inserted along the optical path of the beam. The HWP modifies the polarization of the incident pulse, positioning it at 45° to the crystal's fast and slow axes. The optical characteristics of the crystal cause the two pulse projections to divide in time, propagating in the crystal at different phase velocities, $c_0/n^o$ and $c_0/n^e$, where $c_0$ is the speed of light in vacuum and the apices $o$ and $e$ of the index $n$ are for ordinary and extraordinary. Thus, while the beam propagates in the birefringent crystal, the pulse projections along the two axis shift temporally by a quantity $\tau = L/c_0(n^e - n^o)$. A diagram of this process is provided in Fig. 4.3. One of these two replicas will be temporally and spatially overlapped with the pump pulse, using a delay line and a dichroic mirror, and used to probe the sample and generate the SRS signal, while the other one will be use as reference, allowing us to recover the weak SRG signal after lock-in demodulation. [35]. In Fig. 4.2 a schematic representation of the microscope setup is provided.

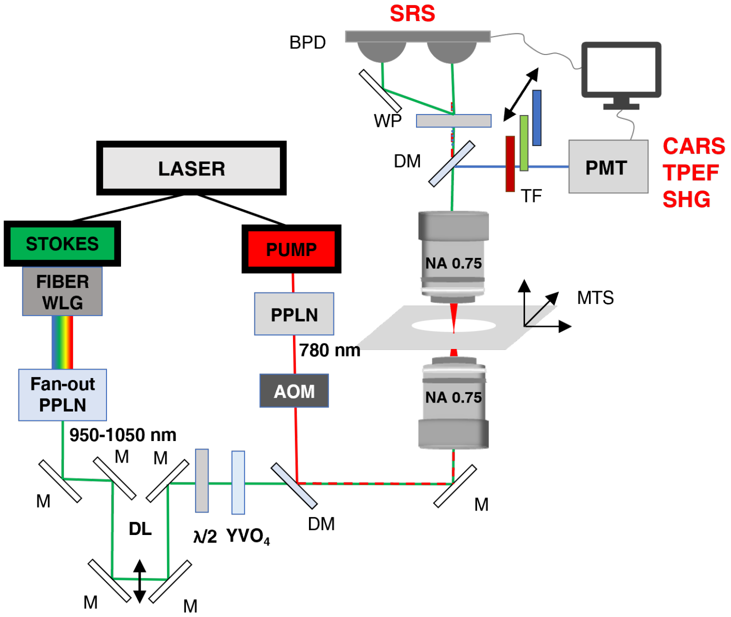

**Figure 4.2:** *Schematic representation of the experimental setup. M, mirror; DL, delay line; AOM, acousto-optic modulator; DM, dichroic mirror; MTS, motorized translational stage; TF, tunable filters; WP, Wollaston prism; BPD, balanced photodiode; PMT, photomultiplier tube.*

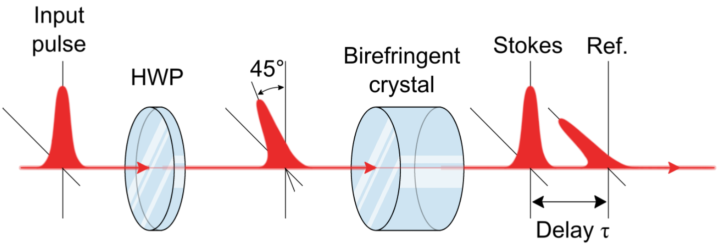

**Figure 4.3:** *Generation of the two Stokes pulses with perpendicular polarization for IBD detection of SRS signal, using a half-wave plate (HWP) and a birefringent crystal.*

### Microscopy unit

The two combined laser beams arrive at the microscopy unit. The microscope presents an inverted configuration and the nonlinear signals are detected in the forward direction. The beams are directed into the back aperture of an LD EC Epiplan-Neofluar 100x/0.75 DIC M27 objective (Zeiss, Germany) with 4-mm working distance, used as illumination optics, which focused them on the sample. The sample is placed on a custom-designed sample holder, mounted on the scanning unit. A first motorized translation stage (Mad City Labs Inc, USA) on the vertical axis ($z$-axis) is used to position the sample in the focal plane, and a second one (8MTF-75LS05 Standa, Lithuania) provides the movement on the horizontal plane ($xy$-plane). The vertical translator has a resolution of 50 nm, while the xy-stage, the same used in Section 3.2.4, has a resolution of 125 nm. The combination of these two translators allows us to move the sample in three dimensions, and it is useful both for positioning the sample on the region of interest and controlling the scanning pattern during the imaging process. Then, the transmitted signals and the nonlinear signals generated are collected via a second identical objective, LD EC Epiplan-Neofluar 100x/0.75 DIC M27 objective (Zeiss, Germany). The long working distance provided by these objectives is convenient, as it facilitates the initial operations of orientation on tissue samples, which typically have dimensions of the order of the centimeters.

### Signal detection

The signals collected by the collection objective continue their path towards the detection systems: a dichroic mirror (cut frequency at 750 nm, Semrock, USA) divides the signals by reflecting photons with wavelengths shorter than 750 nm and trasmitting those with higher wavelengths. The reflected photons are directed to a photomultiplier tube (PMT) (R3896, Hamamatsu, Japan) assigned to the detection of TPEF and SHG signals, selected using appropriate sets of filters. The use of spectral filters guarantees that only the correct signal arrives to the selected detector, with no contributions from the pump and Stokes driving fields or from unwanted nonlinear processes. Table 4.1 lists all the employed filters configurations.

The photons transmitted by the dichroic mirror, with a wavelength greater than 750 nm, are sent to a Wollaston prism, which spatially separates the components with orthogonal polarizations, thus it separates the Stokes reference from the Stokes carrying the SRG signal and sends them to two active areas of a balanced photodiode (PDB210A/M, ThorLabs, USA), as shown in Fig. 4.5. Then, a high-speed lock-in amplifier (HF2LI, Zurich

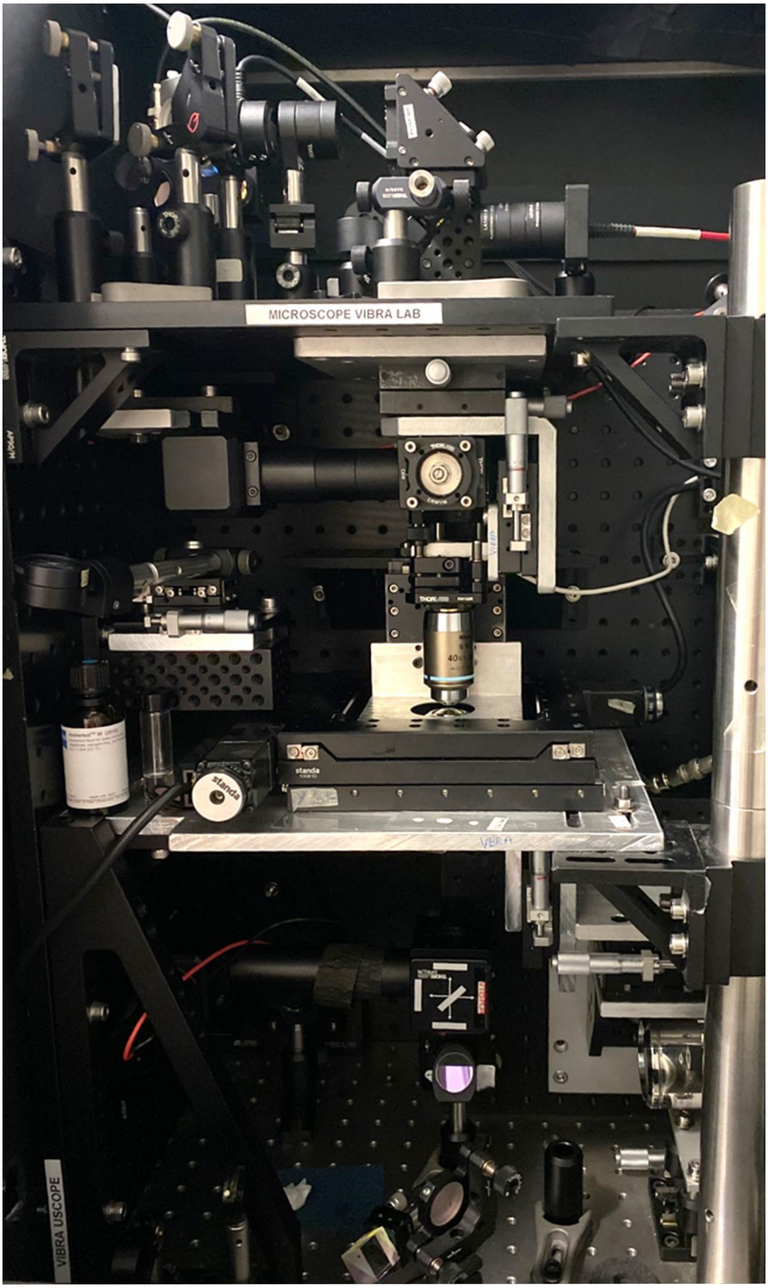

**Figure 4.4:** *Picture of the microscopy unit of the VIBRA multimodal microscope.*

| | Pump/Stokes removal | Signal selection |
|---|---|---|
| **TPEF** | NF 785/33 nm<br>(ThorLabs: NF785-33)<br>SPF 700 nm<br>(ThorLabs: FESH0700)<br>SPF 750 nm<br>(ThorLabs: FESH0750) | SPF 600 nm<br>(ThorLabs: FESH0600) |
| **SHG** | SPF 750 nm<br>(Semrock: FF01-750/SP-25) | BPF 390/18<br>(Semrock: FF01-390/18-25) |

**Table 4.1:** *Schematic of the different filters configurations; NF, Notch filter; SPF, Short Pass Filter; BPF, Band Pass Filter.*

Instruments, Swiss) is employed to extract the SRG signal in a modulation-transfer scheme. This completes the IBD system [35]. The Stokes reference is used to create a transmission image of the sample (bright-field microscopy modality), and accounts for the different transmission intensities due to the morphology difference of the sample.

The output of the PMT and the transmission signal from the photodiode enter as input channels in the Data Acquisition system (DAQ), which transmits them as digital data to the PC.

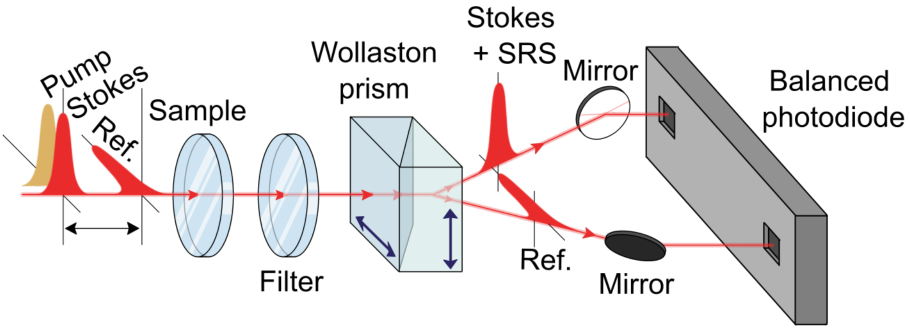

**Figure 4.5:** *IBD detection scheme: interaction of the pulses with the sample and their detection by balanced photodiode.*

### Microscope software

The microscope is controlled via a dedicated computer software, built using MATLAB App Designer®. It allows the user to set all the desired parameters and controls the electronic equipments involved in the measurement. The main window user-interface of the software is presented in Fig. 4.7.

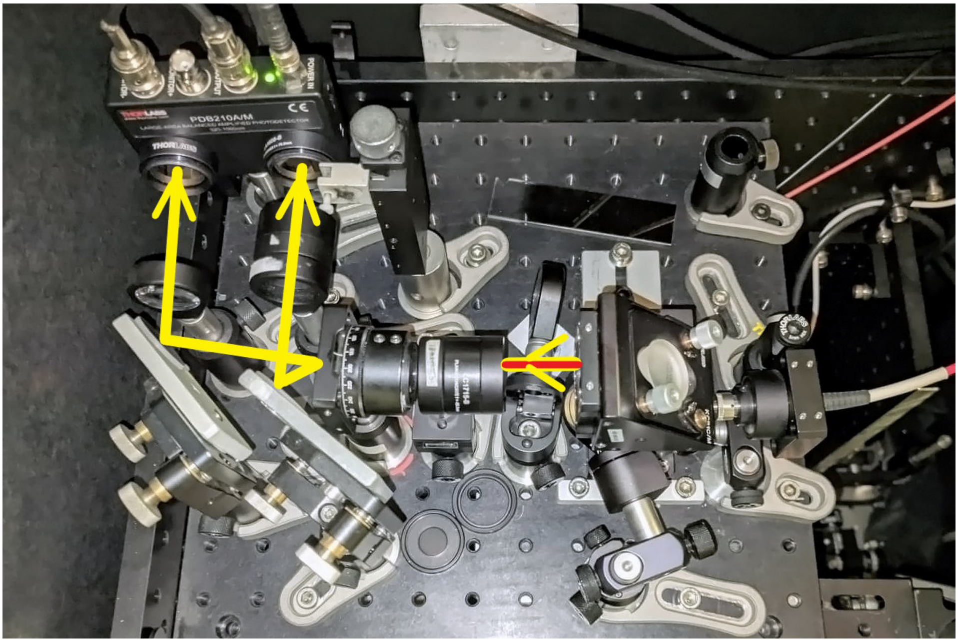

**Figure 4.6:** *Picture of the SRS detection line.*

Log

```
Welcome
Session Started
18-Nov-2020 14:23:57
Getting Ready..
Connection to Mad City Lab...
Mad City Lab initialized
MCL speed: 50.00 um/s
MCL step_size: 10.00 um
standa ready
Connecting DAQ...
DAQ Connected.
0
Galvo Moved
Default Galvo settings loaded
Starting Motor Control..
Motor Control Activated
Computing Stokes parameters based
on motor position..
Done!
```

Mad City Vertical Axis
Position [um] 0
Speed [um/s] 50
Step Size [um] 10

Stokes
Position 8.6691 [mm]
Wavenumber 9875.204 [cm-1]
Lambda 1012.637 [nm]
Raman Shift 2945 [cm-1]
From 2500
To 3200
Steps 60
StepSize 11.67
☐ Save

Galvos
X [V] 0
Y [V] 0
Npix 200
Ampl [V] 1
RDT [s] 0.5
☐ Save
n 50
PDT [s] 0.1
Rate [Hz] 20000
Circshift 0
1 V = 70 um

Full Scanner
Wavenumber
From 2945
To 2945
Steps 1
StepSize 0
Vertical
Tot Range [um] 0
StepSize [um] 0
Steps 1

**Figure 4.7:** *Vibra microscope acquisition software main interface.*

On the bottom part, three matrix images show the pixel intensity in real time during acquisition: the transmission image forms on the left via the photodiode detection of Stokes reference, the PMT signal (CARS/TPE-F/SHG) is displayed in the centre and finally the SRS signal is shown on the right.
The user-controllable functions are organized in windows, each containing different panels. The relevant software windows in this experimental work are the following:

- **General Controls**: the *Mad City Vertical Axis* panel allows one to move the sample holder in the optical axis, controlling the vertical translational unit, when the focus needs to be adjusted on the sample. The panel *Stokes* allows one to select the appropriate Raman shift $[cm^{-1}]$ to stimulate the vibrational mode of the analyte of interest (Fig. 4.8a).
- **Standa**: contains all the parameters to regulate the movement of the horizontal translation unit before and during the acquisition. The panel *Setting standa position* allows the user to freely move the sample in the X and Y direction before the start of the measurement; *Setting scanned area* is used to specify the X and Y dimension of the image (in $\mu$m), the resolution in pixel, the pixel dwell time (PDT [s]), the number of points sampled per pixel (n) and the correction to the circular shift of the acquired rows (*circshift*, in number of pixels). The *circshift* function is very useful because it allows one to correct the artifacts due to the serpentine scanning pattern and realign correctly the data acquired on scanned lines in different directions. The *START* button initiates a single acquisition, which can be saved in a PC folder of choice with the *SAVE_std* button. The data are saved in the *.txt* format. When the portion of the sample is too extended (in the order of mm) to be imaged in a single acquisition, multiple consecutive acquisitions, called tiles, must be taken. The *Autotiling* function manages the tiling operation. The total dimensions (in $\mu$m) of the final image and all the other parameters are user-controllable. The saving folder is set as soon as the Autotiling *START* button is pressed (Fig. 4.8b).
- **Keep-In-Focus**: this function allows to automatically increase or decrease the position of the sample on vertical axis (in $\mu$m) every time $n$ columns are scanned and/or an entire row of tiles has been imaged. In fact, while in a single acquisition it is safe to assume that the focus stays constant, it is highly probable that, when scanning over lengths

of millimeters, the focus on the sample has to be adjusted, because of irregularities in the biological specimen and for the not perfect flatness of the sample (Fig. 4.8c).

Log

```
Welcome
Session Started
30-Sep-2021 16:21:01
Getting Ready..
Connection to Mad City Lab...
Mad City Lab initialized
MCL speed: 50.00 um/s
MCL step_size: 10.00 um
standa ready
Connecting DAQ...
DAQ Connected.
0
Galvo Moved
Default Galvo settings loaded
Starting Motor Control..
Motor Control Activated
Computing Stokes parameters based
on motor position..
Done!
```

Mad City Vertical Axis

Position [um] 0
Speed [um/s] 50
Step Size [um] 10

Stokes

Position 9.2105 [mm]
Wavenum 9975.144 [cm-1]
Lambda 1002.491 [nm]
Raman Shift 2850 [cm-1]
From 2500
To 3200
Steps 60
StepSize 11.67
☐ Save

Galvos

X [V] 0
Y [V] 0
Npix 200
Ampl [V] 1
RDT [s] 0.5
☐ Save
n 50
PDT [s] 0.1
Rate [Hz] 20000
Circshift 0
1 V = 70 um

Full Scanner

Wavenumber
From 2865
To 2865
Steps 1
StepSize 0

Vertical
Tot Range [um] 0
StepSize [um] 0
Steps 1

Setting standa position

Displacement [um] 0
Act Pos X [um] 0
Act Pos Y [um] 0

Setting scanned area

Dim X 0
Dim Y 0
N_pix_X 0
N_pix_Y 0
PDT [s] 0.1
n 10
RDT std [s] 0
CircShift_std 0
Rate [Hz] std 0

Autotiling

Base Dim 0
N_pix_base 0
Tot Dim x 0
Tot Dim y 0
PDT [s] 0
n 0
CircShift_aut 0
RDT aut [s] 0.000

Parameters

move the focus of: every n columns
X-Focus 0 [um] 0 [columns]
move the focus of:
Y-Focus 0 [um] every Dim_Y rows

NB: Put only positive values
NB: Put only positive values
The software will select the correct direction itself.

**Figure 4.8:** *Vibra microscope acquisition software windows: a) General Controls panel; b) Standa panel; c) Keep-In-Focus panel.*

### 4.1.3 Image acquisition settings

For each mouse used in this study, we analyzed a complete vertebra. Of each vertebra, six images were produced: bright-field, TPEF, SHG with polarization parallel to the craniocaudal axis of the spine, SHG with polarization perpendicular to the craniocaudal axis of the spine, SRS at Raman shift 2850 $\text{cm}^{-1}$ and SRS at Raman shift 2920 $\text{cm}^{-1}$. The laser power was kept constant at 20 mW for the pump beam and 1.2 mW for the Stokes beam. Images were acquired with a pixel dimension of 1 $\mu$m and a pixel dwell time of 5 ms.

### 4.1.4 Image analysis

#### Analysis of collagen production

One of the objectives of this work was to verify if there were appreciable differences in the amount of collagen expressed in the two murin models. To this aim, we compared the average raw SHG pixel intensity displayed by our set of WT and KO individual murine models, computed via ImageJ. For this calculation we considered the entire available area of cortex ad trabeculae.

#### Analysis of collagen fibrils orientation â Sobel algorithm

For the analysis of collagen fibrils directionality, we applied a Sobel filtering ( [162]) algorithm implemented in Python on SHG images of WT and KO models. The Sobel-Feldman operator (or simply, the Sobel operator) is a discrete differentiation operator that calculates the approximate gradient of an image and it has been famously employed in image processing, for example as an edge-detector filter to highlight the high spatial frequency regions of an image [141] and in machine vision [175].

In the theory of gradient approximation, it is assumed that there exists an underlying continuous differentiable intensity function, such that the discrete points of the digital image are actually the sampling points of the source image. The classical Sobel operator employs (3,3) dimensional matrices to keep a low computational effort while maintaining a sufficient level of accuracy. From a practical point of view, the Sobel operator consists of two (3,3) kernels, which are cross-correlated with the input image. These cross-correlation kernels can be simplified as the products of an averaging and a differentiation kernel; because of this, the Sobel operator has a smoothing effect that makes the operation less sensitive to noise [144]. The result brings two approximate derivative images, one for the horizontal direction, $\mathbf{G}_x$, and the other for the vertical one, $\mathbf{G}_y$, defined as:

$$\mathbf{G}_x = \begin{bmatrix} +1 & 0 & -1 \\ +2 & 0 & -2 \\ +1 & 0 & -1 \end{bmatrix} * \mathbf{A}, \tag{4.1}$$

$$\mathbf{G}_y = \begin{bmatrix} +1 & +2 & +1 \\ 0 & 0 & 0 \\ -1 & -2 & -1 \end{bmatrix} * \mathbf{A}. \tag{4.2}$$

The two gradient approximations can then be combined to give the absolute magnitude of the gradient at each pixel: $|\mathbf{G}| = \sqrt{\mathbf{G}_x^2 + \mathbf{G}_y^2}$.
More interestingly, it is possible to calculate the orientation of the gradient pixel-wise as

$$\theta = \arctan \frac{\mathbf{G}_y}{\mathbf{G}_x} \tag{4.3}$$

with $\theta$ expressed in radiants. Considering for example two consecutive pixels on the same row, the first being black and the second white, the output will be 0, as this is the direction of maximum contrast, from left to right, in the image featuring a vertical edge. The other angles are calculated anticlockwise from $-\pi/2$ to $\pi/2$. In Fig. 4.9, an example of application on a simple (6,6) intensity matrix is reported. The result is a 4x4 theta map.

For its properties, the Sobel operator can be applied to swiftly estimate the orientation of the microscopic features contained in a digital microscopy image. Running the algorithm on a (N,N) input image, the result is saved in a (N-2,N-2) matrix, called *theta map*, where the two lost rows and columns amount to the cross-correlation operation. The theta map can be opened like a standard image, using a cyclic colormap (*e.g. twilight*, from the common visualization library matplotlib, in Python) to have a qualitative depiction of the features orientation in the source image.

### Analysis of lipids and proteins distribution

Images captured in SRS modality were used to assess whether a lack of DPP3 could induce changes in the distribution of protein and lipid content. To do so, the ratio between the average signal intensity in the bone tissue and in the bone marrow has been calculated and the results obtained in the WT models have been compared to the one obtained in the KO samples. This operation was performed on the images obtained at both Raman shifts explored, 2850 cm$^{-1}$ and 2920 cm$^{-1}$.

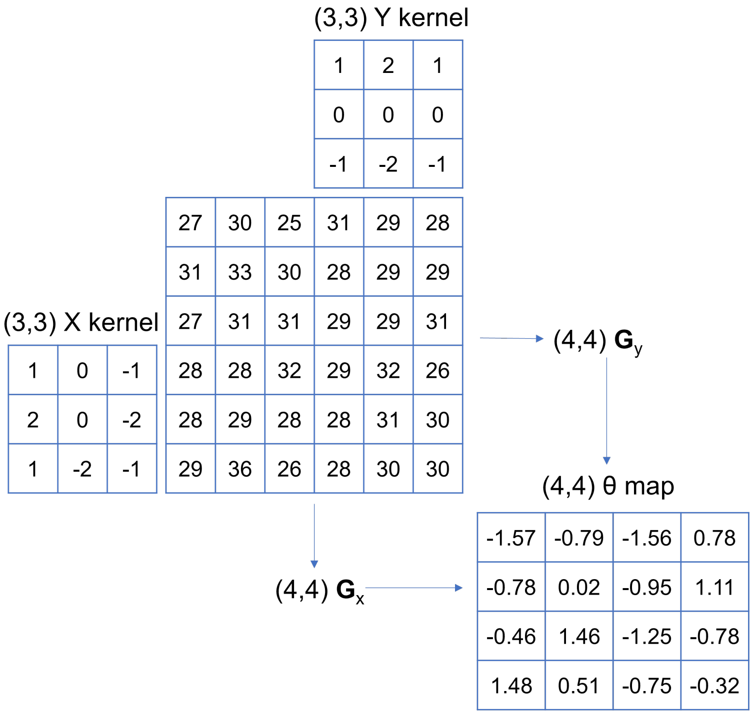

(3,3) Y kernel

| | | |
|---|---|---|
| 1 | 2 | 1 |
| 0 | 0 | 0 |
| -1 | -2 | -1 |

(3,3) X kernel

| | | |
|---|---|---|
| 1 | 0 | -1 |
| 2 | 0 | -2 |
| 1 | -2 | -1 |

| | | | | | |
|---|---|---|---|---|---|
| 27 | 30 | 25 | 31 | 29 | 28 |
| 31 | 33 | 30 | 28 | 29 | 29 |
| 27 | 31 | 31 | 29 | 29 | 31 |
| 28 | 28 | 32 | 29 | 32 | 26 |
| 28 | 29 | 28 | 28 | 31 | 30 |
| 29 | 36 | 26 | 28 | 30 | 30 |

(4,4) θ map

| | | | |
|---|---|---|---|
| -1.57 | -0.79 | -1.56 | 0.78 |
| -0.78 | 0.02 | -0.95 | 1.11 |
| -0.46 | 1.46 | -1.25 | -0.78 |
| 1.48 | 0.51 | -0.75 | -0.32 |

**Figure 4.9:** *Sobel operator applied to a fictional (6,6) image. The cross-correlation kernels are shown on the top and left side, respectively, of the input image. The tangent inverse operation is performed, resulting in a* $(4,4)$ *angular representation of the gradient orientation.*

#### Statistics

Statistical analysis was performed using MannâWhitney test (GraphPad Prism 5.0; GraphPad Software, Inc). Statistical significance was considered where $p < 0.1$ (90% CI). All data are presented as mean ± SEM (standard error of the mean).

## 4.2 Results and Discussion

### 4.2.1 Multimodal nonlinear imaging

Thanks to the VIBRA microscope we performed multimodal, non-invasive, label-free imaging, obtaining a spatially extended (field of view (FOV) on the scale of millimeters) characterization of the major biochemical components that constitute the murine spine sample, with the aim of assessing the phenotypic differences between the WT model and the KO model.

From bright-field images, produced by detecting the linearly transmitted Stokes beam, it is possible to derive morphological information on the samples under observation. In Fig. 4.10 bright-field images of a WT sample (panel a) and a KO sample (panel b) are presented.

In these images (Fig. 4.10) four different biological tissues can be distinguished. The prevalent one is the bone marrow: it appears in the middle section of the FOV, inside vertebrae, as light gray and grainy, being composed of white and red blood cells [116]. In the darker gray areas, there are two types of bone tissue: the trabeculae, which are interconnected thin rod-shaped structures of spongy and porous bones that fill the bone marrow [115], and the cortex (or cortical bone), which is an elongated bone tissue that runs vertically through the entire sample from top to bottom, encasing and protecting the marrow. In addition, the cortex is the skeleton's most thick outer layer, which bears the most of the mechanical stress [147]. Then, immediately outside the cortex, the skeletal muscle tissue is visible. It appears almost transparent. Last, the white spots in the bone marrow are empty and the result of the not perfect processing of the murine spine sample. A clear indication of the various zones of the fabric is given in Fig. 4.10. The KO models do not exhibit any distinguishing characteristics when compared to the control group at this initial level of analysis, which is performed using a linear transmission signal.

The signal in the TPEF modality is generated by stimulation of intrinsic intracellular fluorophores, such as NADH and FAD. Their existence indicates the presence of oxidative and glycolytic metabolic processes at the cellular level [193]. Two images (WT in panel a and KO in panel b)

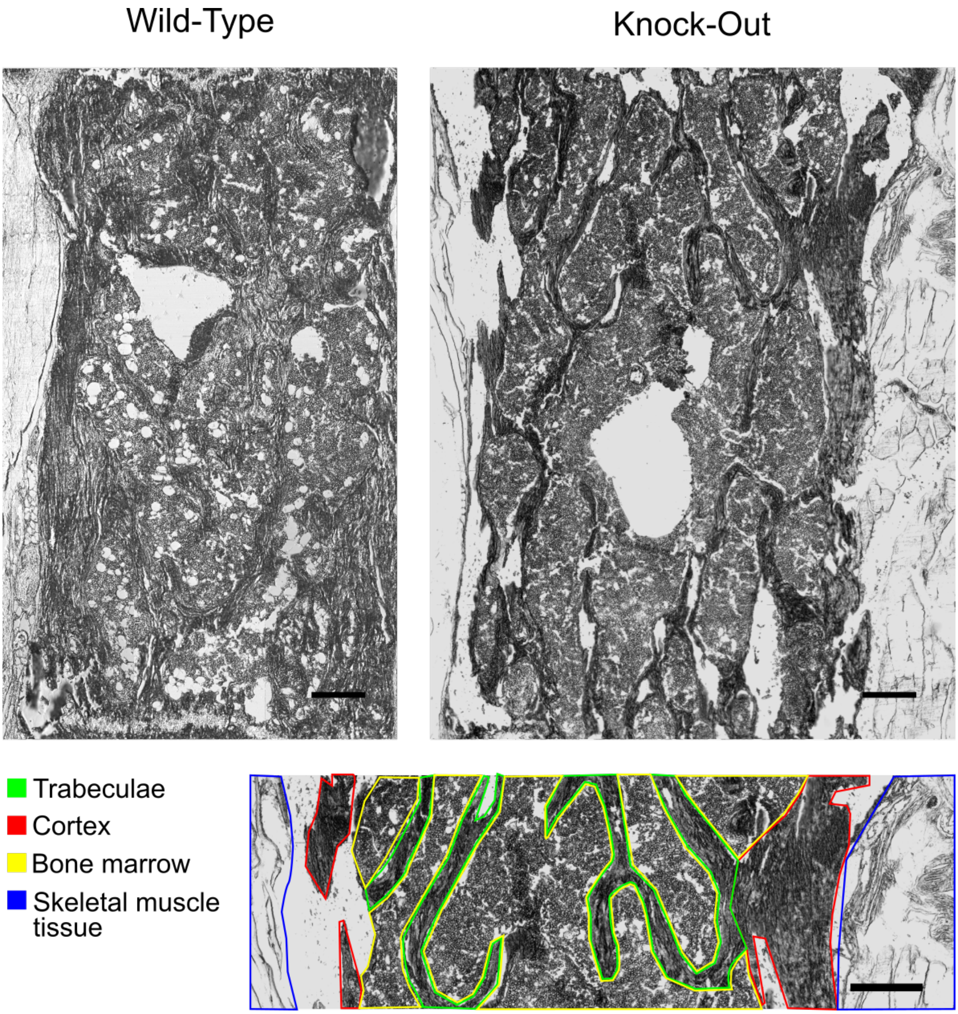

**Figure 4.10:** *Bright-field images of a WT murine model sample and a KO murine model sample. At the bottom, the edges of the different areas of the fabric are highlighted with different colors: trabeculae in green, cortex in red, bone marrow in yellow and skeletal muscle tissue in blue. Scale bar: 200 μm.*

captured in TPEF modality are shown in Fig. 4.11. Looking at these images, one can not appreciate significant differences between the two murine models, since the two signals are comparable. Each picture shows a distinct difference in fluorescence activity between the bone tissue and the marrow, which is filled by red blood cells. TPEF signals from intracellular endogenous fluorophores in the bone marrow area are stronger because the cell density (the number of cells per unit volume of tissue) in bone marrow is higher than in bone tissue. Both images (panel a and b of Fig. 4.11) clearly show that the bone marrow, which contains blood cells, is far more fluorescently active than the bone tissue. In fact, bone marrow has a higher cell density than bone tissue, which explains the stronger TPEF signal from intracellular endogenous fluorophores seen in the marrow area compared to the rest of the bone tissue sample. Similarly, the brightest spots inside the bone marrow suggest an increased cell density. Magnified details of a TPEF image is shown in Fig. 4.12, revealing vivid TPEF lines along the cortical and trabecular bone boundaries. Because of the increase in metabolic activity along bone margins during the process of bone remodeling, which occurs continually in the context of bone homeostasis, this unusual signal is produced [67].

The non-centrosymmetric structure of collagen fibrils, as well as their remarkable second-order nonlinear susceptibility, are responsible for the generation of the SHG signal. In the SHG modality, two acquisitions were performed on each mouse spine sample. In the first one, the polarization of the pump beam was parallel to the spine's craniocaudal axis. In the second acquisition, SHG measurements were carried out using a pump beam that was perpendicularly polarized with respect to the craniocaudal axis of the spine. In each acquisition, the pump polarization was maintained fixed while the sample was rotated by 90° in order to retain all experimental conditions except the pump polarization with respect to the sample orientation. In Fig. 4.13 images obtained with parallel and perpendicular pump polarization for WT and KO samples are reported. Knowing that SHG signals are strongly correlated with non-centrosymmetric matter concentrations and looking at these images, we can deduce, as expected, that collagen fibers are mainly present in cortex and trabeculae. In addition, unlike the two previous microscopy modalities, in this case it is possible to notice qualitative differences between the two murine models: in fact, the KO model image appears to be brighter than the WT, suggesting a different production of collagen between the two models. So, in order to determine the quantity of collagen produced in the two model and the spatial orientation of collagen fibrils, a quantitative statistical analysis was performed on

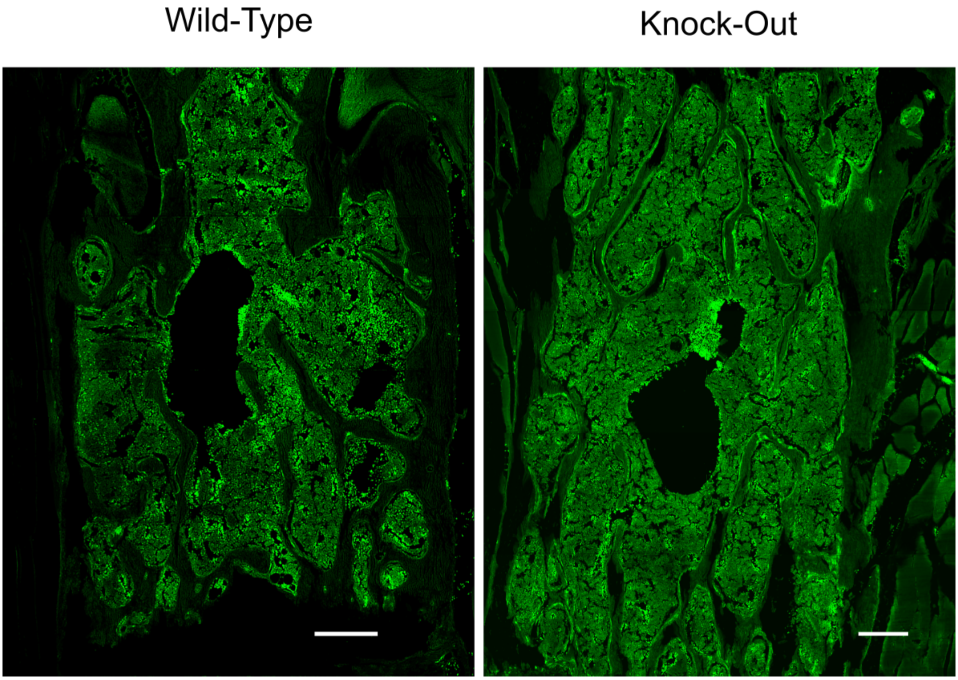

**Figure 4.11:** *TPEF images a WT murine model sample and a KO murine model sample. Scale bar: 200 μm.*

the raw datasets obtained from the SHG channel acquisitions. The results of these analysis are presented in Subsection 4.2.2 and Subsection 4.2.3.

In SRS imaging modality, an approach based on the CH-stretching modes is employed. Lipids and proteins possess strong Raman vibrational response at 2850 $cm^{-1}$ and 2920 $cm^{-1}$, resonant to $CH_2$ and $CH_3$ stretching modes, respectively. The images based on the intensity of these bands provide a pseudo-map of protein and lipid concentration [76]. The images acquired in SRS modality are presented in Fig. 4.14. In this case, the difference in lipid concentration presented by the two samples is immediately evident. In fact, while the healthy (WT) sample has a uniform distribution over all areas of the vertebra, the KO sample instead shows a higher concentration in cortical and trabecular areas than bone marrow. Based on this observation, a further statistical analysis has been made to confirm and quantify this behavior. The results of this analysis are shown in Subsection 4.2.4. Each imaging modality provides complementary information about the sample, and it can be appreciated both singularly and merging multiple images in a sole image, to obtain a richer and more thorough understanding about the overall tissue composition, as shown in Fig. 4.15.

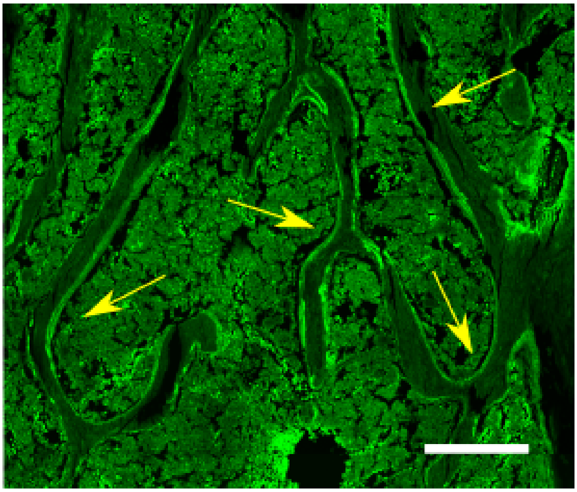

**Figure 4.12:** *detail of tissue acquired in TPEF modality: the yellow arrows highlight the increase in signal due to the metabolic activity along bone margins during the process of bone remodeling. Scale bar: 200 $\mu$m.*

### 4.2.2 Collagen production

Menale and colleagues [116] showed that the Dpp3 gene was correlated to bone loss diseases. The gene regulates the formation of hydroxyapatite (HA) crystals, which are tiny calcium-based plate-shaped crystals that are found in the gap areas between collagen fibers [184]. A crucial role in mineral ion homeostasis is played by HA [14], which is involved in bone regeneration via conduction or by providing a framework for bone repair [82]. Maximum load that the bone can withstand before breaking is the definition of bone strength. Bone mass, size, geometry, and microarchitecture all have a role in mechanical resistance. The degree of mineralization and the organic matrix characteristics (i.e., the orientation and chemical structure of the collagen fibrils) play a critical influence in tissue strength and mechanical qualities when examining the bone tissue [10]. Collagen, in particular, is crucial for bone flexibility, enabling it to be deformed reversibly; type-I collagen, the most abundant kind in bone tissue, matures through enzymatic cross-linking processes and non-enzymatic modifications [156]. Collagen fibrils form an ordered network throughout these maturation stages, in which mineral crystals are arranged in a specific pattern. Thus, variations in the quantity, size, and perfection of HA crystals caused by widespread Dpp3 gene inactivation may account for changes in the orientation and concentration of collagen fibrils in bone tissue [47, 153].

For each image, a background subtraction is performed, where the ROI

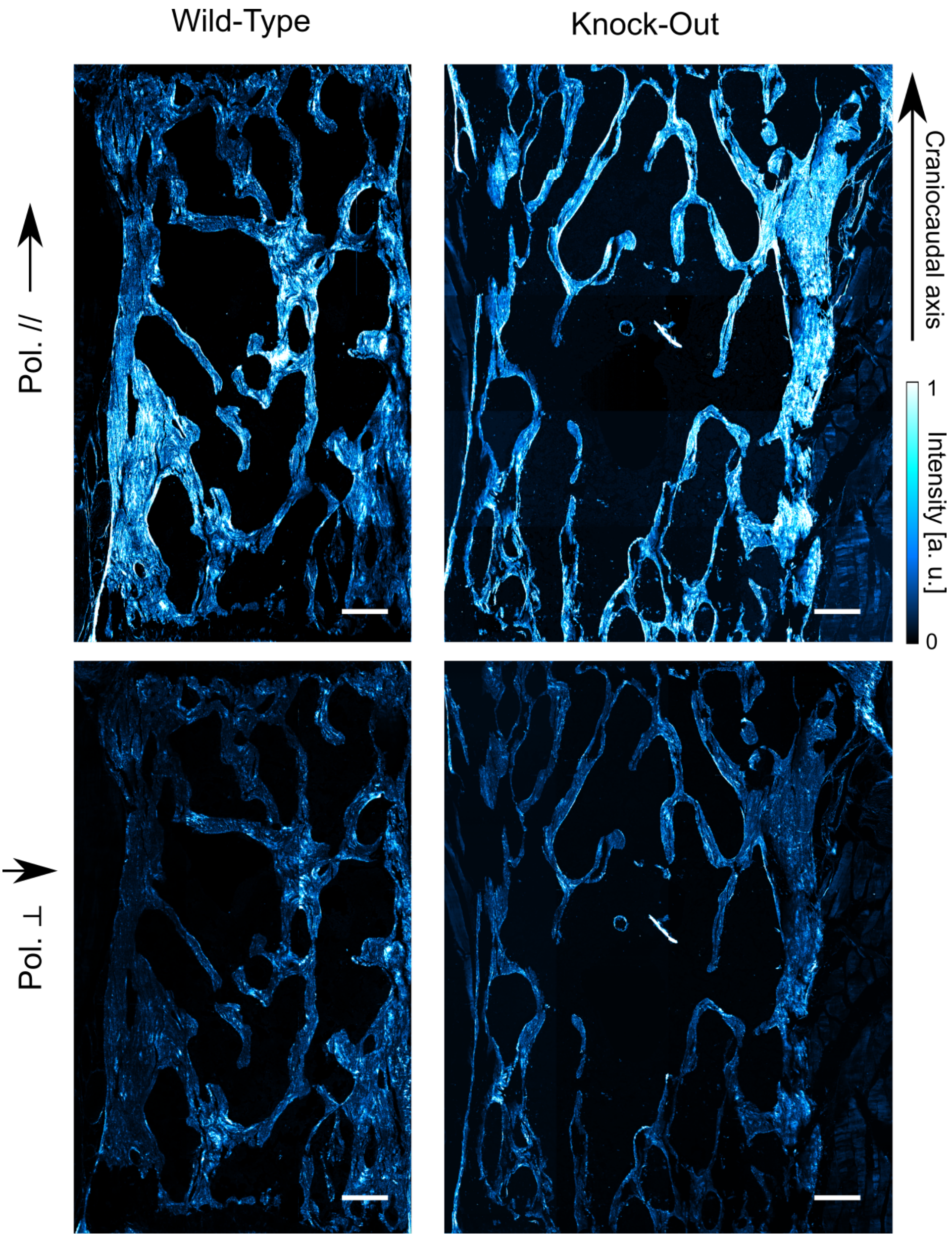

**Figure 4.13:** *SHG images of a WT murine vertebra and of a KO murine vertebra, in two different polarization configuration. In parallel-polarization configuration, the polarization orientation matches the preferential orientation of the collagen fibrils (craniocaudal axis) and the SHG signal is generated more efficiently with respect to perpendicular-polarization configuration. Scale bar: 200 µm.*

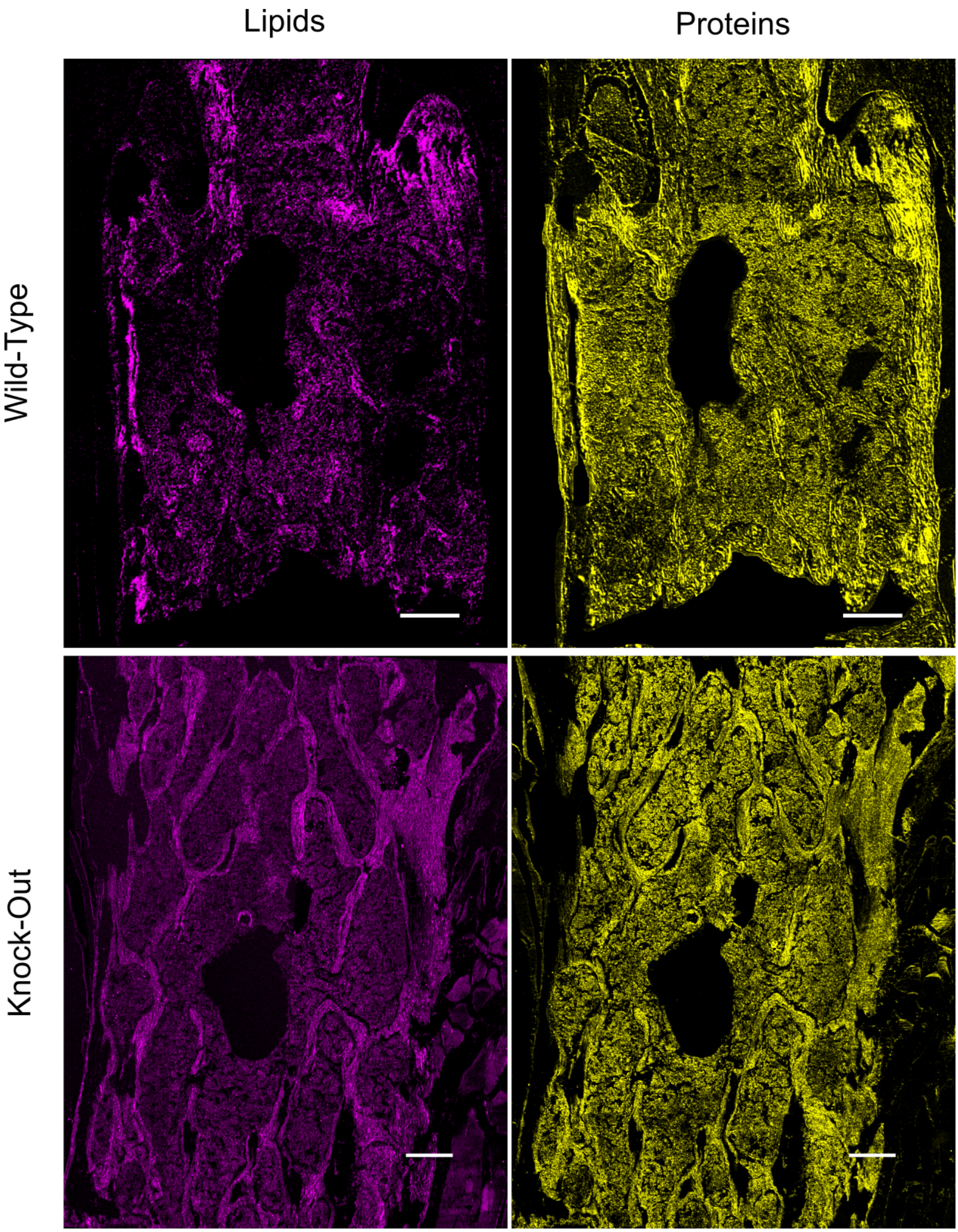

**Figure 4.14:** *SRS images of a WT murine vertebra and of a KO murine vertebra at two different Raman shift: 2850 cm*$^{-1}$ *for lipids and 2920 cm*$^{-1}$ *for proteins. Scale bar: 200* $\mu$*m.*

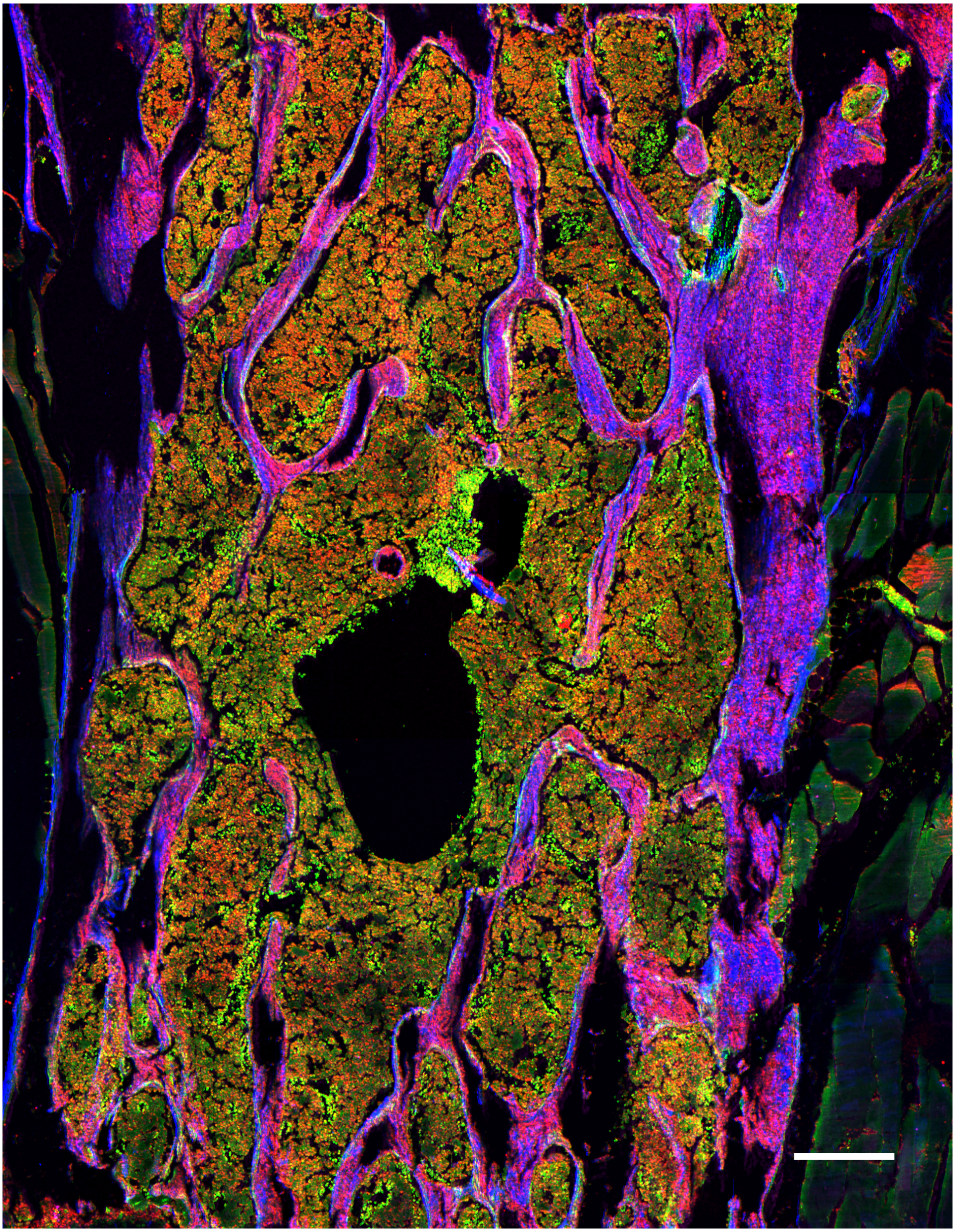

**Figure 4.15:** *Multicolor image of a KO murine spine sample: TPEF signal (green), SHG channel (blue), SRS signal at 2850* $cm^{-1}$ *Raman shift (magenta), SRS signal at 2920* $cm^{-1}$ *Raman shift (red), merged.*

for the mean background estimation is selected from a dark area of the image. The ROI is manually drawn on the figure, using the tools of *ImageJ*, to separate the bone tissue from the skeletal muscle tissue, which shows weak contributions of signal. Thus, the image is cropped and saved. Next, the pixels of the foreground displaying the osseous features are thresholded and selected and their intensities are collected for the subsequent analysis. Since different PMT sensitivities were employed in the SHG image acquisitions, the pixel values had to be scaled accordingly to make them comparable. Thus, the mean value of all the selected pixels is calculated, which is representative of the average SHG signal intensity of the whole image, related to the collagen amount present in the irradiated sample. Such data are employed for the statistical analysis: a set of three average values of SHG intensity from the WT sample group and three average values from the KO sample group, both in vertical and horizontal polarization. The results are presented in Fig. 4.16. The amount of collagen expressed in the KO model is greater than in the WT model, for both polarization orientations, with a relative increase of +183% in the case of polarization parallel to the cranio-caudal axis of the murine spine (**Pol.** //), and an increment of +127% in the case of perpendicular polarization (**Pol.** ⊥). Moreover, the signal intensity in parallel polarization is greater than in perpendicular polarization, as expected, both in WT and KO models: for the WT model, the signal intensity obtained by perpendicular polarization is 56% greater than that obtained by perpendicular polarization, while for the KO model it is 95%.

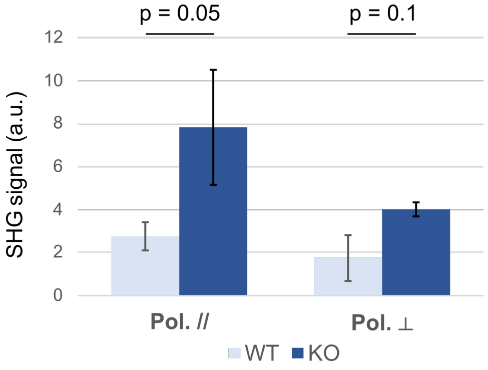

**Figure 4.16:** *Comparison between the amount of SHG signal detected in WT models and KO models, sorted by experimental pump beam polarization. The p values of the tests are reported; mean values ± SEM.*

The same analysis was conducted individually on cortical and trabecular regions, using two non-overlapping ROIs to isolate the two areas in each sample. The results are shown in Fig. 4.17. Again, it is evident that the signal intensity is always greater in the KO model. Looking at each case, for the parallel-polarized pump, the KO model's cortex shows a 202% increase in signal compared to the WO model, while the trabecular area show a 162% increase. For perpendicular-polarized pump, the KO model's cortex shows a 112% increase in signal compared to the WO model, while the trabecular area show a 140% increase. The largest relative increase was achieved in cortical regions with parallel-polarization configuration. This result suggests that fibrillar collagen is differently oriented amongst different regions of the sample; in particular, it implies that the cortical collagen fibrils directionality is more pronounced in the vertical direction. This finding integrates perfectly into the researches, widely documented in literature [163, 164, 185], reporting that the mechanical strength of bone depends primarily on the mechanical strength of the cortex, which in turn is closely related to the organization and orientation of collagen fibrils.

This result intrinsically foreshadows the subject of the statistical analysis done in Subsection 4.2.3, namely the investigation of the directionality of collagen fibrils. Indeed, all other factors being equal, the increased SHG signal in parallel polarization imaging is entirely due to the more efficient alignment of the collagen fibrils with the direction of polarization of the beam, indicating that the fibrils do not have a random orientation. Although the statistical power of the test is limited and adversely affected by the small sample size, the data reveals that the expression of collagen proteins in the KO model may be different than in the control group, indicating that inactivating the DPP3 gene may really influence collagen formation. In fact, those results are in line with the previous study by Menale et al. [116], that showed higher CollaI gene expression during in vitro osteoblast (OB) differentiation and in primary OB (pOB) cultures from DPP3 KO as compared to WT mice. In addition, our fellow researchers at the Humanitas obtained consistent result demostrating higher CollaI gene expression in DPP3 KO flushed bone and increased in vitro collagen production from DPP3 KO vs WT pOBs.

### 4.2.3 Collagen fibrils orientation

The following investigation sought to determine if there were differences in the directionality of collagen fibers between healthy and pathology-bearing mouse samples. Collagen type I is a fibrillar collagen that is mostly composed of rectilinear arrays of collagen fibrils [2]. Collagen is a critical component of bone construction, imparting its pliability, strain hardening, and toughness [59]. Unlike in other tissues, such as skin, fibrils in trabec-

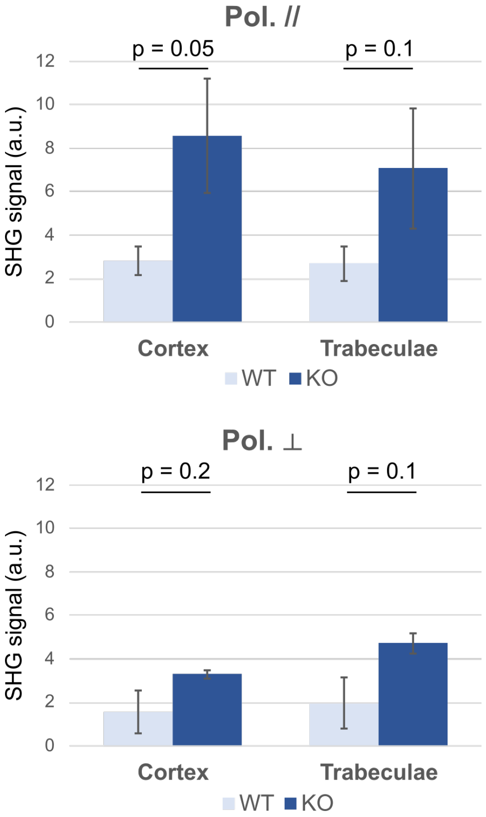

**Figure 4.17:** *SHG signal quantification as detected in WT models and KO models, sorted by experimental pump beam polarization and bone tissue region. The p values of the tests are reported; mean values ± SEM.*

ular and cortical bone may be orientated in either a straight or an oblique direction, even though they retain their regular parallel arrangement. Additionally, the collagen matrix in bone is quite dense. Thus, even in the presence of perfect homeostasis in the bone matrix, the collagen fibers in bone tissue are not consistently oriented in a single direction [79].

Collagen's effects on bone strength and hardness have been extensively studied in a variety of research [20,92,132,183]. In this section, the consequences of DPP3 gene inactivation in KO animals were examined in terms of changes in the orientation of fibrillar collagen, which impairs the mechanical characteristics of bone tissue and may be a contributing factor to the resurgence of osteoporosis-like diseases. Similarly to the analysis described in Subsection 4.2.2, bone tissue in SHG images was divided into two areas, cortical and trabecular, and each region was analyzed independently using a customized algorithm that employs the Sobel operator. Also this time, the findings are expressed in terms of the pump field's polarization direction and presented in Fig. 4.18. For each cortex and trabecular areas, the Sobel algorithm generates a matrix of angles, defined as in Subsection 4.1.4, representing all the orientations of the collagen fibrils contained in the ROIs. Such data are grouped in bins in a one-dimensional array of 75 elements, which represent the fraction of pixels displaying collagen fibrils oriented around a certain angle, spanning from 0° to 180°. Therefore, each

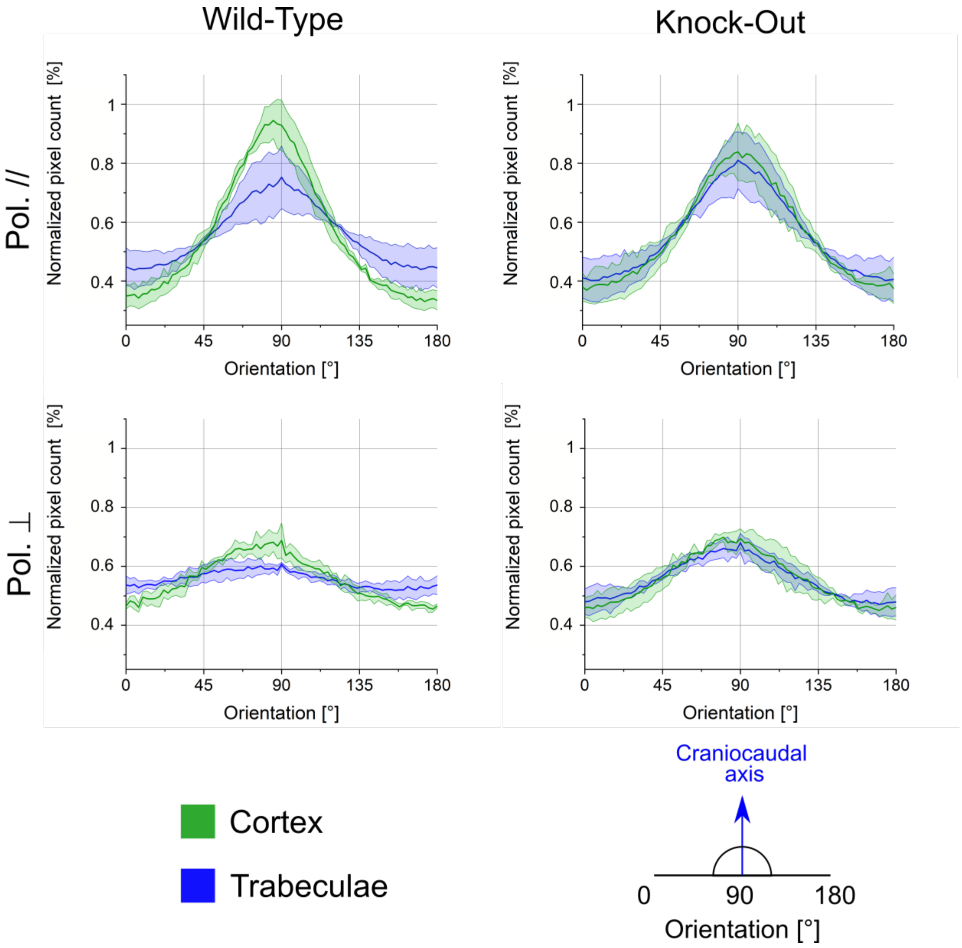

**Figure 4.18:** *Directionality analysis of collagen fibrils. On the x axis, the possible angles of orientation of the fibrils are displayed. On the $y$-axis, the average fraction of fibrils oriented at the corresponding angle ($x$-axis) is reported. The mean plot is displayed in solid line, the confidence interval at $90\%$ is shown as a shaded light area. In green are reported data obtained in cortical regions, in blue data obtained in trabecular regions.*

of the 75 bins represents the normalized pixels count in a range of 2.4°. For example, a portion of collagen fibrils oriented along the craniocaudal axis of the murine spine yields values in general nearby 90°. The confidence interval, displayed as a shaded area, is estimated with a confidence level of $90\%$.

The most of collagen fibrils are orientated at roughly $90\%$, regardless of where they are collected, confirming the findings of the preceding section. Trabeculae and cortex both contribute to bone's mechanical strength by supplying toughness and elasticity, primarily in the direction of load-bearing articulation, which is 90°, for as we have defined the reference system. The orientation is more pronounced when using the parallel-polarized pump field: collagen fibrils exhibit a preferential 90° organization along the craniocaudal axis of the spine, but the perpendicular-polarized pump beam enhances the signal emitted by transversely oriented collagen fibrils. This translates into weaker peaks at 90° and a more dispersed outline for data collected with perpendicular-polarized pump beam, as displayed in Fig. 4.18, panel c and d, with respect to data plotted in panel a and b. Another interesting observation is that the fibril orientation curves in cortex and trabeculae show significant differences in WT samples, while they are practically overlapping in KO samples. This result suggests that, in the WT model, the cortical region displays a higher grade of orientation of its collagen fibrils, making it distinguishable from the trabecular region (Fig. 4.18, panel a and c). Conversely, these results are not found in the KO model (Fig. 4.18, panel b and d).

To analyze more rigorously the graphs presented in Fig. 4.18, we decided to fit them with a function $f$ that was the sum of a baseline (B) and a Gaussian, defined as:

$$f = B + Ae^{-(\frac{\theta-\theta_0}{\sqrt{2}\sigma})^2}, \tag{4.4}$$

where $B$ represents the baseline, that is the portion of collagen fibrils evenly distributed in all orientations, $A$ is the peak-baseline amplitude of the gaussian bump, $\theta_0$ is the central orientation of the curve and $\sqrt{2}\sigma$ measures the width of the curve, as it is the inflection points of the gaussian fit. As an example, Fig. 4.19 shows the fit obtained with the data acquired from cortical areas of WT samples, with pump beam parallel-polarized to the craniocaudal axis.

Not all parameters present in function $f$ are free parameters. In fact, once the values of $A$, $\theta_0$ and $\sigma$ that properly describe the Gaussian bump have been found, the value of the baseline can be obtained directly: the sum of the area underlying the Gaussian curve and the area of the rectangle of

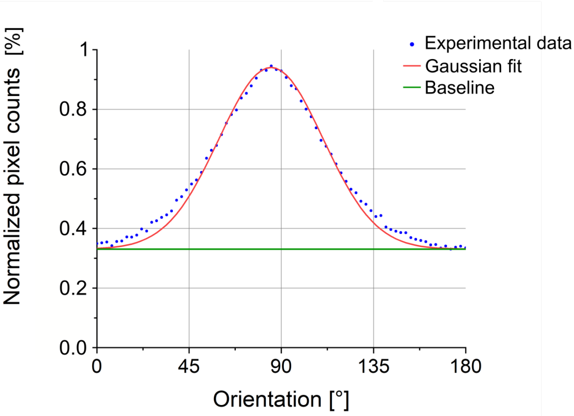

**Figure 4.19:** *Example of the $f$ function fit with data obtained from the cortical regions of WT samples illuminated with parallel-polarized pump beam.*

***Pol. //***

| | WT | | KO | |
|---|---|---|---|---|
| | **Cortex** | **Trabeculae** | **Cortex** | **Trabeculae** |
| **A [%]** | 0.6 | 0.3 | 0.46 | 0.39 |
| $\theta_0$ **[°]** | 85 | 89 | 91 | 91 |
| $\sigma$ **[°]** | 25.45 | 27.58 | 28.99 | 28.28 |
| $\mathbf{R}^2$ | 0.9926 | 0.9921 | 0.9963 | 0.9978 |
| **B [%]** | 0.33 | 0.44 | 0.37 | 0.4 |
| $A_G/A_B$ | 0.65 | 0.26 | 0.50 | 0.38 |

**Table 4.2:** *Optimal parameter values that maximize the $R^2$ of the fit for data collected with pump beam parallel-polarized to the craniocaudal axis of the spine.*

height corresponding to the baseline must be equal to 1, since the integral of the function $f$ between 0 and 180 degrees must be equal to 1. The results obtained, *i.e.* the values of free parameters $A$, $\theta_0$ and $\sigma$ that maximize the $R^2$ value of the fit, are reported in Table 4.2 for images acquired with parallel-polarized pump field, and in Table 4.3 for images acquired with perpendicular-polarized pump field. We reported also the value of $B$ and the $A_G/A_B$ ratio, with $A_G$ area underlying the Gaussian curve and $A_B$ area underlying the baseline, as it is an indicator of the degree of orientation of the collagen fibrils.

Considering the values presented in tables 4.2 and 4.3, the baseline value $B$ is averagely higher in case of perpendicular polarization of the pump beam than in parallel polarization. Indeed, by calculating the average of the baseline values obtained, 0.475 and 0.385, respectively for per-

***Pol.*** $\perp$

| | WT | | KO | |
|---|---|---|---|---|
| | **Cortex** | **Trabeculae** | **Cortex** | **Trabeculae** |
| **A [%]** | 0.214 | 0.077 | 0.24 | 0.186 |
| $\theta_0$ [°] | 79 | 73 | 85 | 83 |
| $\sigma$ [°] | 34.65 | 35.35 | 31.11 | 33.23 |
| **R**$^2$ | 0.9857 | 0.9537 | 0.9914 | 0.9921 |
| **B [%]** | 0.46 | 0.52 | 0.45 | 0.47 |
| $A_G/A_B$ | 0.22 | 0.07 | 0.23 | 0.18 |

**Table 4.3:** *Optimal parameter values that maximize the* $R^2$ *of the fit for data collected with pump beam perpendicular-polarized to the craniocaudal axis of the spine.*

pendicular and parallel polarization, we found an increase of the baseline of $\approx$23%. Moreover, the parameter $\sigma$ is also on average higher in the case of perpendicular polarization of the pump. Acting in the same way as for parameter $B$, we obtained average values of 33.59 for perpendicular polarization and 27.58 for parallel polarization, which means an increase of the $\sigma$ average value of $\approx$22%. An increase in baseline value means an increase in the percentage of randomly oriented collagen fibrils in all directions, so a high baseline value is related to a low degree of fibrils organization. Similarly, since the parameter $\sigma$ is indicative of the width of the Gaussian bell, a high value of $\sigma$ is also related to a low degree of ordering of fibrils. On the contrary, a low value indicates the existence of a preferential direction of orientation of fibrils.

Finally, the values of the ratios $A_G/A_B$ appear higher in the case of the parallel-polarized pump, consistent with the fact that that is the preferred direction of orientation of collagen fibrils. Furthermore, going to calculate the ratio cortex/trabeculae of these values for each sample type and pump polarization, we obtained 2.50 and 3.10 for WT samples, for Pol. // and Pol. $\perp$ respectively, while 1.31 and 1.27 for KO sample, again for Pol. // and Pol. $\perp$ respectively. This result represents a quantification of the higher degree of orientation shown in cortical areas of WT samples compared to trabecular areas, making the two regions effectively distinguishable. This difference is much less marked in the KO samples and, in fact, the curves of the orientations of the collagen fibrils in the cortical and trabecular regions are about overlapping.

In conclusion, in WT sample, the cortical and the trabecular regions present some differences in terms of orientation of their collagen fibrils, due to the diverse specialization of the two bone tissues: in fact, the cortical region is the main responsible for the vertebrae mechanical strength and load bearing. Due to genetic modification, KO models do not feature highly oriented cortical collagen fibrils along the craniocaudal direction, thus their mechanical strength is lower than WT models. Such results are in line with the condition of bone loss induced in KO models.

### 4.2.4 Lipids and proteins distribution

SRS microscopy images at 2850 cm$^{-1}$ and 2920 cm$^{-1}$ reveal the lipid and protein distributions in the WT and KO mouse model. To assess the different distribution and possible accumulations of protein and lipids in bone tissue (cortex and trabeculae) compared to bone marrow, the average signal intensity in the two areas has been calculated pixelwise along with their statistical variances. Then, the ratio of the two average signal intensities has been calculated and the total variance is estimated. The same operations were repeated both for the three KO model samples and for the three WT model samples. The results reported in Fig. 4.20 have been obtained from only 2 samples out of 3, since one sample in both groups showed completely unreliable results. From these graphs it is deduced that in the WT model the distribution of proteins and lipids between mineralized areas and bone marrow is perfectly comparable. On the contrary, in the KO model the lipid signal is much greater in the mineralized regions than in the bone marrow, while the protein content appears homogeneously distributed in the vertebra. This particular observation may stem from a metabolic alteration and prompted our biologist colleagues at Humanitas to look into the matter further. Their test on the expression pattern of genes related to lipid metabolism in washed bone of mice DPP3 KO confirmed this hypothesis.

From these graphs it is deduced that in the WT model the distribution of proteins and lipids between mineralized areas and bone marrow is perfectly comparable. On the contrary, in the KO model the lipid signal is much greater in the mineralized regions than in the bone marrow, while the protein content appears homogeneously distributed in the vertebra. This particular observation may stem from a metabolic alteration and prompted our biologist colleagues at Humanitas to look into the matter further. Their test on the expression pattern of genes related to lipid metabolism in washed bone of mice DPP3 KO confirmed this hypothesis.

## 4.3 Conclusions

Thanks to our technology, it was possible to recreate morphological and biochemical maps of mouse spine tissues spanning millimeter-wide FOVs

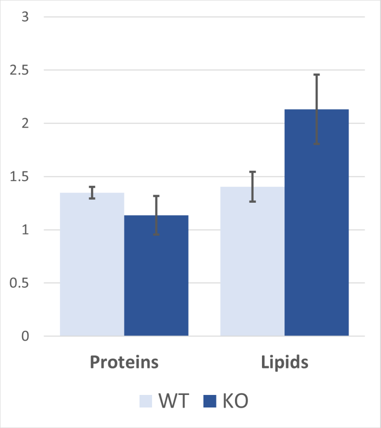

**Figure 4.20:** *Comparison of the ratio between the average signal intensity in the bone tissue and in the bone marrow for proteins and lipids in WT and KO models. Mean values ± SEM.*

with multimodal imaging acquisitions. The results obtained in SHG modality provided evidence for the existence of a relationship between the suppression of the DPP3 gene in mice and the expression and organization of fibrillar collagen in lumbar spine sample. Furthermore, this method yields an innovative, fast and effective means to distinguish pathology-bearing mice from healthy ones exploiting the properties of SHG imaging and simple image processing methods coupled with statistical tools. In SRS modality, a difference in the distribution of lipid content between the two sample groups, WT and KO, was evidenced and it was related to a metabolic change, subsequently confirmed by standard biological techniques.

In conclusion, VIBRA microsope led us to highlight differences between the two set of samples not previously appreciated by standard analysis, thus demonstrating the potential of multimodal NLO microscopy for the characterization of bone specimens. Moreover, this technique could be translated to the clinics and be a useful new diagnostic tool for detecting bone diseases that cause alteration in the expression and organization of collagen fibrils in human bone tissues.

CHAPTER 5

# Adaptive Optics

This chapter presents the work done in collaboration with the Neurophotonics group of Universitá degli Studi di Modena e Reggio Emilia. Through this collaboration, I was able to uncover the huge potential of adaptive optics applied to nonlinear imaging methods and I had the chance to broaden my knowledge of biological samples.

## Introduction

As already highlighted in this thesis, optical microscopes are fundamental instruments in a wide range of scientific domains. High-quality optical systems are required to achieve optimal resolution, but even with flawless optical components, the performance of the microscope is influenced by variations in the optical characteristics of the specimen under observation. As depicted in Fig. 5.1, when light travels through a specimen with spatial changes in refractive index, aberrations are introduced. Optical aberration are deviations from the ideal wavefront which, spreading light out over some region of space rather than focusing to a point, lead to reduced resolution or power efficiency of the optical system [85]. As a result, resolution and contrast of microscope images are significantly reduced. In order to get over this limitation and to correct specimen-induced aberration, adaptive optics (AO) was introduced, which have been shown to successfully correct optical aberrations induced by both sample and optical system [12]. In particular, the improvements brought by the use of this technology have been crucial for deep brain microscopy applications [137].

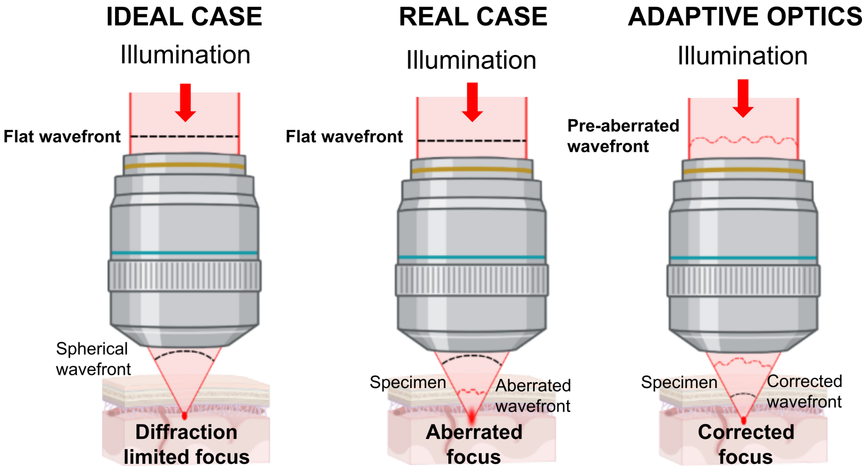

**Figure 5.1:** *Schematic representation of focusing by a high-NA objective lens. In an ideal case flat wavefront in the pupil is converted into convergent spherical wavefront leading to a perfect diffraction limited focus. In a real case focusing through a complex specimen with refractive index variations introduces aberrations, so the flat wavefront in the pupil is distorted and it is converted in an aberrated focus. With adaptive optics it is possible to introduce a conjugate phase in the objective pupil and correct the specimen-induced aberrations, recovering a diffraction limited focus.*

Adaptive optics systems can be classified into two cathegories: wavefront sensor based systems [24] and sensorless systems [11]. In the first case, the wavefront sensor provides the great advantage of quickly measuring the aberration to be corrected. Unfortunately this advantage is accompanied by many drawbacks, including technological complexity, the lack of brilliant point-like sources within bio-samples, and the correction's validity over a small field of view. These drawbacks lead to sensorless adaptive optics being often selected in situations where the simplicity of installation and greater fields of view take precedence over the speed with which the correction is made.

In sensorless systems, aberration correction is based on optimization of an image quality metric (such as intensity), so that it is maximum or minimum when the aberration is completely compensated. The aberration $\Phi$ can be described as a linear combination of $N$ elements of an orthogonal base:

$$\Phi = \sum_{i=1}^{N} a_i \phi_i, \tag{5.1}$$

so that the aberration $\Phi$ is entirely defined by the vector of coefficients $\boldsymbol{a} = \{a_1, ..., a_n\}$ [168]. The choice of the base $B = \{\phi_1, ..., \phi_N\}$ to use depends on the application: the Zernike polynomials [180] or the influence functions of the actuators of a deformable mirrors are frequently used. In order to determine the set of coefficients for $\boldsymbol{a}$ maximizing the metric, a number of optimization techniques may be used, including hill-climbing algorithms [18], model-based approaches [139], nonlinear optimizations [140], and neural networks [150]. Even if the optimization can be performed with any base, the selection of the aberration base B turns out to be a critical factor to achieve a good result. As demonstrated by previous research [13, 139], the use of gradient orthogonal bases, such as Lukosz Polynomials, guarantees various positive effects. In particular, these bases ensure that during the optimization process the geometric centre of the point spread function (PSF) of the system remains spatially unchanged, and consequently that the optimized image field of view is not displaced with respect to the field of view initially chosen.

Among the many definitions that could be given to the geometric center of the PSF, we have chosen to use the PSF intensity distribution $PSF(x, y, z)$ and the center of mass $(COM)$ at a given axial depth $z$, defined as:

$$COM_x(z) = \sum_{x,y} (x * PSF(x, y, z)) \,/ \sum_{x,y} (PSF(x, y, z)) \tag{5.2}$$

$$COM_y(z) = \sum_{x,y} (y * PSF(x, y, z)) \,/ \sum_{x,y} (PSF(x, y, z))\,. \tag{5.3}$$

Then, we define the axial position of the center $C_z$ of the PSF as the coordinate for which the second moment $SM(z)$ of $PSF(x, y, z)$ is minimum:

$$C_z = min_z SM(PSF, z) \tag{5.4}$$

with

$$SM(PSF, z) = \frac{\sum_{x,y} \left( PSF(x, y, z) * \left[ (x - COM_x(z))^2 + (y - COM_y(z))^2 \right] \right)}{\sum_{x,y} (PSF(x, y, z))}. \tag{5.5}$$

Finally, the lateral coordinates of the PSF center as the center of mass in the $C_z$ axial plane can be defined as:

$$C_x = COM_x(C_z),\ C_y = COM_y(C_z). \tag{5.6}$$

Corrections based on a gradient orthogonal base may be analytically demonstrated to be shift-less for imaging systems that use linear imaging techniques [190], where the PSF is actually represented by the intensity distribution at the system's focus plane. Fig. 5.2 reports simulation of point spread function in both lateral and axial planes, for Zernike and Lukosz polynomials describing coma-like and spherical-like aberrations for linear and quadratic imaging methods. This simulation clearly show that the invariance of the PSF center is not verified for two-photon microscopy, or any other approach with a nonlinear dependence between the PSF and the intensity of the excitation light, such as SHG/THG microscopy, CRS microscopy or three-photon fluorescence microscopy [100, 127].

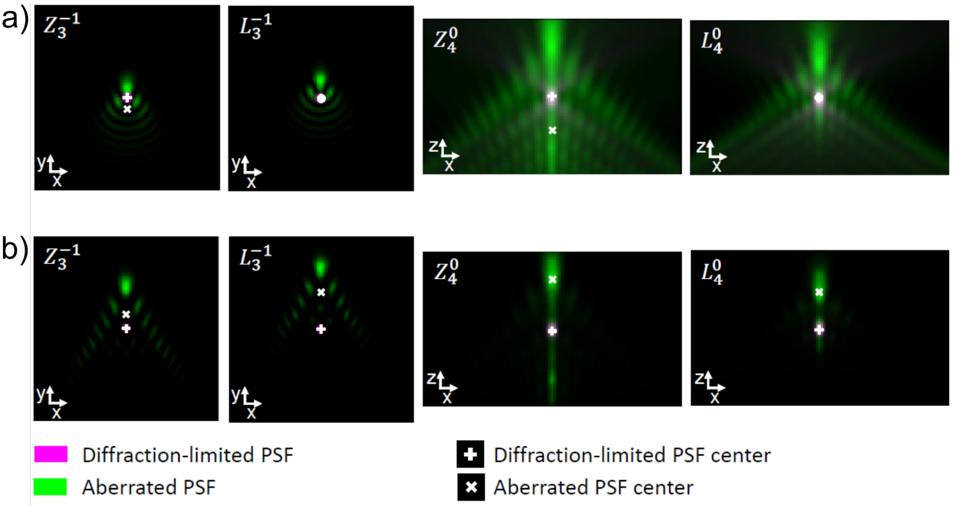

**Figure 5.2:** *Simulation of point spread function in both lateral and axial planes, for Zernike and Lukosz polynomials describing coma-like and spherical-like aberrations. Aberrations are simulated for a) linear imaging methods and b) quadratic imaging methods (e.g. two-photon microscopy, second harmonic generation imaging). It should be noticed how, for linear PSFs, Lukosz polynomial aberrations produce no shift in the centre of the PSF as defined in equations 5.2, 5.3 and 5.4, due to the gradient orthogonal nature of the base. This does not hold true for nonlinear imaging, as reported in panel b. Reprinted with permission from [168] ®Optica Publishing Group.*

Even though modest changes in the field of vision are often deemed insignificant, using a not gradient orthogonal aberration base may cause considerable issues during optimization. In fact, a significant amount of aberrations may be introduced when signal optimization is performed on a focal plane with weak fluorescent features with brighter objects contained in the planes immediately above or below. This situation can lead to a shift of the image′s field of view towards the brighter features rather than correcting the aberration on the plane of interest. In addition, a space-varying correction performed on little subregions of the field of view may considerably enhance imaging result on large fields of view, as demonstrated by several recent studies [3, 101, 130, 138, 145]. Indeed, to prevent substantial artifacts when combining the subregion images into a single output image, a shift-less correction base is crucial for these applications.

Here we present a calibration method for the determination of a shift-less correction base for adaptive optics in nonlinear microscopy setups. Although the calibration was carried out using a bespoke setup for two-photon adaptive optics imaging, any multiphoton microscope can be easily adapted, adding an adaptive optical element for aberration correction. To demonstrate the shift-less nature of calibrated base, imaging experiments were carried out on a synthetic sample of fluorescent microspheres, and on the barrel cortex of an anesthetized mouse.

## 5.1 Materials and Methods

### 5.1.1 Sample preparation

Two different samples were employed in this study. The first is a thick synthetic sample consisting of fluorescent microspheres of $\approx$ 200 nm in diameter, embedded in a $10\% \, w/v$ agarose gel. The second is an anesthetized female six months old C57BL/6 mouse. An optically clear permanent cranial window was surgically opened on the mouse head. In addition, during surgery, 2 $\mu L$ of a 10 $\mu M$ solution of sRhoVR1-GP1 [93], a synthetic fluorophores, in ACSF was injected in the mouse brain. For additional information you can refer to [168]. All animal procedures were performed according to the guidelines established by the Italian Council on Animal Care, and were approved by Italian Government Decree No. 947/2017-PR. Every effort was made to minimise the number of mice used, and their suffering.

### 5.1.2 Experimental setup

The custom-built nonlinear optical microscope used in this experiment is powered by a titanium-sapphire laser (Chameleon Ultra II, Coherent), a tunable ultrashort pulsed laser source, working in the range 680-1080 nm, with a pulse duration of 140 fs and a 80 MHz of repetition rate. First, the laser beam is expanded to a diameter of 12 mm (1/e$^2$ value), then it is directed to a spatial light modulator (SLM) (Meadowlark, USA) with a refresh rate of 31 Hz, 1152×1920 pixels and a pixel pitch of 9.2 $\mu$m. The SLM is the adaptive optical element of the setup: it is used to modify the phase of the impinging laser beam in order to compensate for the aberrations introduced by the system and the specimen. Then, a couple of lenses (AC-508-200-B and AC-508-150-B, Thorlabs) in 4-f configuration conjugates the SLM with the plane between two galvanometric mirrors (GVS-012/M, Thorlabs, USA), which is in turn conjugated to the back aperture of the objective (XLUMPlanFL N, 20X, 1.0 NA, Olympus, Japan) by another pair of lenses (AC-508-180-AB and AC-508-400-AB, Thorlabs, USA), still in 4-f configuration. A physical point blocker is placed in the focal plane of the first lens to stop the SLM's zeroth diffraction order. Being this microscope suitable for in vivo imaging, the TPEF signal generated in the sample is collected in backward direction, so an epi-detection scheme is employed. The nonlinear signal is isolated from the excitation light with a long-pass dichroic mirror (FF665-Di02-25x36, Semrock, USA), mounted between the SLM and the galvanometric mirrors, in a descanned optical path. TPEF signal, filtered again with two other filtres, a short-pass filter (FF01-680/SP-25, Semrock, USA) and a suitable bandpass filter, is finally gathered on an EMCCD camera (Hnu 128 AO, Nuvu, Canada) via an adjustable magnification lens (12-72 mm, 1.2 f #, Cosina, Sony, Japan). The experimental setup is schematically represented in Fig. 5.3.

### 5.1.3 Shift-less correction base determination

In order to define a shift-less correction base we decided to start from the Zernike polynomials base $Z_{n,m}$ [106]. This choice can be justified by simulating the displacement of the PSF. In fact, as shown in Fig. 5.4, the only terms that introduce shifts are coma-like polynomials and radial polynomials. Considering the standard notation $Z_{n,m}$, the coma-like polynomials are those with $n$ coefficient odd and $m = \pm 1$ and move the center of the PSF laterally, while the radial polynomials have $n$ coefficient even and $m = 0$ and shift the center of the PSF axially. This feature is crucial for our work, since it enables us to write a shift-less base $S$ of polynomials $s_{n,m}$ as:

$$S_{n,m} = \begin{cases} Z_{n,m} - s_{n,m} Z_{1,-1}, & \text{if } n \text{ is odd and } m = -1 \\ Z_{n,m} - s_{n,m} Z_{1,1}, & \text{if } n \text{ is odd and } m = 1 \\ Z_{n,m} - s_{n,m} Z_{2,0}, & \text{if } n \text{ is even and } m = 0 \\ Z_{n,m}, & \text{otherwise.} \end{cases} \tag{5.7}$$

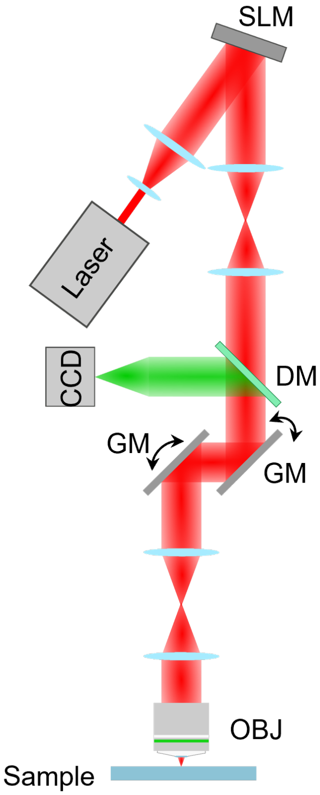

**Figure 5.3:** *Schematic representation of the experimental setup, not to scale. SLM, spatial light modulator; DM, dichroic mirror; GM, galvanometric mirror; OBJ, objective; CCD, detector. Adapted with permission from [168] ®Optica Publishing Group.*

$Z_{1,1}$, $Z_{1,-1}$ and $Z_{2,0}$ are the Tip, Tilt and Defocus Zernike polynomials, respectively and represent aberrations that have as their only effect to move the PSF along the three main axes ($x$, $y$ and $z$), with no change in its intensity. Ideally, the coefficients $s_{n,m}$ to be used to compensate for shifts along the main axes introduced by coma-like polynomials and astigmatism-like polynomials can be calculated directly from simulations. Actually, the simulations fail to take into account that we are working with a real experimental setup. Indeed, the unavoidable tiny misalignments of the optics and the actual numerical aperture of the system have a not negligible impact on the coefficients, thereby preventing simulated bases from being shift-less in experimental situations. It is therefore necessary to empirically determine the correct coefficients $s_{n,m}$: to do so, we used a test sample, a fluorescent solid slide (FSK3, Thorlabs), selecting a focal plane within the slide at about 200

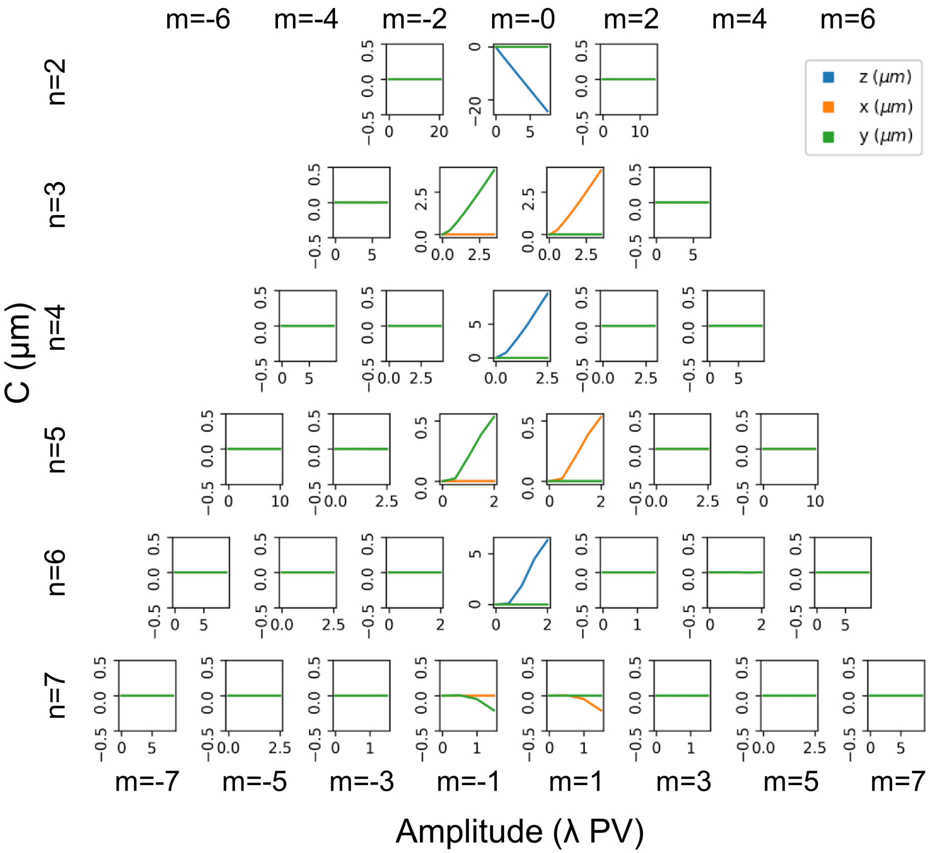

**Figure 5.4:** *Simulation of displacement of the PSF center as defined in Eq. (5.4) and Eq. (5.6). Blue lines represent axial displacement, green and orange lines represent lateral displacement. Adapted with permission from [168] ®Optica Publishing Group.*

$\mu$m depth. First, a set of TPEF images were taken at a fixed excitation focus, with linearly varying quantities of defocus aberration added to each image, and the second moment of the intensity distribution (Eq. (5.5)) was measured for each image. By quadratically interpolating the obtained second moment values, we can derive the value of defocus that minimizes the second moment of the intensity distribution. All subsequent measurements were taken using this value as a defocus offset. Having said that, we can go on to explain the procedure for determining the coefficients $s_{n,m}$.

Let′s start by considering horizontal coma-like polynomials and their coefficients $s_{n,1}$ with odd $n$: introducing in the system aberrations in the form:

$$\Phi = aZ_{n,1} + bZ_{1,1} \tag{5.8}$$

we go to measure the displacement of the center of mass of the PSF intensity distribution from the initial position, as a function of linearly increasing parameters $a$ and $b$. The results obtained with this procedure are shown in Fig. 5.5a. Each tested value of parameter $a$ has been represented with a different color, while the values of parameter $b$ are used as x-axis. In order to find its minimum value, each curve obtained for each value of $a$ has been filtered with a Savitzky-Golay filter and interpolated with a polynomial. The slope of the fitted line that passes through all minima is used to compute the value of the $s_{n,1}$ coefficient. In other words, what we are doing is finding out how much Tip aberration needs to be added to compensate for the shift introduced by the n-th coma-like polynomial. The same procedure was repeated to determine the coefficient $s_{n,-1}$ with odd $n$ of vertical coma-like polynomials.

By moving to radial polynomials, the coefficients of these polynomials, $s_{n,0}$ with even $n$, have been determined using a procedure that is analogous to the one that has just been explained. The only differences are in the aberrations that were introduced into the system, this time in the form:

$$\Phi = aZ_{n,0} + bZ_{2,0}, \tag{5.9}$$

and the metric that was used to calibrate the coefficient, no longer the PSF displacement but the second moment of the intensity distribution, as defined in Eq. (5.5). The result for the calibration of $S_{4,0}$ is reported in Fig. 5.5b. The base was calibrated in this way up to the sixth aberration order.

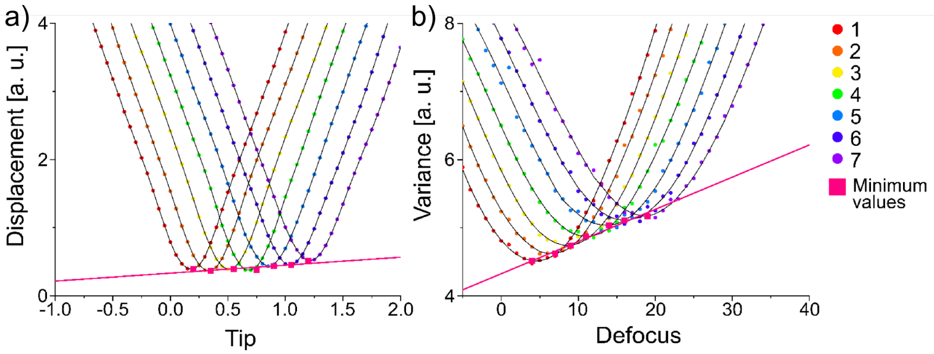

**Figure 5.5:** *a) Dataset for the calibration of $S_{3,-1}$. b) Dataset for the calibration of $S_{4,0}$. Adapted with permission from [168] ® Optica Publishing Group.*

### 5.1.4 Sensorless correction method

The base calibrated as explained in the previous subsection (5.1.3) was tested on two different samples, a synthetic sample of fluorescent particles in agarose gel and the barrel cortex of an anesthetized mouse, to assess its shift-less feature and compare it with the standard Zernike base. All elements of the base were optimized, with the exception of Piston, Tip, Tilt and Defocus, with a sensorless approach. Since the goal of this experiment was not to get a short convergence time or optimal corrections performance, we decided to use a simple hill-climb algorithm for the optimization. As an optimization metric, we chose to use the mean intensity of the two-photon fluorescence signal, generated by scanning the laser in a spiral pattern over the sample with a period corresponding to the camera exposure. The aberration amplitude was linearly modulated for each of the terms in the optimization base, with the intensity metric being measured at each step of the modulation. A Savitzky-Golay filter was used to filter the metric function before it was interpolated. The correction coefficient was determined as the peak-to-valley polynomial amplitude maximizing the metric value.

## 5.2 Results and Discussion

For each sample used, the results are presented by comparing three distinct three dimensional datasets, acquired in 3 different ways: the first was acquired without applying any aberration correction, the second was acquired using the Zernike polynomials as correction base, and the third was acquired using the shift-less base calibrated as described in Subsection 5.1.3. The acquisition experimental protocol of the three datasets foresaw to acquire first the dataset without correction, then the one with the Zernike correction base, and then the one corrected with the calibrated shift-less base. In the end a fourth control dataset was acquired without aberration correction, to ensure that no motion artifacts occurred during the experiment and to guarantee a fair and reliable comparison.

Let′s start considering the results obtained on the synthetic sample, fluorescent microspheres in agarose gel. The datasets were acquired inside the sample, at a depth of 500 $\mu$m (considering the center of the z-stack), and the main aberration introduced by the sample is spherical, as a consequence of the mismatch between refractive indices. Two datasets, the uncorrected one and the one corrected applying the shift-less base, were acquired on a field of view of $20\times20\times10$ $\mu$m$^3$, instead the dataset corrected with the Zernike base was acquired on a field of view of $20\times20\times20$ $\mu$m$^3$. The extension of the acquisition in the radial direction was made to clearly assess the radial shift introduced by the correction of aberrations with the Zernike base. The size of the voxels acquired was the same in all three datasets and is $200\times200\times500$ nm$^3$. In Fig. 5.6 the first row reports images of the plane at the axial center of each dataset. It is clear that, in contrast to using a shift-less base, which just raises the image's average intensity, aberration correction using the Zernike base drastically alters the details in the image owing to the imaging plane's axial shift. By searching within the corrected datasets the planes with the best correlation with the central plane of the uncorrected dataset, in the case of the correction with the shift-less base we have to move down by 1 $\mu$m from the dataset's axial center, while for the Zernike base of 4 $\mu$m upwards, as shown in the second row of Fig. 5.6.

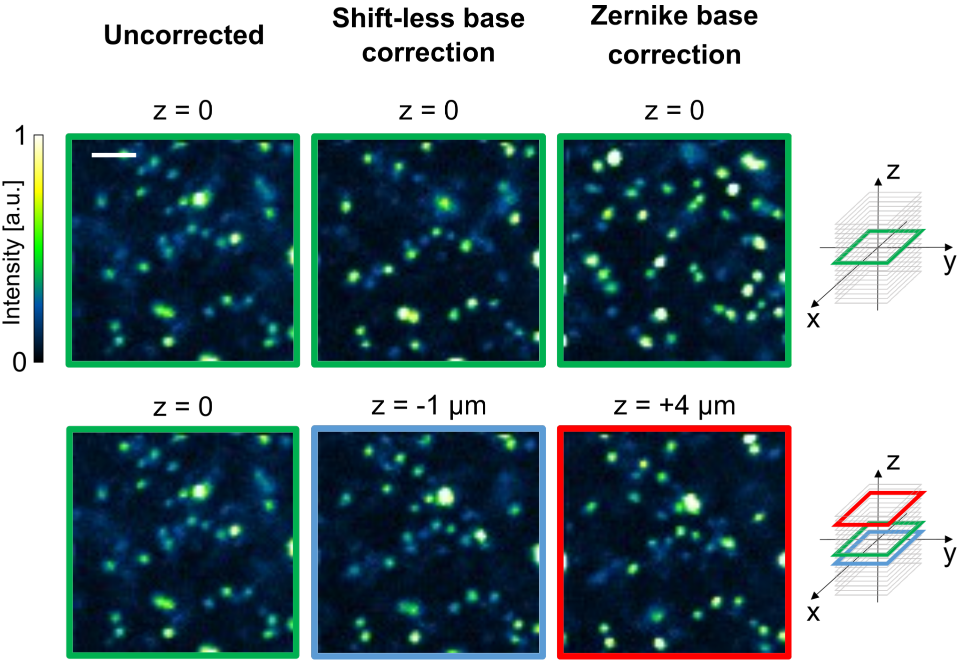

**Figure 5.6:** *Results obtained with fluorescent microspheres sample: in the first row uncorrected, shift-less corrected and Zernike corrected images of the datasets' axial center are presented. In the second row, images of the planes with best correlation with the uncorrected dataset's axial center. On the right there is a schematic representation of the datasets in the reference system, with the reported images highlighted in the z-stack according to the color code of their contour. Scale bar is 3 $\mu$m. Adapted with permission from [168] ®Optica Publishing Group.*

Furthermore, considering the image with highest correlation of the Zernike-corrected dataset, a considerable lateral shift of $\approx$ 1 $\mu$m between the two pictures, the uncorrected and the Zernike-corrected one, can be noticed. This lateral displacement is compensated when using the shift-less base, as this presented a tip-tilt component of 1.2 $\lambda$ peak-to-valley, which is equivalent to $\approx 1\ \mu$m in the focal plane for our experimental setup.

Fig. 5.7 depicts an $xz$-section from the three datasets. The correction performed with the shift-less base acts effectively on the slight spherical aberration, in fact the fluorescent microspheres appear brighter and shorter in the axial direction. In contrast, the correction performed with the Zernike base not only considerably distorted the PSF, making the microspheres appear completely deformed, but also dramatically moved the imaging plane.

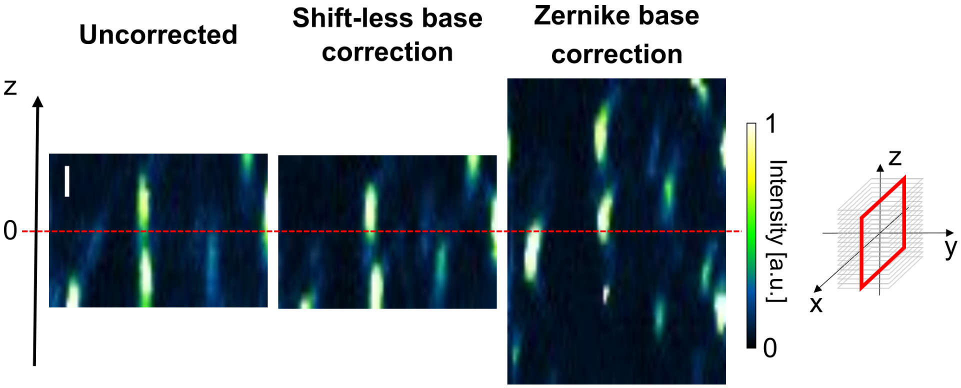

**Figure 5.7:** *$xz$-section from the three datasets: the red dashed line represents the datasets' axial center. Scale bar is 1 $\mu$m. Adapted with permission from [168] ®Optica Publishing Group.*

Then we decided to focus our attention on a single microspheres. In Fig. 5.8 we reported the maximum intensity projections of the same microsphere in the three datasets: in the first row in the transverse plane ($xy$-plane) and in the second row in the frontal ($xz$-plane) and sagittal ($yz$-plane) plane. The, we estimated the lateral resolution of each dataset measuring the FWHM of the microsphere intensity. For the uncorrected dataset we obtained a resolution of 710 $\pm$ 2 nm, correcting the aberrations using the Zernike base a resolution of 600 $\pm$ 2 nm, and using the shift-less base for correction the resolution still improves, reaching a value of 540 $\pm$ 2 nm. Finally, we presented in Fig. 5.9 the phase patterns obtained after imaging optimization, using the shift-less base as correction base and using the Zernike base.

Now to the results obtained in-vivo in an anesthetized mouse (Fig. 5.10), certainly a more interesting experimental scenario for applications

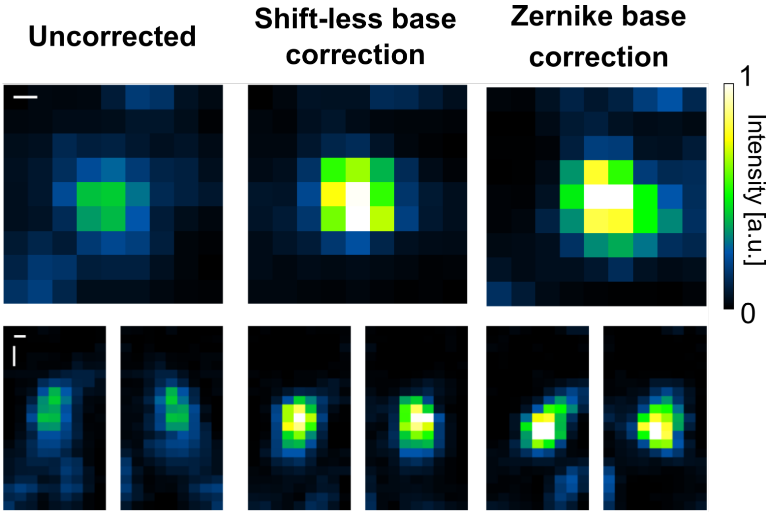

**Figure 5.8:** *Maximum intensity projections of a sub-diffraction object in the field of view. In the first row the projections in $xy$ plane is reported. In the second row, $xz$ and $yz$ projections are reported. Horizontal scale bars are 200 nm, vertical scale bar is 500 nm. Adapted with permission from [168] ®Optica Publishing Group.*

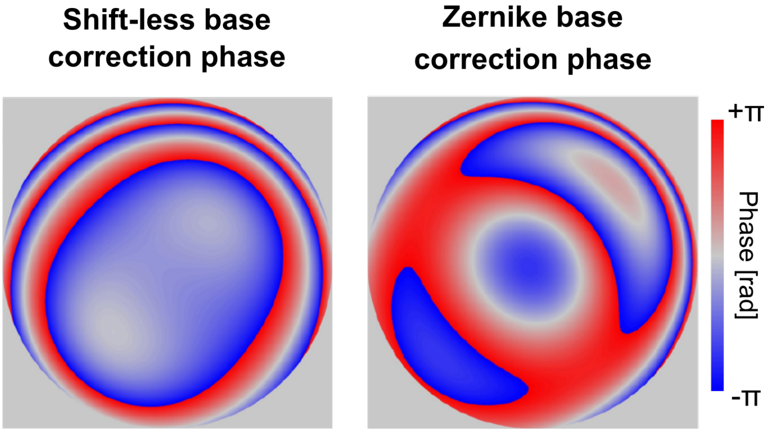

**Figure 5.9:** *Phase correction after optimization with the shift-less base and with the Zernike base in fluorescent microspheres experiment. Adapted with permission from [168] ®Optica Publishing Group.*

of adaptive optics in nonlinear microscopy. Working in-vivo, for ethical issues it was necessary to minimize the acquisition time of datasets, so we decided to reduce sampling a bit and acquire voxels of $1{\times}1{\times}1\ \mu\text{m}^3$. This time, datasets were acquired over a field of view of $200{\times}200{\times}50\ \mu\text{m}^3$.

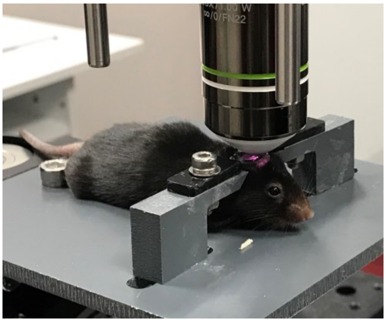

**Figure 5.10:** *In-vivo experiment: the mouse is positioned under the microscope and kept anesthetized with 2,2,2-tribromoethanol for 1 hour.*

Similarly to the experiment on the synthetic sample, in Fig. 5.11 we reported the images of the plane at the axial center of each dataset, the uncorrected one, the shift-less corrected one and the Zernike-corrected one. Also this time, the details shown in the image of the third dataset (Zernike base correction) are completely different from those present in the other two images. Small motion artifacts are inevitable in this kind of experiment, but when the Zernike base is used for correction, the dataset exhibits noticeable shifts when contrasted to the uncorrected and shift-less corrected datasets.

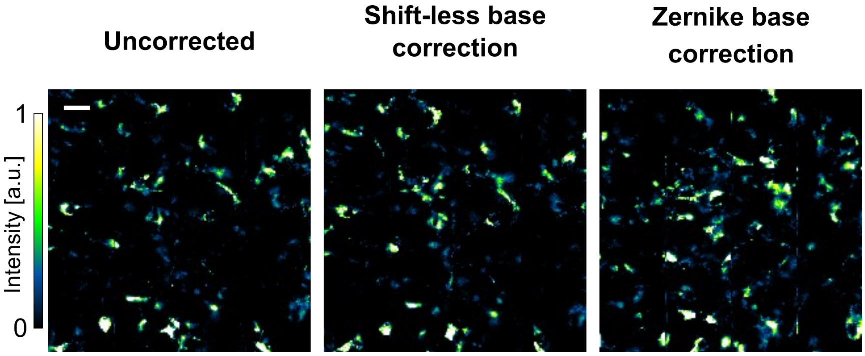

**Figure 5.11:** *Images of fluorescence from sRhoVR-1 injection in the barrel cortex of anesthetized mouse. Two-dimensional images at the focal plane of the microscope in the absence of correction, in the case of correction with the shift-less base, and of correction with the Zernike base. Scale bar is 20 μm. Adapted with permission from [168] ®Optica Publishing Group.*

Referring to the detail highlighted by the red box in Fig. 5.12, we reported the plans of the three datasets with the maximum correlation in the second row. Between uncorrected dataset and shift-less corrected dataset there is perfect correspondence between the central axial planes, instead in the Zernike-corrected dataset we have to move of 6 $\mu$m upward and however there is not perfect correspondence between the observed features. In addition, in the images of the $xz$-plane sections shown in the third row of the figure, it is clearly seen that the use of the shift-less base improves intensity and resolution.

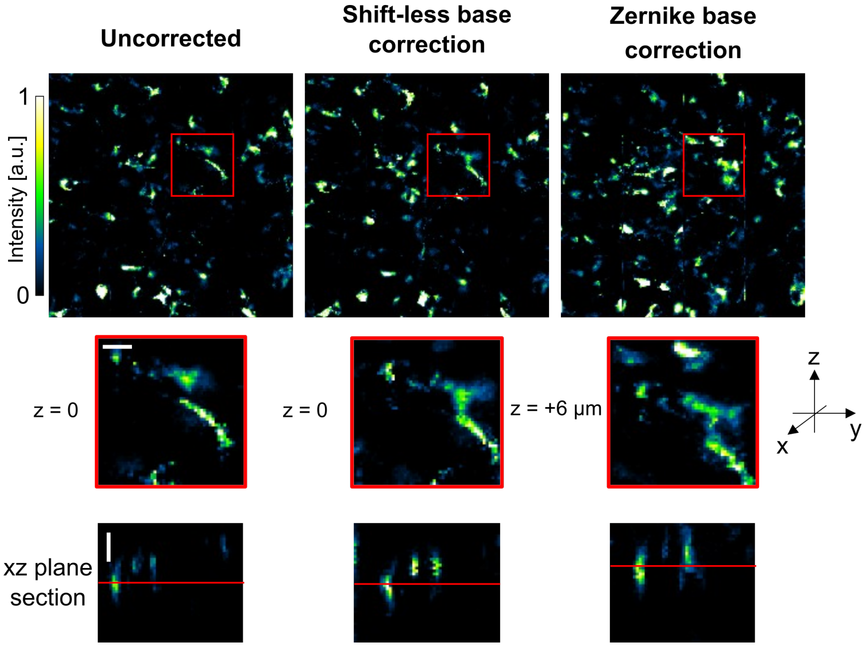

**Figure 5.12:** *Detail from the red highlighted area of images at the axial center of the three datasets. In the second row the images from the three dataset with the highest correlation are reported. In the third row the same section from each dataset on a $xz$-plane. Scale bars are 10 µm. Adapted with permission from [168] ®Optica Publishing Group.*

On the contrary, the dataset corrected with the Zernike base shows a slight worsening of the resolution. In fact, because of the small amount of fluorophores present in the three-dimensional field of vision, the Zernike-correction tends to shift the focus of the image towards more fluorescent details to optimize the intensity metric, sacrificing resolution. An example of this is given in Fig. 5.13. Here we focus on the detail highlighted by the magenta box: similarly to Fig. 5.12, in the second row we reported three planes with maximum correlation, while in the third row is reported the same sagittal section in the three datasets. Observing the sagittal sections it is evident that correcting with the shift-less base the two cell bodies are resolved correctly and are perfectly distinguishable, instead correcting with the Zernike base they appear as a single fluorescent mass.

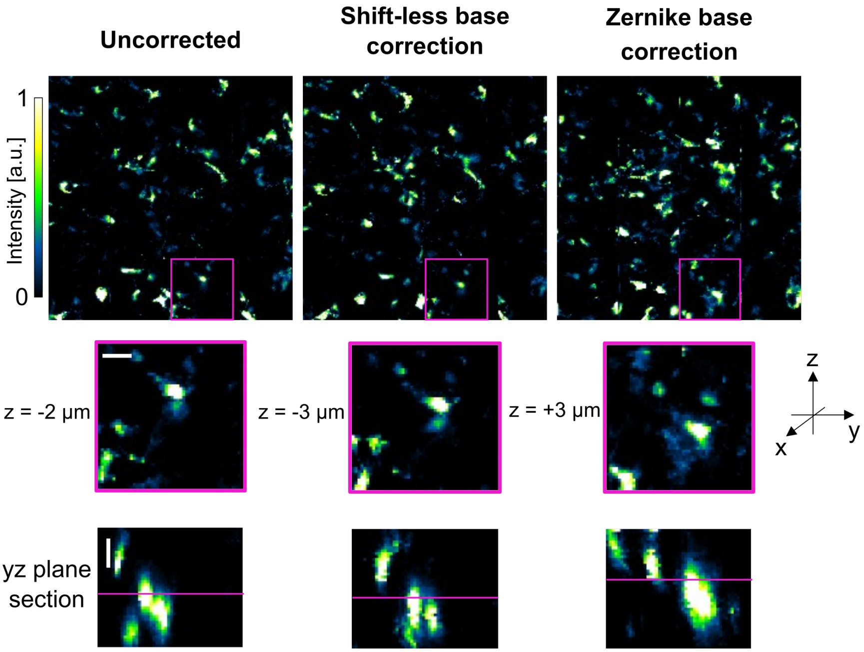

**Figure 5.13:** *Detail from the magenta highlighted area of images at the axial center of the three datasets. In the second row the images from the three dataset with the highest correlation are reported. In the third row the same section from each dataset on a $yz$-plane. Scale bars are 10 $\mu$m. Adapted with permission from [168] ®Optica Publishing Group.*

In conclusion, we presented in Fig. 5.14 the phase patterns obtained after imaging optimization, using the shift-less base as correction base and using the Zernike base in this in-vivo experiment.

## 5.3 Conclusions

In this chapter, a method for calibrating a shift-less aberration base for sensorless adaptive optics in two-photon microscopy has been proposed and validated. To take advantage of the approach presented here, a standard two-photon fluorescence microscope has to be modified into an adaptive microscopy system, however the necessary modifications are extremely

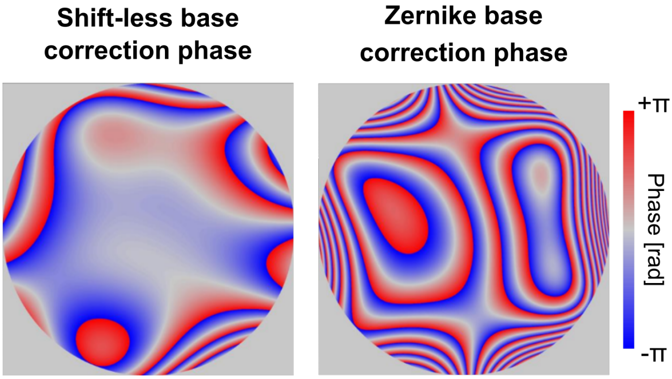

**Figure 5.14:** *Phase correction after optimization with the shift-less base and with the Zernike base in in-vivo experiment. Adapted with permission from [168] ® Optica Publishing Group.*

simple and well within the reach of researchers with experience in nonlinear optical configurations. The results presented in Section 5.2 demonstrated that not always the shifts introduced using Zernike polynomials as correction base are negligible and the images obtained can be seriously compromised. Furthermore, adaptive optics is becoming increasingly used in microscope applications in its anisoplanatic declination, where tiled parts of the field of view are independently corrected. It is possible that applying different Zernike-corrections to each tile results in artifacts in the entire reconstructed image, due to the relative shifts introduced, even when an optimum correction is applied. So, because of the ease with which the calibration process may be implemented and because of the possible advantages associated with its use, we believe we have provided a very valid tool for all sensorless adaptive optics systems for nonlinear microscopy applications.

## CHAPTER 6

# Conclusions and future perspectives

The present thesis is a contribution to the field of multimodal nonlinear optical microscopy applied to biological samples. In the last 3 years I had the opportunity to explore this topic deepening three different aspects: first, the problem of phototoxicity induced in viable cells by NIR ultrashort pulsed laser radiation (Chapter 3); second, the development and optimization of a multimodal microscopy setup and its use to study a complex biological problem such as bone diseases (Chapter 4); third, the improvements that adaptive optics can bring to nonlinear imaging techniques in terms of resolution and depth of penetration (Chapter 5).

In Chapter 3, we studied the survival rate of HeLa cells exposed to NIR laser radiation, following a data-driven approach. We characterized the photodamage mechanisms that come into play, corroborating the presence of photothermal damage with thermodynamics considerations. In addition, we provided useful insights into safe working conditions to many researchers planning experiments involving laser illumination [167].

In Chapter 4, we used the VIBRA multimodal nonlinear microscope on murine spine tissue samples to gather morphological and biochemical information over wide FOVs. By exploiting the characteristics of the different microscopy modalities, we demonstrated the impact of the DPP3 enzyme suppression in collagen expression, in collagen fibrils orientation and in the lipid content distribution, proving the validity and effectiveness of multimodal microscopy as a diagnostic tool for pathologies characterized by bone loss.

In Chapter 5, we proposed an innovative calibration method for shiftless correction base in sensorless adaptive optics microscopy applications. We demonstrated the shiftless feature of such a calibrated base on a synthetic sample and *in-vivo* on mouse brain, obraining improvement in resolution and correction of aberrations [168].

In my opinion, the combination of the findings presented in this thesis could lead to a breakthrough in the field of nonlinear microscopy for biological applications such as the development of a new pioneering and innovative multimodal nonlinear optical microscope, with an adaptive optical element for *in-vivo* biomedical applications. Without any doubt, the true value of nonlinear technologies lies in their label-free and non-invasive nature, which makes them suitable for *in-situ* and *in-vivo* applications and future clinical translation. The application of adaptive optics to multimodal nonlinear microscopy could make this translation closer and more concrete, improving resolution and penetration depth. In particular, although attempts have been made, application of adaptive optics to CRS techniques still has much room for improvement, mainly due to the difficulty of optimizing the wave fronts of two beams, pump and Stokes, with a single adaptive element. Surely it is a very ambitious vision but, as Hegel said, nothing great in the world has ever been accomplished without passion.

# List of Figures

# List of Tables

# Bibliography

[1] https://imagej.nih.gov/ij/index.html.

[2] Eijiro Adachi, Ian Hopkinson, and Toshihiko Hayashi. Basement-membrane stromal relationships: Interactions between collagen fibrils and the lamina densa. pages 73–156. Elsevier, 1997.

[3] Daniele Ancora, Tommaso Furieri, Stefano Bonora, and Andrea Bassi. Spinning pupil aberration measurement for anisoplanatic deconvolution. *Opt. Lett.*, 46(12):2884–2887, Jun 2021.

[4] Sergey N. Arkhipov, Ilyas Saytashev, and Marcos Dantus. Intravital imaging study on photodamage produced by femtosecond near-infrared laser pulses in vivo. *Photochemistry and Photobiology*, 92(2):308–313, feb 2016.

[5] J. A. Armstrong, N. Bloembergen, J. Ducuing, and P. S. Pershan. Interactions between light waves in a nonlinear dielectric. *Physical Review*, 127(6):1918–1939, September 1962.

[6] Brian D. Bennett, Thomas L. Jetton, Guangtao Ying, Mark A. Magnuson, and David W. Piston. Quantitative subcellular imaging of glucose metabolism within intact pancreatic islets. *Journal of Biological Chemistry*, 271(7):3647–3651, February 1996.

[7] Joseph Berkson. Application of the logistic function to bio-assay. *Journal of the American Statistical Association*, 39(227):357–365, sep 1944.

[8] Elif Bilgiç, Ãzge Boyacıoğlu, Merve Gizer, Petek Korkusuz, and Feza Korkusuz. Architecture of bone tissue and its adaptation to pathological conditions. In *Comparative Kinesiology of the Human Body*, pages 71–90. Elsevier, 2020.

[9] Andreas Bodén, Francesca Pennacchietti, Giovanna Coceano, Martina Damenti, Michael Ratz, and Ilaria Testa. Volumetric live cell imaging with three-dimensional parallelized RESOLFT microscopy. *Nature Biotechnology*, 39(5):609–618, jan 2021.

[10] Georges Boivin. The hydroxyapatite crystal: A closer look. *Medicographia*, 29:126–132, 01 2007.

[11] Martin J Booth. Wavefront sensorless adaptive optics for large aberrations. *Optics letters*, 32(1):5–7, 2007.

[12] Martin J Booth. Adaptive optical microscopy: the ongoing quest for a perfect image. *Light: Science & Applications*, 3(4):e165–e165, 2014.

[13] Martin J Booth, Delphine Débarre, and Tony Wilson. Image-based wavefront sensorless adaptive optics. In *Advanced Wavefront Control: Methods, Devices, and Applications V*, volume 6711, page 671102. International Society for Optics and Photonics, 2007.

[14] Adele L. Boskey and Pamela Gehron Robey. The composition of bone. pages 49–58. John Wiley & Sons, Inc., July 2013.

[15] S.W. Botchway, P. Reynolds, A.W. Parker, and P. O'Neill. Use of near infrared femtosecond lasers as sub-micron radiation microbeam for cell DNA damage and repair studies. *Mutation Research/Reviews in Mutation Research*, 704(1-3):38–44, apr 2010.

[16] Robert W. Boyd. *Nonlinear Optics*. Academic Press, 2008.

[17] A. Bresci, M. Guizzardi, C. M. Valensise, F. Marangi, F. Scotognella, G. Cerullo, and D. Polli. Removal of cross-phase modulation artifacts in ultrafast pump–probe dynamics by deep learning. *APL Photonics*, 6(7):076104, July 2021.

[18] Juan M Bueno, Emilio J Gualda, and Pablo Artal. Adaptive optics multiphoton microscopy to study ex vivo ocular tissues. *Journal of biomedical optics*, 15(6):066004, 2010.

[19] William C. Burhans and Nicholas H. Heintz. The cell cycle is a redox cycle: Linking phase-specific targets to cell fate. *Free Radical Biology and Medicine*, 47(9):1282–1293, nov 2009.

[20] AH Burstein, JM Zika, KG Heiple, and L Klein. Contribution of collagen and mineral to the elastic-plastic properties of bone. 57(7):956–961, October 1975.

[21] C.H. Camp. Broadband coherent anti-stokes raman scattering. In *Imaging in Dermatology*, pages 155–168. Elsevier, 2016.

[22] Paul Campagnola. Second harmonic generation imaging microscopy: Applications to diseases diagnostics. *Analytical Chemistry*, 83(9):3224–3231, March 2011.

[23] P. M. Carlton, J. Boulanger, C. Kervrann, J.-B. Sibarita, J. Salamero, S. Gordon-Messer, D. Bressan, J. E. Haber, S. Haase, L. Shao, L. Winoto, A. Matsuda, P. Kner, S. Uzawa, M. Gustafsson, Z. Kam, D. A. Agard, and J. W. Sedat. Fast live simultaneous multiwavelength four-dimensional optical microscopy. *Proceedings of the National Academy of Sciences*, 107(37):16016–16022, aug 2010.

[24] Jae-Won Cha, Jerome Ballesta, and Peter TC So. Shack-hartmann wavefront-sensor-based adaptive optics system for multiphoton microscopy. *Journal of biomedical optics*, 15(4):046022, 2010.

[25] Martin Chalfie, Yuan Tu, Ghia Euskirchen, William W. Ward, and Douglas C. Prasher. Green fluorescent protein as a marker for gene expression. *Science*, 263(5148):802–805, February 1994.

[26] Zenghu Chang, Andy Rundquist, Haiwen Wang, Margaret M. Murnane, and Henry C. Kapteyn. Generation of coherent soft x rays at 2.7 nm using high harmonics. *Physical Review Letters*, 79(16):2967–2970, October 1997.

[27] Bi-Chang Chen, Jiha Sung, and Sang-Hyun Lim. Chemical imaging with frequency modulation coherent anti-stokes raman scattering microscopy at the vibrational fingerprint region. *The Journal of Physical Chemistry B*, 114(50):16871–16880, December 2010.

[28] Hongtao Chen, Haifeng Wang, Mikhail N. Slipchenko, YooKyung Jung, Yunzhou Shi, Jiabin Zhu, Kimberly K. Buhman, and Ji-Xin Cheng. A multimodal platform for nonlinear optical microscopy and microspectroscopy. *Optics Express*, 17(3):1282, jan 2009.

[29] I.-H. Chen, S.-W. Chu, C.-K. Sun, P.-C. Cheng, and B.-L. Lin. Wavelength dependent damage in biological multiphoton confocal microscopy: A micro-spectroscopic comparison between femtosecond ti:sapphire and cr:forsterite laser sources. *Optical and Quantum Electronics*, 34(12):1251–1266, 2002.

[30] J X Cheng and Xiaoliang Sunney. Xie. *Coherent Raman Scattering Microscopy*. CRC Press, 2013.

[31] J X Cheng and Xiaoliang Sunney. Xie. *Coherent Raman Scattering Microscopy*. CRC Press, 2013.

[32] Ji-Xin Cheng and X. Sunney Xie. Coherent anti-stokes raman scattering microscopy: instrumentation, theory, and applications. *The Journal of Physical Chemistry B*, 108(3):827–840, December 2003.

[33] Marcus T. Cicerone, Khaled A. Aamer, Young Jong Lee, and Erik Vartiainen. Maximum entropy and time-domain kramers-kronig phase retrieval approaches are functionally equivalent for CARS microspectroscopy. *Journal of Raman Spectroscopy*, 43(5):637–643, April 2012.

[34] Francesco Crisafi, Vikas Kumar, Antonio Perri, Marco Marangoni, Giulio Cerullo, and Dario Polli. Multimodal nonlinear microscope based on a compact fiber-format laser source. *Spectrochimica Acta Part A: Molecular and Biomolecular Spectroscopy*, 188:135–140, January 2018.

[35] Francesco Crisafi, Vikas Kumar, Tullio Scopigno, Marco Marangoni, Giulio Cerullo, and Dario Polli. In-line balanced detection stimulated raman scattering microscopy. *Scientific Reports*, 7(1), sep 2017.

[36] Matthew K. Daddysman, Michael A. Tycon, and Christopher J. Fecko. Photoinduced damage resulting from fluorescence imaging of live cells. In *Methods in Molecular Biology*, pages 1–17. Springer New York, 2014.

[37] Luca Dalbosco, Giulia Zanini, Elvira D'Amato, Francesco Tessarolo, Sebastiana Boi, Paolo Bauer, Albrecht Haase, and Renzo Antolini. Photodamage in deep tissue two-photon optical biopsy of human skin. *Journal of Biophotonics*, 8(10):816–825, dec 2014.

[38] Delphine Débarre, Nicolas Olivier, Willy Supatto, and Emmanuel Beaurepaire. Mitigating phototoxicity during multiphoton microscopy of live drosophila embryos in the 1.0–1.2 $\mu$m wavelength range. *PLoS ONE*, 9(8):e104250, aug 2014.

[39] Thomas J. Deerinck. The application of fluorescent quantum dots to confocal, multiphoton, and electron microscopic imaging. *Toxicologic Pathology*, 36(1):112–116, January 2008.

[40] W. Denk, J. Strickler, and W. Webb. Two-photon laser scanning fluorescence microscopy. *Science*, 248(4951):73–76, apr 1990.

[41] Winfried Denk. Two-photon excitation in functional biological imaging. *Journal of Biomedical Optics*, 1(3):296, 1996.

[42] Ram Dixit and Richard Cyr. Cell damage and reactive oxygen species production induced by fluorescence microscopy: effect on mitosis and guidelines for non-invasive fluorescence microscopy. *The Plant Journal*, 36(2):280–290, oct 2003.

[43] Jurek W. Dobrucki, Dorota Feret, and Anna Noatynska. Scattering of exciting light by live cells in fluorescence confocal imaging: Phototoxic effects and relevance for FRAP studies. *Biophysical Journal*, 93(5):1778–1786, sep 2007.

[44] Stephen Douthwright and Greenfield Sluder. Live cell imaging: Assessing the phototoxicity of 488 and 546 nm light and methods to alleviate it. *Journal of Cellular Physiology*, 232(9):2461–2468, apr 2017.

[45] Gisela Eckhardt, R. W. Hellwarth, F. J. McClung, S. E. Schwarz, D. Weiner, and E. J. Woodbury. Stimulated raman scattering from organic liquids. *Physical Review Letters*, 9(11):455–457, December 1962.

[46] Susan Elmore. Apoptosis: A review of programmed cell death. *Toxicologic Pathology*, 35(4):495–516, jun 2007.

[47] Delphine Farlay and Georges Boivi. Bone mineral quality. InTech, February 2012.

[48] A. V. Fedyaeva, A. V. Stepanov, I. V. Lyubushkina, T. P. Pobezhimova, and E. G. Rikhvanov. Heat shock induces production of reactive oxygen species and increases inner mitochondrial membrane potential in winter wheat cells. *Biochemistry (Moscow)*, 79(11):1202–1210, nov 2014.

[49] P. A. Franken, A. E. Hill, C. W. Peters, and G. Weinreich. Generation of optical harmonics. *Physical Review Letters*, 7(4):118–119, August 1961.

[50] Christian W. Freudiger, Wei Min, Brian G. Saar, Sijia Lu, Gary R. Holtom, Chengwei He, Jason C. Tsai, Jing X. Kang, and X. Sunney Xie. Label-free biomedical imaging with high sensitivity by stimulated raman scattering microscopy. *Science*, 322(5909):1857–1861, December 2008.

[51] Christian W. Freudiger, Wenlong Yang, Gary R. Holtom, Nasser Peyghambarian, X. Sunney Xie, and Khanh Q. Kieu. Stimulated raman scattering microscopy with a robust fibre laser source. *Nature Photonics*, 8(2):153–159, jan 2014.

[52] I. Freund, M. Deutsch, and A. Sprecher. Connective tissue polarity. optical second-harmonic microscopy, crossed-beam summation, and small-angle scattering in rat-tail tendon. *Biophysical Journal*, 50(4):693–712, October 1986.

[53] M. M. Frigault, J. Lacoste, J. L. Swift, and C. M. Brown. Live-cell microscopy - tips and tools. *Journal of Cell Science*, 122(6):753–767, mar 2009.

[54] Yan Fu, Haifeng Wang, Riyi Shi, and Ji-Xin Cheng. Characterization of photodamage in coherent anti-stokes raman scattering microscopy. *Optics Express*, 14(9):3942, 2006.

[55] Roberta Galli, Ortrud Uckermann, Elisabeth F. Andresen, Kathrin D. Geiger, Edmund Koch, Gabriele Schackert, Gerald Steiner, and Matthias Kirsch. Intrinsic indicator of photodamage during label-free multiphoton microscopy of cells and tissues. *PLoS ONE*, 9(10):e110295, oct 2014.

[56] Feruz Ganikhanov, Conor L. Evans, Brian G. Saar, and X. Sunney Xie. High-sensitivity vibrational imaging with frequency modulation coherent anti-stokes raman scattering (FM CARS) microscopy. *Optics Letters*, 31(12):1872, June 2006.

[57] Derek J. Gardiner. Introduction to raman scattering. In *Practical Raman Spectroscopy*, pages 1–12. Springer Berlin Heidelberg, 1989.

[58] E. Garmire, F. Pandarese, and C. H. Townes. Coherently driven molecular vibrations and light modulation. *Physical Review Letters*, 11(4):160–163, August 1963.

[59] Alfonso Gautieri, Simone Vesentini, Alberto Redaelli, and Markus J. Buehler. Hierarchical structure and nanomechanics of collagen microfibrils from the atomistic scale up. 11(2):757–766, February 2011.

[60] Antoine G. Godin, Brahim Lounis, and Laurent Cognet. Super-resolution microscopy approaches for live cell imaging. *Biophysical Journal*, 107(8):1777–1784, oct 2014.

[61] Maria Göppert-Mayer. Über elementarakte mit zwei quantensprüngen. *Annalen der Physik*, 401(3):273–294, 1931.

[62] G.Placzek. *Rayleigh-Streuung und Raman-Effekt*. Handbuch der Radiologie, E. Marx, Ed. Akademische Verlagsgesellschaft, Leipzig, Germany, 1934.

[63] Z. T. Gu, L. Li, F. WU, P. Zhao, H. Yang, Y. S. Liu, Y. Geng, M. Zhao, and L. Su. Heat stress induced apoptosis is triggered by transcription-independent p53, ca2 dyshomeostasis and the subsequent bax mitochondrial translocation. *Scientific Reports*, 5(1), jun 2015.

[64] Z. T. Gu, H. Wang, L. Li, Y. S. Liu, X. B. Deng, S. F. Huo, F. F. Yuan, Z. F. Liu, H. S. Tong, and L. Su. Heat stress induces apoptosis through transcription-independent p53-mediated mitochondrial pathways in human umbilical vein endothelial cell. *Scientific Reports*, 4(1), mar 2014.

[65] Yici Guo, P. P. Ho, H. Savage, D. Harris, P. Sacks, S. Schantz, Feng Liu, N. Zhadin, and R. R. Alfano. Second-harmonic tomography of tissues. *Optics Letters*, 22(17):1323, September 1997.

[66] V. P. Gupta. *Molecular and Laser Spectroscopy - Advances and Applications*. John Fedor, 2017.

[67] D. J. Hadjdakis and I. I. Androulakis. Bone remodeling. 1092(1):385–396, December 2006.

[68] R. Le Harzic, I. Riemann, K. Koenig, C. Wullner, and C. Donitzky. Influence of femtosecond laser pulse irradiation on the viability of cells at 1035, 517, and 345nm. *Journal of Applied Physics*, 102(11):114701, dec 2007.

[69] R A Hoebe, C H Van Oven, T W J Gadella, P B Dhonukshe, C J F Van Noorden, and E M M Manders. Controlled light-exposure microscopy reduces photobleaching and phototoxicity in fluorescence live-cell imaging. *Nature Biotechnology*, 25(2):249–253, jan 2007.

[70] Alexander Hopt and Erwin Neher. Highly nonlinear photodamage in two-photon fluorescence microscopy. *Biophysical Journal*, 80(4):2029–2036, apr 2001.

[71] H. Hora. Y. r. shen, the principles of nonlinear optics, john wiley & sons, new york, 1984, 576 pages. *Laser and Particle Beams*, 4(2):318–319, May 1986.

[72] Ya-Ling Hsu, Hsin-Su Yu, Hsien-Chung Lin, Kwou-Yeung Wu, Rei-Cheng Yang, and Po-Lin Kuo. Heat shock induces apoptosis through reactive oxygen species involving mitochondrial and death receptor pathways in corneal cells. *Experimental Eye Research*, 93(4):405–412, oct 2011.

[73] T.B. Huff and J.-X. Cheng. In vivo coherent anti-stokes raman scattering imaging of sciatic nerve tissue. *Journal of Microscopy*, 225(2):175–182, February 2007.

[74] Jaroslav Icha, Michael Weber, Jennifer C. Waters, and Caren Norden. Phototoxicity in live fluorescence microscopy, and how to avoid it. *BioEssays*, 39(8):1700003, jul 2017.

[75] Darian S. James and Paul J. Campagnola. Recent advancements in optical harmonic generation microscopy: Applications and perspectives. *BME Frontiers*, 2021:1–24, February 2021.

[76] Minbiao Ji, Daniel A. Orringer, Christian W. Freudiger, Shakti Ramkissoon, Xiaohui Liu, Darryl Lau, Alexandra J. Golby, Isaiah Norton, Marika Hayashi, Nathalie Y. R. Agar, Geoffrey S. Young, Cathie Spino, Sandro Santagata, Sandra Camelo-Piragua, Keith L. Ligon, Oren Sagher, and X. Sunney Xie. Rapid, label-free detection of brain tumors with stimulated raman scattering microscopy. *Science Translational Medicine*, 5(201), sep 2013.

[77] Xingshan Jiang, Jiazhao Zhong, Yuchun Liu, Haibo Yu, Shuangmu Zhuo, and Jianxin Chen. Two-photon fluorescence and second-harmonic generation imaging of collagen in human tissue based on multiphoton microscopy. *Scanning*, 33(1):53–56, January 2011.

[78] Charles H. Camp Jr, Young Jong Lee, John M. Heddleston, Christopher M. Hartshorn, Angela R. Hight Walker, Jeremy N. Rich, Justin D. Lathia, and Marcus T. Cicerone. High-speed coherent raman fingerprint imaging of biological tissues. *Nature Photonics*, 8(8):627–634, July 2014.

[79] H. Kafantari, E. Kounadi, M. Fatouros, M. Milonakis, and M. Tzaphlidou. Structural alterations in rat skin and bone collagen fibrils induced by ovariectomy. 26(4):349–353, April 2000.

[80] W. Kaiser and C. G. B. Garrett. Two-photon excitation in caf2:eu2. *Physical Review Letters*, 7(6):229–231, September 1961.

[81] S. Kalies, K. Kuetemeyer, and A. Heisterkamp. Mechanisms of high-order photobleaching and its relationship to intracellular ablation. *Biomedical Optics Express*, 2(4):805, mar 2011.

[82] Vivekanand Sabanna Kattimani, Sudheer Kondaka, and Krishna Prasad Lingamaneni. Hydroxyapatite–-past, present, and future in bone regeneration. 7:BTRI.S36138, January 2016.

[83] Mohammad E. Khosroshahi. *Applications of Biophotonics and Nanobiomaterials in Biomedical Engineering*. CRC Press, oct 2017.

[84] Alex Kiepas, Elena Voorand, Firas Mubaid, Peter M. Siegel, and Claire M. Brown. Optimizing live-cell fluorescence imaging conditions to minimize phototoxicity. *Journal of Cell Science*, 133(4):jcs242834, jan 2020.

[85] L. Kirkpatrick and G. Wheeler. *Physics : a world view*. Philadelphia : Saunders College Pub., 1995.

[86] K. Koenig. Multiphoton microscopy in life sciences. *Journal of Microscopy*, 200(2):83–104, nov 2000.

[87] K. Koenig, T. W. Becker, P. Fischer, I. Riemann, and K.-J. Halbhuber. Pulse-length dependence of cellular response to intense near-infrared laser pulses in multiphoton microscopes. *Optics Letters*, 24(2):113, jan 1999.

[88] K. Koenig, H. Liang, M. W. Berns, and B. J. Tromberg. Cell damage by near-IR microbeams. *Nature*, 377(6544):20–21, sep 1995.

[89] Karsten Koenig. Cell damage during multi-photon microscopy. In *Handbook Of Biological Confocal Microscopy*, pages 680–689. Springer US, 2006.

[90] Helmut J. Koester, Dagmar Baur, Rainer Uhl, and Stefan W. Hell. Ca2 fluorescence imaging with pico- and femtosecond two-photon excitation: Signal and photodamage. *Biophysical Journal*, 77(4):2226–2236, oct 1999.

[91] Xiangduo Kong, Samarendra K. Mohanty, Jared Stephens, Jason T. Heale, Veronica Gomez-Godinez, Linda Z. Shi, Jong-Soo Kim, Kyoko Yokomori, and Michael W. Berns. Comparative analysis of different laser systems to study cellular responses to DNA damage in mammalian cells. *Nucleic Acids Research*, 37(9):e68–e68, apr 2009.

[92] J.J. Kruzic, D.K. Kim, K.J. Koester, and R.O. Ritchie. Indentation techniques for evaluating the fracture toughness of biomaterials and hard tissues. 2(4):384–395, August 2009.

[93] Rishikesh U Kulkarni, Matthieu Vandenberghe, Martin Thunemann, Feroz James, Ole A Andreassen, Srdjan Djurovic, Anna Devor, and Evan W Miller. In vivo two-photon voltage imaging with sulfonated rhodamine dyes. *ACS central science*, 4(10):1371–1378, 2018.

[94] Philippe Laissue, Rana A. Alghamdi, Pavel Tomancak, Emmanuel G. Reynaud, and Hari Shroff. Assessing phototoxicity in live fluorescence imaging. *Nature Methods*, 14(7):657–661, jul 2017.

[95] Joseph R. Lakowicz. *Principles of Fluorescence Spectroscopy*. Springer US, 2006.

[96] Thuc T. Le and Ji-Xin Cheng. Single-cell profiling reveals the origin of phenotypic variability in adipogenesis. *PLoS ONE*, 4(4):e5189, April 2009.

[97] Soo-Y. Lee, Donghui Zhang, David W. McCamant, Philipp Kukura, and Richard A. Mathies. Theory of femtosecond stimulated raman spectroscopy. *The Journal of Chemical Physics*, 121(8):3632–3642, August 2004.

[98] Young Jong Lee, Yuexin Liu, and Marcus T. Cicerone. Characterization of three-color CARS in a two-pulse broadband CARS spectrum. *Optics Letters*, 32(22):3370, November 2007.

[99] M. Lewenstein, Ph. Balcou, M. Yu. Ivanov, Anne L'Huillier, and P. B. Corkum. Theory of high-harmonic generation by low-frequency laser fields. *Physical Review A*, 49(3):2117–2132, mar 1994.

[100] Haonan Lin, Hyeon Jeong Lee, Nathan Tague, Jean-Baptiste Lugagne, Cheng Zong, Fengyuan Deng, Jonghyeon Shin, Lei Tian, Wilson Wong, Mary J Dunlop, and Ji Xin Cheng. Microsecond fingerprint stimulated raman spectroscopic imaging by ultrafast tuning and spatial-spectral learning. *Nature communications*, 12(1):1–12, 2021.

[101] Tsung-Li Liu, Srigokul Upadhyayula, Daniel E. Milkie, Ved Singh, Kai Wang, Ian A. Swinburne, Kishore R. Mosaliganti, Zach M. Collins, Tom W. Hiscock, Jamien Shea, Abraham Q. Kohrman, Taylor N. Medwig, Daphne Dambournet, Ryan Forster, Brian Cunniff, Yuan Ruan, Hanako Yashiro, Steffen Scholpp, Elliot M. Meyerowitz, Dirk Hockemeyer, David G. Drubin, Benjamin L. Martin, David Q. Matus, Minoru Koyama, Sean G. Megason, Tom Kirchhausen, and Eric Betzig. Observing the cell in its native state: Imaging subcellular dynamics in multicellular organisms. *Science*, 360(6386), 2018.

[102] Y. Liu, D.K. Cheng, G.J. Sonek, M.W. Berns, C.F. Chapman, and B.J. Tromberg. Evidence for localized cell heating induced by infrared optical tweezers. *Biophysical Journal*, 68(5):2137–2144, may 1995.

[103] Fa-Ke Lu, Srinjan Basu, Vivien Igras, Mai P. Hoang, Minbiao Ji, Dan Fu, Gary R. Holtom, Victor A. Neel, Christian W. Freudiger, David E. Fisher, and X. Sunney Xie. Label-free DNA imaging in vivo with stimulated raman scattering microscopy. *Proceedings of the National Academy of Sciences*, 112(37):11624–11629, aug 2015.

[104] C. Macias-Romero, V. Zubkovs, S. Wang, and S. Roke. Wide-field medium-repetition-rate multiphoton microscopy reduces photodamage of living cells. *Biomedical Optics Express*, 7(4):1458, mar 2016.

[105] Valentin Magidson and Alexey Khodjakov. Circumventing photodamage in live-cell microscopy. In *Methods in Cell Biology*, pages 545–560. Elsevier, 2013.

[106] Virendra N Mahajan. Zernike circle polynomials and optical aberrations of systems with circular pupils. *Applied optics*, 33(34):8121–8124, 1994.

[107] T. H. Maiman. Stimulated optical radiation in ruby. *Nature*, 187(4736):493–494, August 1960.

[108] P. D. Maker and R. W. Terhune. Study of optical effects due to an induced polarization third order in the electric field strength. *Physical Review*, 137(3A):A801–A818, feb 1965.

[109] Marco Marchetti, Enrico Baria, Riccardo Cicchi, and Francesco Saverio Pavone. Custom multiphoton/raman microscopy setup for imaging and characterization of biological samples. *Methods and Protocols*, 2(2):51, June 2019.

[110] P.-O. Mari, B. I. Florea, S. P. Persengiev, N. S. Verkaik, H. T. Bruggenwirth, M. Modesti, G. Giglia-Mari, K. Bezstarosti, J. A. A. Demmers, T. M. Luider, A. B. Houtsmuller, and D. C. van Gent. Dynamic assembly of end-joining complexes requires interaction between ku70/80 and XRCC4. *Proceedings of the National Academy of Sciences*, 103(49):18597–18602, nov 2006.

[111] Barry R. Masters and Peter T. C. So. *Handbook of Biological Nonlinear Optical Microscopy*. Oxford University Press, 2008.

[112] B.R. Masters, P.T. So, and E. Gratton. Multiphoton excitation fluorescence microscopy and spectroscopy of in vivo human skin. *Biophysical Journal*, 72(6):2405–2412, jun 1997.

[113] John R. Masters. HeLa cells 50 years on: the good, the bad and the ugly. *Nature Reviews Cancer*, 2(4):315–319, apr 2002.

[114] Nirmal Mazumder, Naveen K. Balla, Guan-Yu Zhuo, Yury V. Kistenev, Rajesh Kumar, Fu-Jen Kao, Sophie Brasselet, Viktor V. Nikolaev, and Natalya A. Krivova. Label-free non-linear multimodal optical microscopy—basics, development, and applications. *Frontiers in Physics*, 7, oct 2019.

[115] L.M. McNamara. 2.10 bone as a material. pages 202–227. Elsevier, 2017.

[116] Ciro Menale, Lisa J Robinson, Eleonora Palagano, Rosita Rigoni, Marco Erreni, Alejandro J Almarza, Dario Strina, Stefano Mantero, Michela Lizier, Antonella Forlino, Roberta Besio, Marta Monari, Paolo Vezzoni, Barbara Cassani, Harry C Blair, Anna Villa, and Cristina Sobacchi. Absence of dipeptidyl peptidase 3 increases oxidative stress and causes bone loss. *Journal of bone and mineral research: the official journal of the American Society for Bone and Mineral research*, 34(11):2133–2148, September 2019.

[117] Jerome Mertz. *Introduction to Optical Microscopy*. Cambridge University Press, July 2019.

[118] Takeo Minamikawa, Yoshinori Murakami, Naokazu Matsumura, Hirohiko Niioka, Shuichiro Fukushima, Tsutomu Araki, and Mamoru Hashimoto. Photo-induced cell damage analysis for single- and multifocus coherent anti-stokes raman scattering microscopy. *Journal of Spectroscopy*, 2017:1–8, 2017.

[119] A. S. Mishin and K. A. Lukyanov. Live-cell super-resolution fluorescence microscopy. *Biochemistry (Moscow)*, 84(S1):19–31, jan 2019.

[120] L. Moreaux, O. Sandre, and J. Mertz. Membrane imaging by second-harmonic generation microscopy. *Journal of the Optical Society of America B*, 17(10):1685, October 2000.

[121] Leila Mostaço-Guidolin, Nicole Rosin, and Tillie-Louise Hackett. Imaging collagen in scar tissue: Developments in second harmonic generation microscopy for biomedical applications. *International Journal of Molecular Sciences*, 18(8):1772, August 2017.

[122] Xiaolin Nan, Eric O. Potma, and X. Sunney Xie. Nonperturbative chemical imaging of organelle transport in living cells with coherent anti-stokes raman scattering microscopy. *Biophysical Journal*, 91(2):728–735, jul 2006.

[123] Markolf H. Niemz. *Laser-Tissue Interactions*. Springer, 2002.

[124] Joanna Olesiak-Banska, Piotr Hanczyc, Katarzyna Matczyszyn, Bengt Norden, and Marek Samoc. Nonlinear absorption spectra of ethidium and ethidium homodimer. *Chemical Physics*, 404:33–35, aug 2012.

[125] Daniel A. Orringer, Balaji Pandian, Yashar S. Niknafs, Todd C. Hollon, Julianne Boyle, Spencer Lewis, Mia Garrard, Shawn L. Hervey-Jumper, Hugh J. L. Garton, Cormac O. Maher, Jason A. Heth, Oren Sagher, D. Andrew Wilkinson, Matija Snuderl, Sriram Venneti, Shakti H. Ramkissoon, Kathryn A. McFadden, Amanda Fisher-Hubbard, Andrew P. Lieberman, Timothy D. Johnson, X. Sunney Xie, Jay K. Trautman, Christian W. Freudiger, and Sandra Camelo-Piragua. Rapid intraoperative histology of unprocessed surgical specimens via fibre-laser-based stimulated raman scattering microscopy. *Nature Biomedical Engineering*, 1(2), feb 2017.

[126] Jean-Louis Oudar, Robert W. Smith, and Y. R. Shen. Polarization-sensitive coherent anti-stokes raman spectroscopy. *Applied Physics Letters*, 34(11):758–760, June 1979.

[127] Dimitre G Ouzounov, Tianyu Wang, Mengran Wang, Danielle D Feng, Nicholas G Horton, Jean C Cruz-Hernández, Yu-Ting Cheng, Jacob Reimer, Andreas S Tolias, Nozomi Nishimura, and Chris Xu. In vivo three-photon imaging of activity of gcamp6-labeled neurons deep in intact mouse brain. *Nature methods*, 14(4):388–390, 2017.

[128] John Paoli, Maria Smedh, Ann-Marie Wennberg, and Marica B. Ericson. Multiphoton laser scanning microscopy on non-melanoma skin cancer: Morphologic features for future non-invasive diagnostics. *Journal of Investigative Dermatology*, 128(5):1248–1255, may 2008.

[129] Byoung Kyoo Park, Namwoo Yi, Jaesung Park, and Dongsik Kim. Thermal conductivity of single biological cells and relation with cell viability. *Applied Physics Letters*, 102(20):203702, may 2013.

[130] Jung-Hoon Park, Lingjie Kong, Yifeng Zhou, and Meng Cui. Large-field-of-view imaging by multi-pupil adaptive optics. *Nature methods*, 14(6):581–583, 2017.

[131] Valentina Parodi, Emanuela Jacchetti, Arianna Bresci, Benedetta Talone, Carlo M. Valensise, Roberto Osellame, Giulio Cerullo, Dario Polli, and Manuela T. Raimondi. Characterization of mesenchymal stem cell differentiation within miniaturized 3d scaffolds through advanced microscopy techniques. *International Journal of Molecular Sciences*, 21(22):8498, November 2020.

[132] Eleftherios P Paschalis, Elizabeth Shane, George Lyritis, Grigoris Skarantavos, Richard Mendelsohn, and Adele L Boskey. Bone fragility and collagen cross-links. 19(12):2000–2004, August 2004.

[133] Adrian F. Pegoraro, Andrew Ridsdale, Douglas J. Moffatt, Yiwei Jia, John Paul Pezacki, and Albert Stolow. Optimally chirped multimodal CARS microscopy based on a single ti:sapphire oscillator. *Optics Express*, 17(4):2984, February 2009.

[134] D Pestov, Y Andegeko, V V Lozovoy, and M Dantus. Photobleaching and photoenhancement of endogenous fluorescence observed in two-photon microscopy with broadband laser sources. *Journal of Optics*, 12(8):084006, jul 2010.

[135] G. Bush Peter. Two-versus one photon excitation laser scanning microscopy : Critical importance of excitation wavelength. *Frontiers in Bioscience*, 12(1):2646, 2007.

[136] Iestyn Pope, Wolfgang Langbein, Peter Watson, and Paola Borri. Simultaneous hyperspectral differential-CARS, TPF and SHG microscopy with a single 5 fs ti:sa laser. *Optics Express*, 21(6):7096, mar 2013.

[137] Paolo Pozzi, Daniela Gandolfi, Carlo Adolfo Porro, Albertino Bigiani, and Jonathan Mapelli. Scattering compensation for deep brain microscopy: The long road to get proper images. *Frontiers in Physics*, 8:26, 2020.

[138] Paolo Pozzi, Carlas Smith, Elizabeth Carroll, Dean Wilding, Oleg Soloviev, Martin Booth, Gleb Vdovin, and Michel Verhaegen. Anisoplanatic adaptive optics in parallelized laser scanning microscopy. *Optics express*, 28(10):14222–14236, 2020.

[139] Paolo Pozzi, Oleg Soloviev, Dean Wilding, Gleb Vdovin, and Michel Verhaegen. Optimal model-based sensorless adaptive optics for epifluorescence microscopy. *PloS one*, 13(3):e0194523, 2018.

[140] Paolo Pozzi, Dean Wilding, Oleg Soloviev, Hans Verstraete, Laurens Bliek, Gleb Vdovin, and Michel Verhaegen. High speed wavefront sensorless aberration correction in digital micromirror based confocal microscopy. *Optics Express*, 25(2):949–959, 2017.

[141] William K. Pratt. *Introduction to Digital Image Processing*. CRC Press, September 2013.

[142] Richard C. Prince, Renee R. Frontiera, and Eric O. Potma. Stimulated raman scattering: From bulk to nano. *Chemical Reviews*, 117(7):5070–5094, December 2016.

[143] Yifan Qin and Yuanqin Xia. Simultaneous two-photon fluorescence microscopy of NADH and FAD using pixel-to-pixel wavelength-switching. *Frontiers in Physics*, 9, March 2021.

[144] R. Woods R. Gonzalez. *Digital Image Processing*. Addison Wesley, 1992.

[145] Pouya Rajaeipour, Alex Dorn, Kaustubh Banerjee, Hans Zappe, and Çağlar Ataman. Extended field-of-view adaptive optics in microscopy via numerical field segmentation. *Applied optics*, 59(12):3784–3791, 2020.

[146] C. V. RAMAN and K. S. KRISHNAN. A new type of secondary radiation. *Nature*, 121(3048):501–502, March 1928.

[147] Jae-Young Rho, Liisa Kuhn-Spearing, and Peter Zioupos. Mechanical properties and the hierarchical structure of bone. 20(2):92–102, March 1998.

[148] David Richmond, Anna Payne-Tobin Jost, Talley Lambert, Jennifer Waters, and Hunter Elliott. Deadnet: Identifying phototoxicity from label-free microscopy images of cells using deep convnets. *arXiv Prepr. arXiv1701.06109*, 2017.

[149] Ian Seungwan Ryu, Charles H. Camp, Ying Jin, Marcus T. Cicerone, and Young Jong Lee. Beam scanning for rapid coherent raman hyperspectral imaging. *Optics Letters*, 40(24):5826, dec 2015.

[150] Debayan Saha, Uwe Schmidt, Qinrong Zhang, Aurelien Barbotin, Qi Hu, Na Ji, Martin J Booth, Martin Weigert, and Eugene W Myers. Practical sensorless aberration estimation for 3d microscopy with deep learning. *Optics Express*, 28(20):29044–29053, 2020.

[151] Michael J. Sanderson, Ian Smith, Ian Parker, and Martin D. Bootman. Fluorescence microscopy. *Cold Spring Harbor Protocols*, 2014(10):pdb.top071795, oct 2014.

[152] Norman Schulman and Eric J. Hall. Hyperthermia: Its effect on proliferative and plateau phase cell cultures. *Radiology*, 113(1):209–211, oct 1974.

[153] Ego Seeman and Pierre D. Delmas. Bone quality — the material and structural basis of bone strength and fragility. 354(21):2250–2261, May 2006.

[154] Pabitra N. Sen. Time-dependent diffusion coefficient as a probe of geometry. *Concepts in Magnetic Resonance Part A*, 23A(1):1–21, 2004.

[155] Vladimir Shafirovich, Alexander Dourandin, Natalia P. Luneva, Carolyn Singh, Francis Kirigin, and Nicholas E. Geacintov. Multiphoton near-infrared femtosecond laser pulse-induced DNA damage with and without the photosensitizer proflavine. *Photochemistry and Photobiology*, 69(3):265, 1999.

[156] Matthew D. Shoulders and Ronald T. Raines. Collagen structure and stability. 78(1):929–958, June 2009.

[157] Daniela Fatima Teixeira Silva, Raquel Agnelli Mesquita-Ferrari, Kristianne Porta Santos Fernandes, Marcus Paulo Raele, Niklaus Ursus Wetter, and Alessandro Melo Deana. Effective transmission of light for media culture, plates and tubes. *Photochemistry and Photobiology*, 88(5):1211–1216, jun 2012.

[158] A. Silve, N. Dorval, T. Schmid, L.M. Mir, and B. Attal-Tretout. A wide-field arrangement for single-shot CARS imaging of living cells. *Journal of Raman Spectroscopy*, 43(5):644–650, apr 2012.

[159] Rajeshwar P. Sinha and Donat-P. HÃ¤der. UV-induced DNA damage and repair: a review. *Photochemical & Photobiological Sciences*, 1(4):225–236, mar 2002.

[160] T. M. Skirven, A. L. Osterman, J. Fedorczyk, P. C. Amadio, S. Felder, and E. K. Shin. *Reabilitation of the Hand and Upper Extremity*. 7 edition, 2021.

[161] Imen Belhadj Slimen, Taha Najar, Abdeljelil Ghram, Hajer Dabbebi, Moncef Ben Mrad, and Manef Abdrabbah. Reactive oxygen species, heat stress and oxidative-induced mitochondrial damage. a review. *International Journal of Hyperthermia*, 30(7):513–523, oct 2014.

[162] Irwin Sobel. An isotropic 3x3 image gradient operator. *Presentation at Stanford A.I. Project 1968*, 02 2014.

[163] I. D. Stein and G. Granik. Rib structure and bending strength: An autopsy study. 20(1):61–73, December 1976.

[164] Mats Stenström, Birger Olander, Daisy Lehto-Axtelius, Jan Erik Madsen, Lars Nordsletten, and Gudrun Alm Carlsson. Bone mineral density and bone structure parameters as predictors of bone strength: an analysis using computerized microtomography and gastrectomy-induced osteopenia in the rat. 33(3):289–297, March 2000.

[165] John H. Stockley, Kimberley Evans, Moritz Matthey, Katrin Volbracht, Sylvia Agathou, Jana Mukanowa, Juan Burrone, and Ragnhildur T. Káradóttir. Surpassing light-induced cell damage in vitro with novel cell culture media. *Scientific Reports*, 7(1), apr 2017.

[166] Chiara Stringari, Lamiae Abdeladim, Guy Malkinson, Pierre Mahou, Xavier Solinas, Isabelle Lamarre, Sébastien Brizion, Jean-Baptiste Galey, Willy Supatto, Renaud Legouis, Ana-Maria Pena, and Emmanuel Beaurepaire. Multicolor two-photon imaging of endogenous fluorophores in living tissues by wavelength mixing. *Scientific Reports*, 7(1), June 2017.

[167] B. Talone, M. Bazzarelli, A. Schirato, F. Dello Vicario, D. Viola, E. Jacchetti, M. Bregonzio, M. T. Raimondi, G. Cerullo, and D. Polli. Phototoxicity induced in living HeLa cells by focused femtosecond laser pulses: a data-driven approach. *Biomedical Optics Express*, 12(12):7886, dec 2021.

[168] Benedetta Talone, Paolo Pozzi, Miriam Cavagnini, Dario Polli, Gianluca Pozzi, and Jonathan Mapelli. Experimental determination of shift-less aberration bases for sensorless adaptive optics in nonlinear microscopy. *Optics Express*, 29(23):37617, oct 2021.

[169] Sharon Thomsen. Pathologic analysis of photothermal and photochemical effects of laser-tissue interactions. *Photochemistry and Photobiology*, 53(6):825–835, jun 1991.

[170] Kurt Thorn. Genetically encoded fluorescent tags. *Molecular Biology of the Cell*, 28(7):848–857, April 2017.

[171] LeAnn M. Tiede and Michael G. Nichols. Photobleaching of reduced nicotinamide adenine dinucleotide and the development of highly fluorescent lesions in rat basophilic leukemia cells during multiphoton microscopy. *Photochemistry and Photobiology*, 82(3):656, 2006.

[172] Kalina L. Tosheva, Yue Yuan, Pedro M. Pereira, Siân Culley, and Ricardo Henriques. Between life and death: Reducing phototoxicity in super-resolution microscopy. *Preprints*, aug 2019.

[173] Y S Touloukian, R W Powell, C Y Ho, and P G Klemens. *Thermophysical properties of matter - the TPRC data series. Volume2. Thermal conductivity - nonmetallic solids.* 1971.

[174] C. M. Valensise, A. Giuseppi, F. Vernuccio, A. De la Cadena, G. Cerullo, and D. Polli. Removing non-resonant background from CARS spectra via deep learning. *APL Photonics*, 5(6):061305, June 2020.

[175] David Vernon. *Machine Vision: Automated Visual Inspection and Robot Vision*. Prentice-Hall, Inc., USA, 1991.

[176] A. Vogel, J. Noack, G. Huttman, and G. Paltauf. Mechanisms of femtosecond laser nanosurgery of cells and tissues. *Applied Physics B*, 81(8):1015–1047, nov 2005.

[177] A. Vogel, J. Noack, K. Nahen, D. Theisen, S. Busch, U. Parlitz, D.X. Hammer, G.D. Noojin, B.A. Rockwell, and R. Birngruber. Energy balance of optical breakdown in water at nanosecond to femtosecond time scales. *Applied Physics B*, 68(2):271–280, feb 1999.

[178] Alfred Vogel and Vasan Venugopalan. Mechanisms of pulsed laser ablation of biological tissues. *Chemical Reviews*, 103(2):577–644, feb 2003.

[179] Andreas Volkmer, Ji-Xin Cheng, and X. Sunney Xie. Vibrational imaging with high sensitivity via epidetected coherent anti-stokes raman scattering microscopy. *Physical Review Letters*, 87(2), June 2001.

[180] von F. Zernike. Beugungstheorie des schneidenver-fahrens und seiner verbesserten form, der phasenkontrastmethode. *Physica*, 1(7-12):689–704, may 1934.

[181] Sina Waeldchen, Julian Lehmann, Teresa Klein, Sebastian van de Linde, and Markus Sauer. Light-induced cell damage in live-cell super-resolution microscopy. *Scientific Reports*, 5(1), oct 2015.

[182] Haifeng Wang, Yan Fu, Phyllis Zickmund, Riyi Shi, and Ji-Xin Cheng. Coherent anti-stokes raman scattering imaging of axonal myelin in live spinal tissues. *Biophysical Journal*, 89(1):581–591, July 2005.

[183] Xiaodu Wang, Ruud A. Bank, Johan M. Tekoppele, and C. Mauli Agrawal. The role of collagen in determining bone mechanical properties. 19(6):1021–1026, November 2001.

[184] Stephen Weiner and Wolfie Traub. Organization of hydroxyapatite crystals within collagen fibrils. 206(2):262–266, October 1986.

[185] C. Werner, B. F. Iversen, and M. H. Therkildsen. Contribution of the trabecular component to mechanical strength and bone mineral content of the femoral neck. an experimental study on cadaver bones. 48(5):457–460, September 1988.

[186] Rebecca M Williams, Warren R Zipfel, and Watt W Webb. Multiphoton microscopy in biological research. *Current Opinion in Chemical Biology*, 5(5):603–608, October 2001.

[187] E. J. Woodbury and W. K. Ng. Ruby laser operation in near ir. *Proceedings of the IRE*, 50(11):2365–2383, 1962.

[188] Ji xin Cheng, Andreas Volkmer, Lewis D. Book, and X. Sunney Xie. An epi-detected coherent anti-stokes raman scattering (e-CARS) microscope with high spectral resolution and high sensitivity. *The Journal of Physical Chemistry B*, 105(7):1277–1280, February 2001.

[189] Tatsuo Yajima and Masamoto Takatsuji. Higher order optical mixing of raman laser light in nonlinear dielectric media. *Journal of the Physical Society of Japan*, 19(12):2343–2344, dec 1964.

[190] Huizhen Yang, Oleg Soloviev, and Michel Verhaegen. Model-based wavefront sensorless adaptive optics system for large aberrations and extended objects. *Optics express*, 23(19):24587–24601, 2015.

[191] Michael D. Young, Jeffrey J. Field, Kraig E. Sheetz, Randy A. Bartels, and Jeff Squier. A pragmatic guide to multiphoton microscope design. *Advances in Optics and Photonics*, 7(2):276, jun 2015.

[192] Jin Zhang, Robert E. Campbell, Alice Y. Ting, and Roger Y. Tsien. Creating new fluorescent probes for cell biology. *Nature Reviews Molecular Cell Biology*, 3(12):906–918, December 2002.

[193] W. R. Zipfel, R. M. Williams, R. Christie, A. Y. Nikitin, B. T. Hyman, and W. W. Webb. Live tissue intrinsic emission microscopy using multiphoton-excited native fluorescence and second harmonic generation. *Proceedings of the National Academy of Sciences*, 100(12):7075–7080, may 2003.

[194] Warren R Zipfel, Rebecca M Williams, and Watt W Webb. Nonlinear magic: multiphoton microscopy in the biosciences. *Nature Biotechnology*, 21(11):1369–1377, October 2003.

[195] Aikaterini Zoumi, Alvin T. Yeh, and Bruce J. Tromberg. Combined two-photon excited fluorescence and second-harmonic generation backscattering microscopy of turbid tissues. In Ammasi Periasamy and Peter T. C. So, editors, *Multiphoton Microscopy in the Biomedical Sciences II*. SPIE, June 2002.

[196] Andreas Zumbusch, Gary R. Holtom, and X. Sunney Xie. Three-dimensional vibrational imaging by coherent anti-stokes raman scattering. *Physical Review Letters*, 82(20):4142–4145, May 1999.